Nanoscale thermal transport: size effects and transport regimes

---

A Dissertation
Presented to
the faculty of the School of Engineering and Applied Science
University of Virginia

---

in partial fulfillment
of the requirements for the degree

Doctor of Philosophy

by

Jingjie Zhang

December 2019

APPROVAL SHEET

This Dissertation
is submitted in partial fulfillment of the requirements
for the degree of
Doctor of Philosophy

Author Signature: Jingjie Zhang

This Dissertation has been read and approved by the examining committee:

Advisor: Avik Ghosh

Committee Member: Pamela M. Norris

Committee Member: Patrick E. Hopkins

Committee Member: Keivan Esfarjani

Committee Member: Mona Zebarjadi

Committee Member: ______________________

Accepted for the School of Engineering and Applied Science:

Craig H. Benson, School of Engineering and Applied Science

December 2019

To my family

Abstract

The continuing miniaturization of electronic devices drives the advancement of modern technology. As the device dimension shrinks to the nanoscale, thermal management becomes the bottleneck for further performance improvements of these devices. The performance and the lifetime are reliant on the efficiency of heat dissipation. Poor heat dissipation leads to high operating temperatures, and consequently leads to device performance degradation and device lifetime reduction. To achieve better heat dissipation efficiency in nanoscale devices, a fundamental understanding of thermal transport at the nanoscale is essential. One of the biggest challenges to understanding the phonon transport processes at the nanoscale is the involvement of size effects and transport regimes. In nanostructures or low dimensional solids, the size of a system can be comparable to the phonon characteristic lengths (phonon mean free paths and coherence length), and consequently the thermal conductivity is highly dependent on material sizes and transport regimes.

In this dissertation, I present the study of nanoscale size effects in three different systems with varied levels of complexities. These three projects center around varying the most important material transport properties: number of propagating modes, M, and transmission per mode, T. I first discuss thermal transport from the ballistic to the diffusive regime in an intrinsic two-dimensional material, specifically monolayer transition metal dichalcogenides (TMDs). In this work, number of modes M will not change from the ballistic to the diffusive regime, and the only factor that would vary with the transport regime and the material size is the transmission T. We show that with varying sample sizes, the ordering of thermal conductivity among monolayer transition metal dichalcogenides MX_2 (M: Mo, W; X: S, Se) changes as phonon transport transits from the ballistic to the diffusive regime, driven by the competition between the phonon conduction frequency range and the scattering strength (or reduction of phonon transmission). Then I study size effects of thermal transport across an impedance bridged interface, with both M and T changing from the harmonic to the strongly anharmonic limit. In this project, we introduce a quantity called ”conserving modes” which is the upper-bound of M that conserves momentum and energy in the harmonic limit. It shows that in the harmonic limit, the enhancement of conductance is limited due to fewer available channels, while in the anharmonic limit, the thermal conductance is strongly enhanced due to added inelastic channels. In the last project, I study the size effects demonstrating phonon coherence in superlattices. In these structures, M can be tuned by varying the periodic dimension of superlattices to form new phonon band structures. We propose a method built in Non-Equilibrium Green's Function(NEGF) formalism to illustrate the scattering mechanisms and transport regimes. In addition, we introduce phenomenological models of momentum and phase scattering with the flexibility of adjusting the strength of these scatterings. We find momentum scattering is the only source of thermal resistance while phase scattering only removes wave interference and oscillations in the transmission.

These three projects we show in this dissertation extend our understanding of the size effects in nanoscale thermal transport, and the physics behind these systems can be further applied to other structures as well. The work in this dissertation will benefit the design of better heat dissipation in nanoscale devices.

Acknowledgments

This dissertation would not have been possible without the help and support from many individuals. I would like to express my sincere gratitude to them here.

First, I would like to thank my advisor, Professor Avik Ghosh, who inspired me and guided me in so many ways, and shaped me into a researcher I am today. His profound knowledge inspired me with new ideas and solutions for the difficulties I encountered during my research; his enthusiasm towards work has influenced me to work hard. He has been very supportive and gave me enough freedom to choose the topics that I have interest in, but always lead me to the right direction in those projects. Despite his busy schedule, he shared his time with me and cared about the progress in my research. His invaluable advise beyond the academic life will continue to help me in my future.

I also want to thank my committee members, Prof. Pamela Norris, Prof. Patrick Hopkins, Prof. Keivan Esfarjani, and Prof. Mona Zebarjadi for giving me constructive comments on my research proposal and defense. In addition, my research would not be complete without the collaborations with students from their groups. Their advice through those collaborations guided me during my graduate journey.

I am also grateful to have had the opportunity to work as a co-advised student at the center for Nanophase Materials Sciences (CNMS) of Oak Ridge National Laboratory (ORNL). Funded by the ”GO!” program, I had the chance to work with many brilliant researchers in the lab. I want to thank Prof. Bobby Sumpter, Prof. Kai Xiao, Prof. Xiaoguang Zhang, Liangbo Liang and Xufan Li. With their help and encouragement, the collaborations with

them have been productive and fruitful.

I am lucky to have colleagues who share similar interests in research. I want to thank Ramez Cheaito who inspired me to study size effects in nanoscale thermal transport. I want to thank our ‘thermal group’ members: Carlos Polanco, Rouzbeh Rastgar and Nam Le. Our biweekly meeting continued for five years. We have worked together on many exciting projects on heat transfer. I consider them not only my colleagues, but also dear friends, who share ups and downs in our lives. I want to express my special gratitude to Carlos Polanco who not only helped me tremendously in research through countless discussions and arguments, but also encouraged me to speak my thoughts out loud and express myself. This dissertation is in memory of dear Rouzbeh Rastgar.

I also want to thank my VINO group mates, past and present, for their friendship and companionship. Some of them shared with me different cultures and beliefs; some of them showed me new possibilities in life; some of them helped me with knowledge and wisdom; some of them encouraged me all the way along my PhD journey.

Finally but most importantly, I want to thank my family who are my rock. I am forever indebted to my parents for their endless love and unconditional support. I am very fortunate to have my husband in my life. He gives me hope and strength, and lets me believe that I can achieve those dreams in life. I am also lucky to have had my daughter during this period. She is the biggest source of my happiness and the biggest achievement during my PhD.

Contents

List of Tables

List of Figures

List of Abbreviations

BTE	Boltzmann Transport Equation
MD	Molecular Dynamics
MFP	mean free path
NEGF	Non-Equilibrium Green's Function
SL	Superlattice
TMD	Transition metal dichalcogenide

Chapter 1

Introduction

1.1 Background

Heat transfer plays a significant role in modern science and technology, where the transfer properties are the bottleneck towards many applications [1–3]. In energy conversion applications, low thermal conduction materials and structures are the most desirable to improve the figure of merit in thermoelectric devices [4–7]; In memory applications, materials with high thermal anisotropy are favored in order to introduce a large temperature gradient in heat assisted magnetic recording (HAMR) [8,9]. Most importantly, high thermal conductance and efficient heat dissipation are critical to ensure electronic/optical devices (e.g. high electron mobility transistors, high frequency photodiodes, quantum cascade lasers and microelectronic logic chips) operate at a reliable temperature, and to ensure proper device performance and reliability [10–12].

"The power wall" in microelectronics is a notable example to demonstrate the importance of efficient heat dissipation. As shown by the roadmap of microprocessors in Fig. 1.1, starting in 2002, the single thread clock frequency stopped increasing and maximized at 3 GHz [13,14]. The limiting factor was the high power density and the resulting accumulated temperature during the operation of the processors. The power density P is proportional to the clock frequency f: $P = CV^2 f$ (C: gate or interconnect capacitance); V: voltage bias), and accumulated temperature $\Delta\mathbf{T}$ is proportional to the power density: $\Delta\mathbf{T} = PR$ (R: thermal resistance). As a result, an increasing clock frequency leads to an inevitable increase of temperature in the processor, threatening its performance, reliability and lifetime. For instance, the power density generated in modern day digital circuits on a chip can reach up to 100 W/cm^2, which is 10 times greater than the power density of a hot plate and is around the same magnitude of the power density generated on the outer cladding of a nuclear reactor [14–16]. To achieve a better thermal management in microelectronic devices, a deep but fundamental understanding of nanoscale thermal transport is essential.

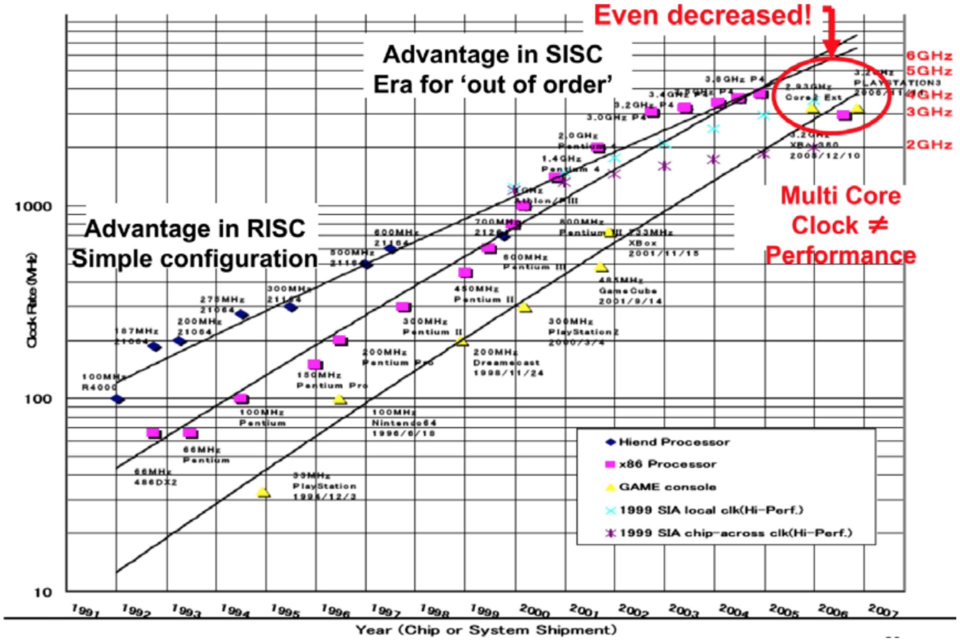

Figure 1.1: Roadmap for clock frequency of microprocessors. [13]

Advances in nanotechnology has enabled the continuous scaling of devices to the nanoscale, following Moore's law [17, 18]. Consequently, thermal transport in current commercial electronic/optical devices is also typically at the nanoscale. For instance, the smallest characteristic dimension of silicon-based commercial CPUs, as of in 2019, is 7 nanometers (AMD Ryzen). Thermal transport in devices/materials at this length scale is substantially different from classical transport processes predicted by Fourier's law, and involves many complexities. One big gap in the complete description of nanoscale thermal transport is the role of *size effects* and *transport regimes*. Take silicon, the foundational material for microelectronics, as an example. The phonon mean free path (MFP) of silicon is of 10^1 – 10^6 nm (Fig. 1.2 (a)), and the phonon wavelength of silicon is $\sim$ 1 nm – 100 nm (Fig. 1.2(b)) [19]. This means that depending on the electronic device dimensions, there is a transition of thermal transport from the ballistic to the diffusive regime, or from the coherent to the incoherent regime.

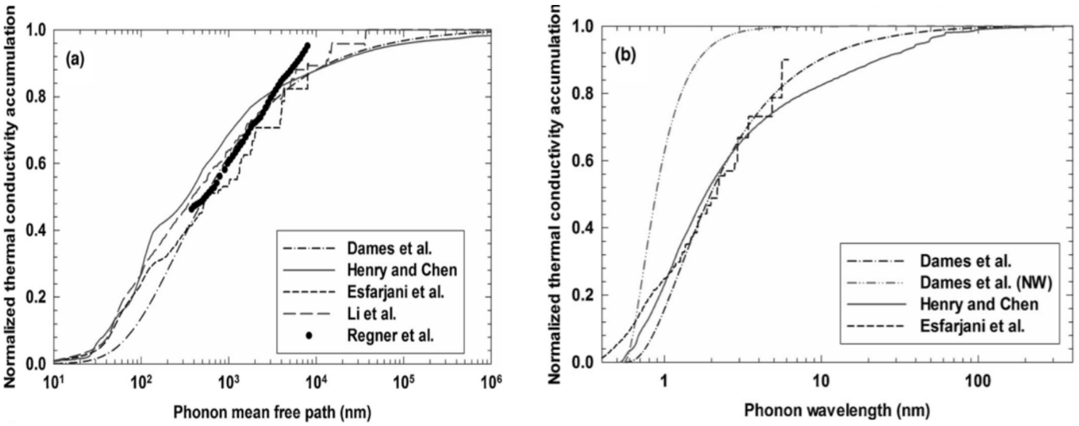

Figure 1.2: (a)The accumulated thermal conductivity of silicon as a function of phonon MFP, demonstrating the silicon phonon MFP is in a range of 10 nm to 10^6 nm; (b)The accumulated thermal conductivity of silicon as a function of phonon wavelength, demonstrating the silicon phonon wavelength is in a range of 1 $\sim$ 100 nm. [19]

Size effect is defined as the phenomenon where the size of a material affects its physical properties. The size effect on thermal conductivity is strongly dependent on the transport regime, and varies from the ballistic to the diffusive regime. For instance, the classical size effect is that the thermal conductivity of a bulk material in the ballistic transport regime increases quasi-linearly with size of the material. This is usually referred to as the *Casimir effect* [20, 21], and can be explained in terms of contributions from phonons with different mean free paths. In semiconductors or insulators, phonons, the quanta of lattice vibrations, are the major heat carriers. The lattice thermal conductivity can be written as $\kappa = \frac{1}{3}\int C_\omega \nu_\omega \Lambda_\omega d\omega$, where C_ω is the volumetric heat capacity, ν_ω is the phonon velocity and Λ_ω is the phonon MFP [20, 21]. When the size of a material shrinks to the scale of the phonon

MFP, phonons scatter at the material boundary before they reach the MFP, leading to a thermal conductivity that depends on the material dimension. On the other hand, if the material dimensions are all larger than the phonon MFP, then phonon transport is in the diffusive regime. Thermal conductivity in this regime recovers Fourier's law and is a constant independent of the material dimension. The transition from the ballistic to the diffusive transport regime is caused by momentum scattering, which is the scattering of the wavevector q of the phonon wavefunction $e^{iqx-i\omega t+\phi}$. This scattering changes the phonon group velocity, reduces transmission, and adds resistance to the transport [22].

Additionally, the size effect of thermal conductivity varies from the coherent to the incoherent regime. In the coherent regime, phonons behave as waves and can interfere with each other and form new band structures. Accordingly, their thermal conductivity can be modified by engineering the phonon band structures [23–26]. This usually happens in periodic systems, such as Superlattice (SL)s or phononic crystals [23–26]. Take the extremely low thermal conductivity of phononic crystals for example. The mid-frequency phonons contribute the most to heat conduction at room temperature because high frequency phonons have high scattering rates and low occupancy while low frequency phonons carry little energy and density of states. The thermal conductivity for phononic crystals can be lowered by creating a large bandgap at thermal frequencies in between, by varying the periodic dimension of the crystal [26]. This idea of engineering phonon band structures to modify the thermal conductivity, however, is not applicable in the incoherent regime when phonons behave as particles. The transition from the coherent to the incoherent regime can be caused by phase scatterings of ϕ for phonon wavefunctions $e^{iqx-i\omega t+\phi}$. This scattering destroys wave interference and eliminates the possibility of forming new phonon band structures by varying the material's periodic dimensions [22].

The study of size effects of thermal transport at the nanoscale faces non-negligible challenges because the results are strongly dependent on the nanostructures under study. In this dissertation, I present the study of three different systems with varied levels of difficulties.

The physics behind these systems can be further applied to other structures as well. Through a study of these three distinct material systems, *my primary goal in this dissertation is to advance the fundamental understanding of nanoscale thermal transport and size effects across different transport regimes.*

1.2 Multiscale thermal transport modeling

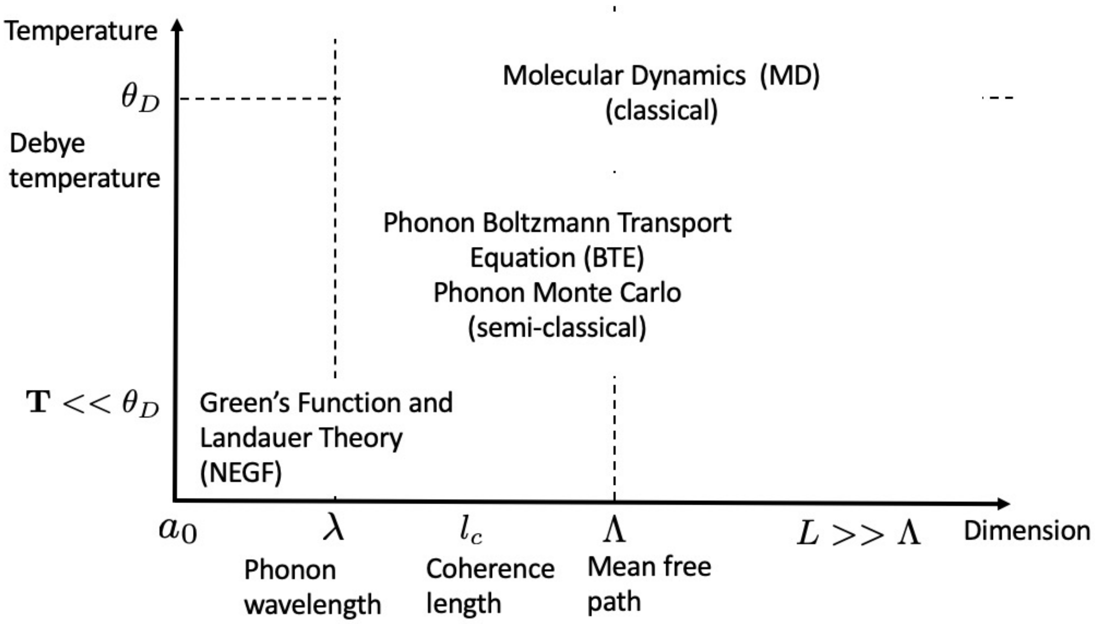

Figure 1.3: Schema for validity of thermal transport modeling methods dependency on material dimension and ambient temperature

The study of size effects and thermal transport regimes at the nanoscale faces considerable challenge due to multiscale modeling. The validity of thermal transport modeling methods and the details to include in a heat conduction model depend on the transport regimes, set by the characteristic length and the ambient temperature [14, 27–29]. The Molecular Dynamics (MD) approach works well for systems over a wide range of dimensions, but it cannot capture quantum effects at low temperatures because it uses the classical limit ensemble (working at $\mathbf{T} > \theta_D$, where θ_D is the Debye temperature). Meanwhile, the Boltzmann Transport Equation (BTE) only applies for systems at or beyond the length scale of phonon MFP ($L \geq \Lambda$)

because it assumes a local equilibrium for the phonon distribution. The Non-Equilibrium Green's Function (NEGF) can describe the phonon quantum distribution as well as phonon interference, but including anharmonicity in NEGF is extremely computationally expensive and limits its application to low temperatures and smaller length scales ($L \leq \Lambda$, $\mathbf{T} \ll \theta_D$). The prevailing modeling methods and their relevant to applicable domains are summarized in Fig. 1.3.

Due to the multiscale nature of my research, most of my work present in the thesis involves utilizing a combination of these methods. NEGF is applied to all the harmonic simulations while either BTE or MD is used to include the anharmonicity. The difference is that BTE is more suitible for systems with periodic boundary conditions along all directions while MD is more suited to thermal transport across interfaces.

1.3 Dissertation organization

In the remainder of the thesis, I will discuss size effects in three different nanostructures in different phonon transport regimes, with different levels of complexities. The differences, and the connections between these projects are best shown by the Landauer equation described below.

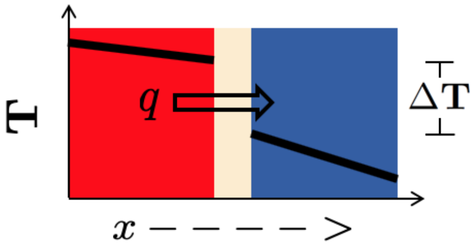

$$\frac{q}{\Delta T} = G = \frac{1}{A}\int_0^{\infty} \frac{d\omega}{2\pi}\hbar\omega\frac{\partial N}{\partial \mathbf{T}}\boxed{MT}$$

Figure 1.4: The Landauer formula for thermal conductance. As shown in the formula, M and T are the critical material properties that determine the thermal conductance.

In the Landauer equation (shown in Fig. 1.4), q is the heat flux, ΔT is the temperature difference, A is the cross-sectional area, $\hbar\omega$ is the phonon energy, N is the Bose-Einsten distribution, M is the number of phonon modes and T is the average transmission per mode. From the Landauer equation, we notice M and T are the most important material properties that affect the conductance or conductivity. The projects in this thesis are centered around varying these two quantities, M and T, in different ways as the transport regime varies.

The first project (chapter 2) involves thermal transport from the ballistic to the diffusive regime in bulk materials – monolayer Transition metal dichalcogenide (TMD)s. In this work, M does not change from the ballistic to the diffusive regime. The only factor that will vary with the transport regime and material size is the transmission T. We then move on to a nanostructure (chapter 3), specifically an impedance bridged interface (for both single layer bridging and multiple layer bridging), where both M and T change from the harmonic to the strong anharmonic limit. In this project, we introduce a quantity called 'conserving modes' which is the upper-bound of M that conserves both momentum and energy in the harmonic limit. In the last project (chapter 4), we study phonon coherence in SLs, where M can be tuned by forming entirely new phonon band structures. Possible future directions for research, and their anticipated challenges are then summarized (chapter 5).

Chapter 2

Bulk transition metal dichalcogenides: ballistic to diffusive

2.1 Introduction

Group-6 transition metal dichalcogenides (TMDs) such as MoS_2 have attracted tremendous attention due to their novel properties and potential applications in electronics [30], optoelectronics [31, 32] and thermoelectrics [33–35]. Unlike graphene, TMDs typically have large electronic bandgaps ($\sim$1.8 eV for MoS_2) which can be tuned with layer thickness and strain [36–38]. Furthermore, a transition from indirect-to-direct bandgap with decreasing layer thickness down to a monolayer suggests further applications in optical devices [31, 32]. Meanwhile, TMDs are predicted to have low thermal conductivities compared to other well explored 2D materials, especially graphene and h-BN, which makes them viable candidates for thermoelectric applications [33–35]. However, the experimentally measured thermal conductivities in TMDs vary widely in literature [39–43]. For instance, the measured thermal conductivity of bulk MoS_2 is $\sim 85 - 110$ W/mK [39], but the reported thermal conductivity for monolayer or few-layer MoS_2 varies from 35 W/mK to 84 W/mK [40–44], since the measured thermal conductivities are sensitive to the sample quality, sample size and measuring methods. The mean free path of some acoustic phonons in MoS_2 can be longer than 10 μm [39, 45]. This implies that as long as the sample sizes are in the nanoscale or even in the microscale, those samples of MoS_2 are in the ballistic to diffusive crossover regime for phonon transport. In gaining a comprehensive understanding of thermal transport in TMDs and to fairly compare it with experiments, calculations of mean free path, isotope effects and sample geometry are highly desirable. Numerous theoretical works have investigated the phonon transport of TMDs using different methods [45–51], but a systematic and in-depth study of the TMD family in both ballistic and diffusive transport regimes with different sample sizes is still lacking. In particular, a full picture of anharmonic scattering rates, mean free paths, and phonon decay channels is needed to reveal the microscopic origin of different thermal conductivities in the TMD family.

In this work, we conduct first-principles simulations on thermal transport in monolayer transition metal dichalcogenides MX_2 (M: Mo, W; X: S, Se) with varying sample sizes. Using Non-Equilibrium Green's Function (NEGF), we compare the number of modes (conducting channels) in these materials, and show that the ballistic thermal conductivity varies inversely with the average atomic mass, which leads to MoS_2 having the largest ballistic thermal conductivity when the sample length is short. Thereafter using iterative Boltzmann Transport Equation (BTE) calculations, we obtain the scattering rates and mean free paths (MFPs), from which we discover a different trend for diffusive thermal conductivity in these materials. In fact, WS_2 has the largest diffusive thermal conductivity, followed by MoS_2, and then WSe_2 and $MoSe_2$. We can rationalize these conflicting trends by bridging transport from the ballistic to diffusive regime using modified Landauer theory and comparing the MFPs. We show that the material with larger thermal conductivity switches between MoS_2 and WS_2 when the sample length is 38.8 nm, and between $MoSe_2$ and WSe_2 when the sample length is 51.5 nm. These results highlight that it is only meaningful to compare thermal conductivities of these materials at comparable sample lengths. Furthermore, significantly higher anharmonic scattering rates are found in $MoSe_2$ compared to the other three materials, because the mid-frequency optical modes in $MoSe_2$ sit just in the middle of the gap between the high-frequency optical modes and acoustic ones, which facilitates the decay process of the high-frequency phonons. Such a high scattering rate in $MoSe_2$ renders its in-plane diffusive thermal conductivity lower than WSe_2. The same flip also occurs between MoS_2 and WS_2 for the same reason in phase space, though the effect is not as severe as in $MoSe_2$.

This work is reproduced with permission from [52] coauthored with Jingjie Zhang, Xufan Li, Kai Xiao, Bobby G. Sumpter, Avik W. Ghosh and Liangbo Liang. Copyright [2019] Institute of Physics Publishing (IOP). Cite This: J. Phys.: Condens. Matter 32, 025306.

2.2 Computational details

We performed first-principles calculations using Quantum Espresso [53]. Norm-Conserving pseudopotentials with Perdew-Zunger exchange-correlation functional within the Local Density Approximation (LDA) were used for all TMDs [54]. We used a $18 \times 18 \times 1$ kpoint mesh and 80 Rydberg cutoff kinetic energy for wavefunctions in the structure relaxation and ground state calculations. A 45 Å vacuum slab was placed between the monolayers. Each structure was fully relaxed to a force threshold of 1.0×10^{-3} eV/Å. The second order force constants were obtained by Density Functional Perturbation Theory (DFPT) calculations with a $16 \times 16 \times 1$ q-mesh on phonon wavevectors [55], and the third order force constants were simulated via a small displacement method by moving the atoms with a 0.04 Å displacement and considering up to 5th neighbor shells (~ 0.6 nm). In the phonon scattering rates and thermal conductivity calculations, a $100 \times 100 \times 1$ q-mesh sampling is used. This Brillouin zone grids, displacement setup and the number of neighbors were carefully chosen to converge the thermal conductivity in less than 10% variance intervals. Note that the LO-TO splitting in monolayer MX_2 is very small, and thus this effect is negligible and was not included in our calculations [47, 50].

We used the Landauer equation, modified for scattering to account for the thermal conductivity variation from ballistic to diffusive regimes [56, 57]:

$$\kappa = \frac{1}{2\pi A}\int_{0}^{\infty} \hbar\omega M(\omega)\frac{\lambda(\omega)L}{\lambda(\omega)+L}\frac{\partial N}{\partial \mathbf{T}}d\omega, \tag{2.1}$$

where $M(\omega)$ is the number of transport channels (or 'number of phonon propagating modes') per unit cross-sectional area in TMDs, $\bar{T}$ is the average transmission per mode (in this study, $\bar{T}$ is unity due to the homogeneous nature of the materials) [58, 59], $\lambda(\omega)$ is the frequency dependent MFP, L is the sample length, N is the Bose-Einstein occupancy, $\mathbf{T}$ is ambient temperature and A is the cross-sectional area perpendicular to the transport direction. When $L \gg \lambda(\omega)$, the Landauer equation recovers the diffusive limit conductivity predicted by the Boltzmann transport equation which follows Fourier's law.

$M(\omega)$ was computed using NEGF as $M(\omega)\bar{T} = \text{Trace}\{\Gamma_l G \Gamma_r G^\dagger\}$, where $\Gamma_{l,r}$ is the broadening matrix of the left or right contact, G is the retarded Green's function [56, 60, 61]. Since $\bar{T}$ is unity when we calculated $M\bar{T}$ for bulk homogeneous materials, we can obtain $M(\omega)$ directly from NEGF. The self-energy matrices responsible for heat injection and broadening were calculated using recursion, assuming that the contacts were material extensions of the channel. $M(\omega)$ was first calculated for every transverse momentum, and then the momenta were summed over to get a frequency-dependent mode and ballistic thermal conductance.

MFPs were obtained by solving Boltzmann transport equations(BTE) including three phonon scattering and isotopic scattering mechanisms by ShengBTE [62]. In this step, only resistive Umklapp scattering is included in the phonon-phonon scattering process by achieving a convergence in the thermal conductivity when solving BTE iteratively. The isotopic scattering was taken into account by the Tamura formula with naturally distributed isotopes. The frequency dependent MFPs were achieved by averaging over momentum: $\lambda(\omega) = 2\langle v_x^2\tau\rangle/\langle|v_x|\rangle$ in which $\langle v_x^2\tau\rangle$ means $\frac{\sum_{q,s}\delta(\omega-\omega_{q,s}){v_x}^2\tau_{q,s}}{\sum_{q,s}\delta(\omega-\omega_{q,s})}$ and $\langle|v_x|\rangle$ means $\frac{\sum_{q,s}\delta(\omega-\omega_{q,s})|v_x|}{\sum_{q,s}\delta(\omega-\omega_{q,s})}$, where v_x is the velocity in the transport direction, q is the phonon wavevector, s is the polarization, $\tau_{q,s}$ is the phonon relaxation time of mode labeled by q, s, $\delta(\omega - \omega_{q,s})$ is the delta function in frequency, and $D(\omega) = \sum_{q,s} \delta(\omega - \omega_{q,s})$ is the phonon density of states. [57]

2.2.1 Simulation details of scattering rates and number of scattering processes

The scattering rates were obtained by considering three–phonon scattering and isotope scattering following Mattiessen's rule [63]:

$$\frac{1}{\tau_j} = \frac{1}{N}(\sum_{j'j''}^{+} \Gamma^{+}_{jj'j''} + \sum_{j'j''}^{-} \frac{1}{2}\Gamma^{-}_{jj'j''} + \sum_{j'} \Gamma_{jj'}), \tag{2.2}$$

where τ_j is the phonon relaxation time for phonon mode j, N is the number of q points sampling the Brillouin zone (BZ) (in our calculations $N = 100 \times 100 \times 1 = 10^4$). $\Gamma^{+}_{jj'j''}$ and $\Gamma^{-}_{jj'j''}$ are the three–phonon scattering rates for the absorption process and decay process respectively, while $\Gamma_{jj'}$ is the isotope scattering rate. If the normal process for three–phonon scattering is treated as resistive one (in other words, if the system is under the relaxation time approximation (RTA)), the scattering rates for the three-phonon scattering can be written in the form of Fermi's Golden Rule: [62, 64]

$$\Gamma^{+}_{jj'j''} = \frac{\hbar\pi}{4}\frac{N_0^{'} - N_0^{''}}{\omega_j\omega_{j'}\omega_{j''}}|V^{+}_{jj'j''}|^2\delta(\omega_j + \omega_{j'} - \omega_{j''}) \tag{2.3}$$

$$\Gamma^{-}_{jj'j''} = \frac{\hbar\pi}{4}\frac{N_0^{'} + N_0^{''} + 1}{\omega_j\omega_{j'}\omega_{j''}}|V^{-}_{jj'j''}|^2\delta(\omega_j - \omega_{j'} - \omega_{j''}) \tag{2.4}$$

where $V^{\pm}_{jj'j''}$ are the scattering matrix elements, N_0' is Bose-Einstein distribution for the phonon mode j' with frequency $\omega_{j'}$ (0 denotes zeroth order).

To selectively include Umklapp scattering, the scattering rates are calculated by solving the Boltzmann transport equation iteratively, and by achieving a convergence in the thermal conductivity: [62, 64–66]

$$\kappa^{\alpha\beta} = \frac{1}{k_B \mathbf{T}\Omega\mathbf{N}} \sum_j N_0(N_0+1)(\hbar\omega)^2 v_j^\alpha F_j^\beta \tag{2.5}$$

where Ω is the volume of the simulation unit cell, $\mathbf{N}$ is the total number of modes, α, β are the labels for the displacement degree of freedom, and F_j is defined in terms of the first order expansion of the non-equilibrium phonon distribution $N(\omega_j)$:

$$N(\omega_j) \approx N_0(\omega_j) - F_j \cdot \bigtriangledown \mathbf{T} \frac{dN_0}{d\mathbf{T}}, \tag{2.6}$$

where $N_0(\omega_j)$ is the Bose-Einstein distribution, and F_j can be written as:

$$F_j = \tau_j^0 (v_j + \Delta_j), \tag{2.7}$$

where τ_j^0 is the relaxation time of mode j following the RTA. Δ_j, having dimension of velocity, controls the deviation of the system from the RTA prediction. Δ_j is also the critical parameter confirming that the system only includes Umklapp scattering processes. All our simulations are performed using the iterative BTE package ShengBTE. [62]

In Fig. 2.6, the number of scattering processes (the number of branch/polarization dependent scattering processes) are counted by considering all three–phonon pairs that satisfy both momentum and energy conservation. In this step we did not exclude normal processes due to the complexity of tracking the polarization of phonon modes in the self-consistent calculations.

Separating the scattering processes into frequency regimes (high frequency optical modes (HFOM), middle frequency optical modes (MFOM) and acoustic modes (AM)) (illustrated in Fig. 2.5) is equivalent to classifying phonon modes by polarization. Much like acoustic modes that can be classified as out-of-plane zone boundary acoustic (ZA), in-plance transverse acoustic (TA), in-plance longitudinal acoustic (LA) modes, in our study, we separated the polarizations into three categories: AM (including ZA, LA, TA), MFOM and HFOM. Taking Fermi's Golden Rule for the decay process in Eq. 2.4 for example, a phonon mode j can be written as label pairs (q, s), where q is the phonon wavevector, and s is the polarization. In each decay process, for instance HFOM to AM+MFOM, three phonons should satisfy the conservation rules in such a way that: the energy conservation $\omega_{q,HFOM} = \omega_{q',AM} + \omega_{q'',MFOM}$ and the momentum conservation $q = q' + q'' + Q$ (Q is the reciprocal space lattice vector). Based on the q-mesh sampling we have $(100 \times 100 \times 1)$, we look through 9×10^4 phonon modes for the three–phonon pairs satisfying the conservation rules.

2.3 The order of thermal conductivity from ballistic to diffusive regime

The number of modes $M(\omega)$ of MX_2 in Fig. 2.1 does not show a significant difference in magnitude, especially for the acoustic phonon modes (MoS_2: $0 < \omega < 44.5$ Trad/s; WS_2: $0 < \omega < 35.2$ Trad/s; $MoSe_2$: $0 < \omega < 30.2$ Trad/s; WSe_2: $0 < \omega < 26.5$ Trad/s), which are the major conductivity contributors at room temperature. However, there are large differences in the frequency ranges of the highest frequency optical modes. MoS_2 has the largest phonon frequency range ($\omega < 87.4$ Trad/s), followed by WS_2 ($\omega < 81.7$ Trad/s), $MoSe_2$ ($\omega < 65.9$ Trad/s) and then WSe_2 ($\omega < 57.7$ Trad/s), which is inversely proportional to the order of the average masses in these four TMDs. The number of modes indicates the number of available transport channels, so the summation of $M(\omega)$ over a thermal window set by $\hbar\omega\frac{\partial N}{\partial \mathbf{T}}$ (in the classic limit, this quantity approaches the Boltzmann constant k_B, indicating all modes available for transport) would give us the ballistic conductance G_{int}:

$$G_{int} = \frac{1}{2\pi A}\int_0^{\omega_{max}} \hbar\omega\frac{\partial N}{\partial \mathbf{T}} M(\omega)d\omega \xrightarrow[\text{classical limit}]{k_B\mathbf{T}\gg\hbar\omega_{max}} \frac{k_B}{2\pi A}\int_0^{\omega_{max}} M(\omega)d\omega. \tag{2.8}$$

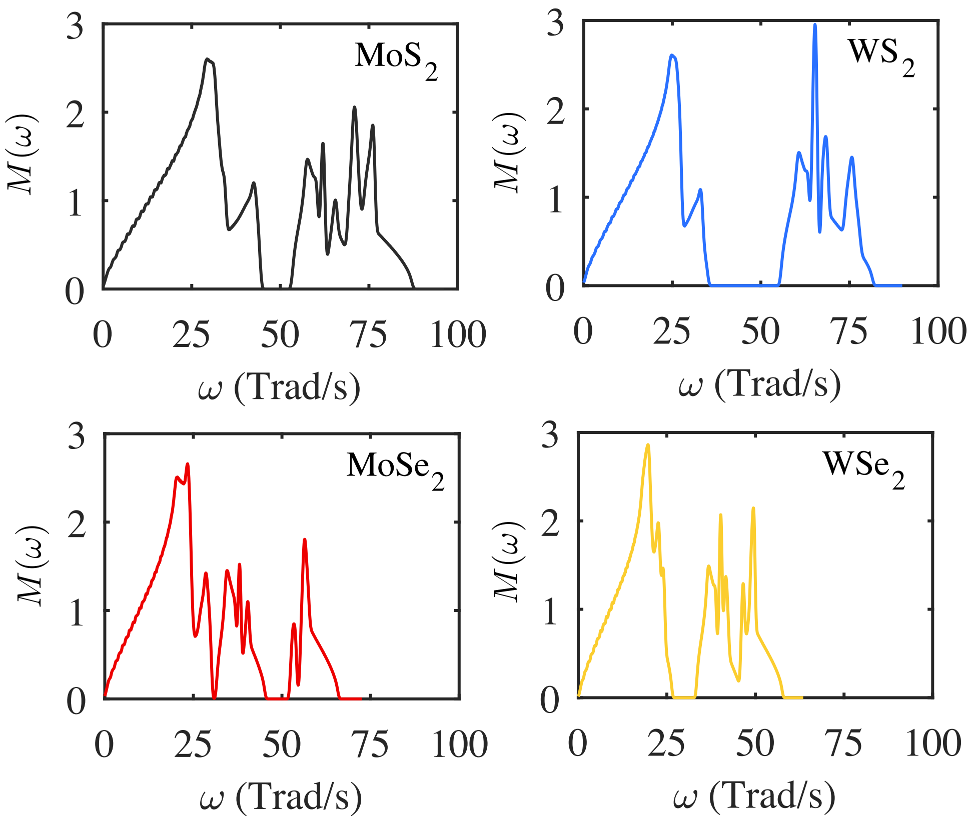

Figure 2.1: Number of phonon propagating modes $M(\omega)$ of MX_2. Number of modes (or channels) are similar in magnitude among these four materials, suggesting that the ordering of ballistic thermal conductance will follow the ordering of the frequency bandwidth.

This indicates that MoS_2 should have the largest *ballistic* thermal conductivity among the four MX_2 species studied here. This is indeed the case, as shown in Fig. 2.2(a), where we plot the ballistic thermal conductivities for samples with a length of 1 μm. Simply speaking, since a lighter mass suggests a higher phonon cut off frequency, the ballistic thermal conductivity is roughly inversely proportional to the average atomic mass.

The thermal conductivities of MX_2 including anharmonic and isotopic scatterings, at different temperatures with sample length fixed at 1 μm, are shown in Fig. 2.2(b). Contrary to the ballistic conductivity trends in Fig. 2.2(a), WS_2 has a much larger conductivity than the others, while $MoSe_2$ shows a smaller κ than WSe_2. Specifically, for the sample length 1 μm at room temperature, $MoSe_2$ has the smallest thermal conductivity (49.9 W m^{-1}K^{-1}), followed by WSe_2 (54.2 Wm^{-1}K^{-1}), MoS_2 (92.9 W m^{-1}K^{-1}), and WS_2 (154.5 W m^{-1}K^{-1}).

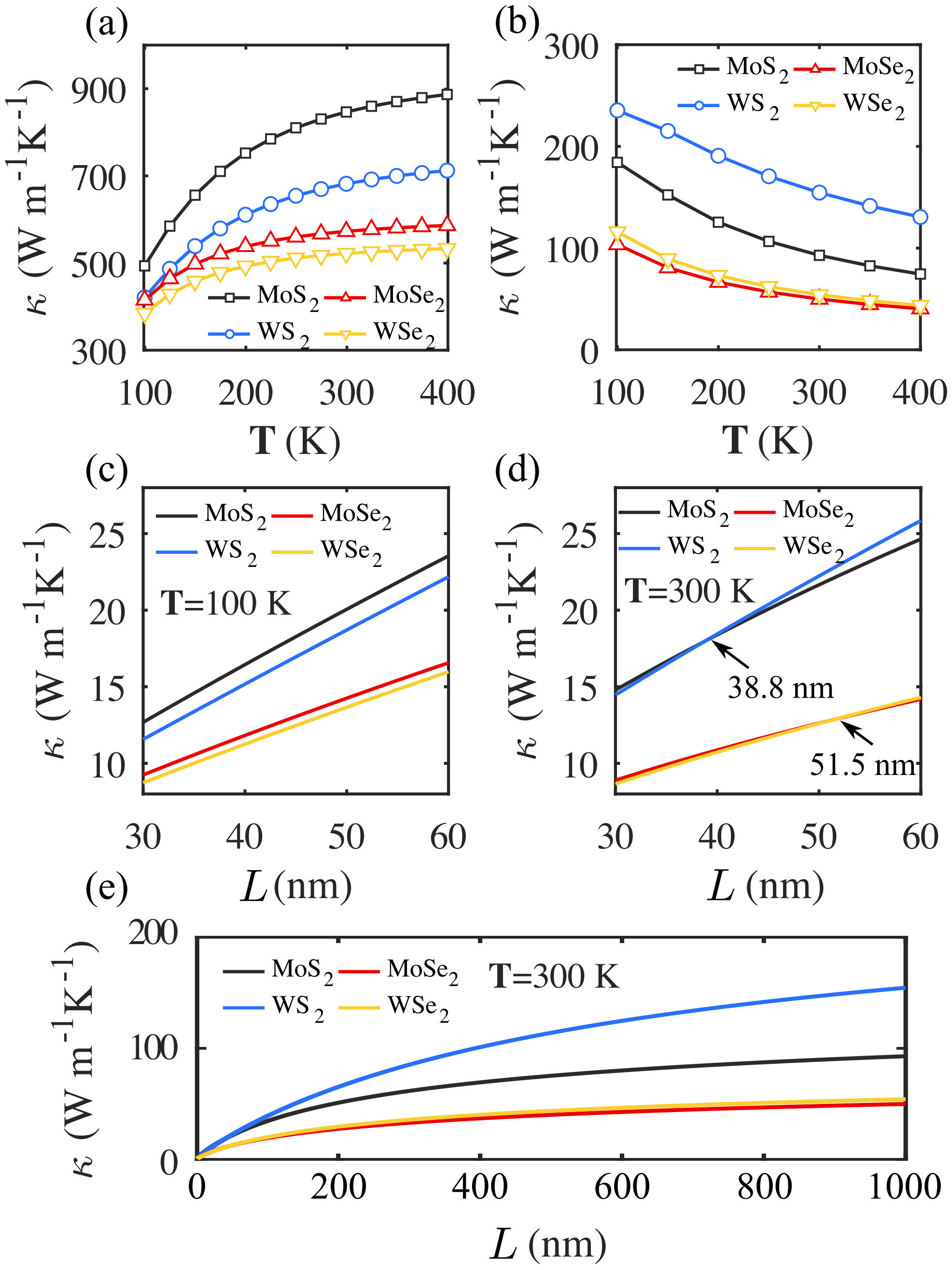

Figure 2.2: (a) Thermal conductivity κ of MX_2 considering only the ballistic contribution with sample length 1 μm. (b) κ of MX_2 including anharmonic and isotopic scatterings with sample length 1 μm. κ of MX_2 at (c) 100 K and (d) room temperature (300 K) with sample length varied from 30 nm to 60 nm. (e) κ of MX_2 at room temperature with the sample size varied from 0 nm to 1000 nm.

The calculated conductivities are in agreement with prior experimental [40,43] and theoretical works [45,46,48,51]. We can thereby conclude that WS_2 has a longer MFP than MoS_2, and

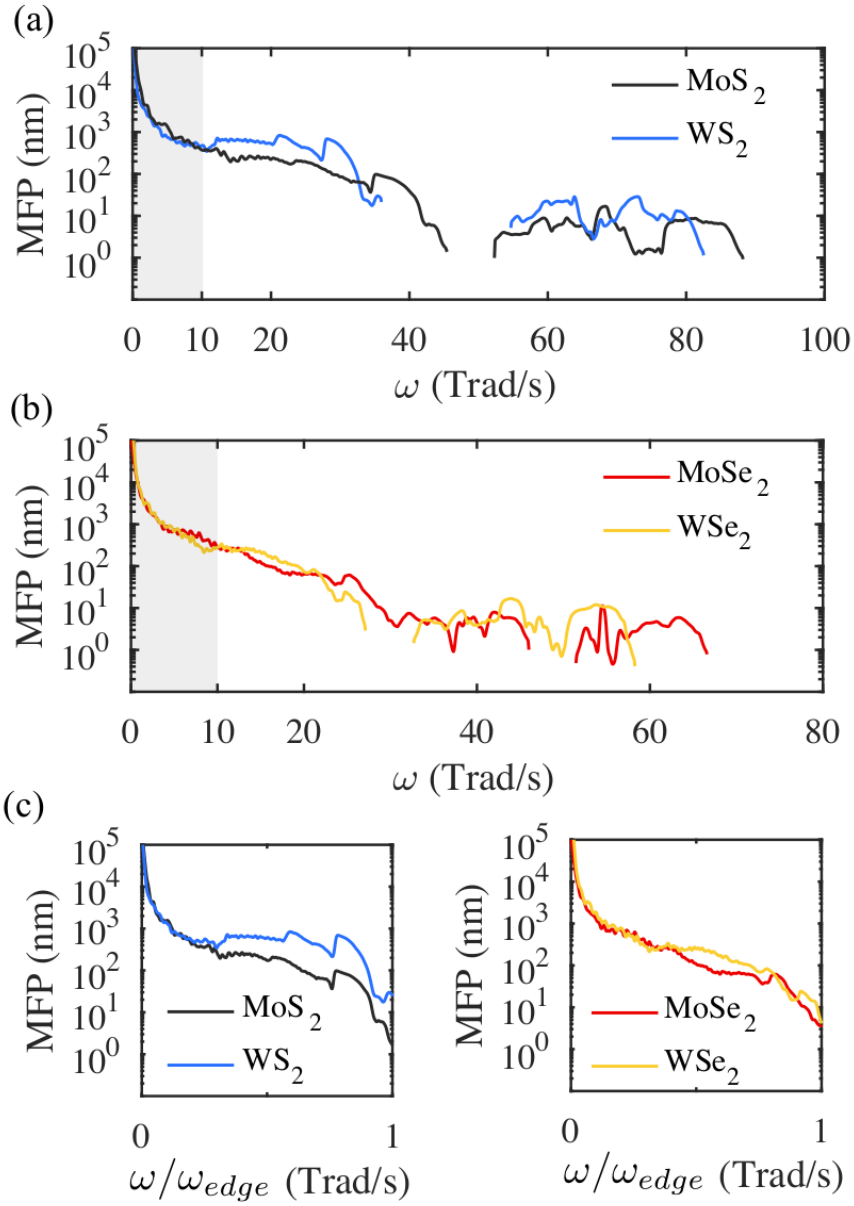

Figure 2.3: The comparison of mean free paths (MFPs) at room temperature between (a) MoS_2 and WS_2; (b) $MoSe_2$ and WSe_2. (c) The MFPs of acoustic phonons with the spectra scaled by the acoustic band edges ($\omega/\omega_{\mathrm{edge}}$).

WSe_2 has a longer MFP than $MoSe_2$. This conclusion is readily validated by comparing the MFPs (Fig. 2.3) directly from the calculated scattering rates.

Fig. 2.3 confirms that the overall MFP of WS_2 is longer than MoS_2, while that of WSe_2 is longer than $MoSe_2$, especially for modes near the acoustic band edge as shown in Fig. 2.3(c) (45.3 Trad/s for MoS_2, 35.9 Trad/s for WS_2, 30.9 Trad/s for $MoSe_2$, and 27.0 Trad/s for

WSe_2). These acoustic phonons are the major contributors to the thermal conductivity at room temperatures; as a result, the MFPs of these phonons determine the order of the thermal conductivity at room temperature. Meanwhile, we see that in a 1 μm long sample, almost all phonons with frequencies higher than 10 Trad/s transport diffusively since their MFPs $<$ 1000 nm. However, those phonons with frequencies lower than 10 Trad/s would transport ballistically up to a length of 100 μm. This is further confirmed by Fig. 2.2(e), where the thermal conductivities are not saturated for a 1000 nm sample size, indicating that a portion of the phonons still transport ballistically.

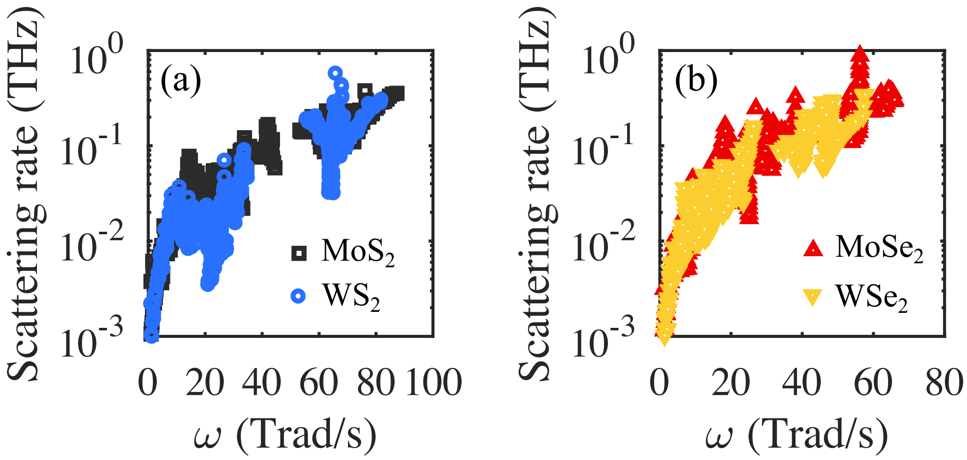

Figure 2.4: Anharmonic scattering rates of (a) MoS_2 and WS_2; (b) $MoSe_2$ and WSe_2.

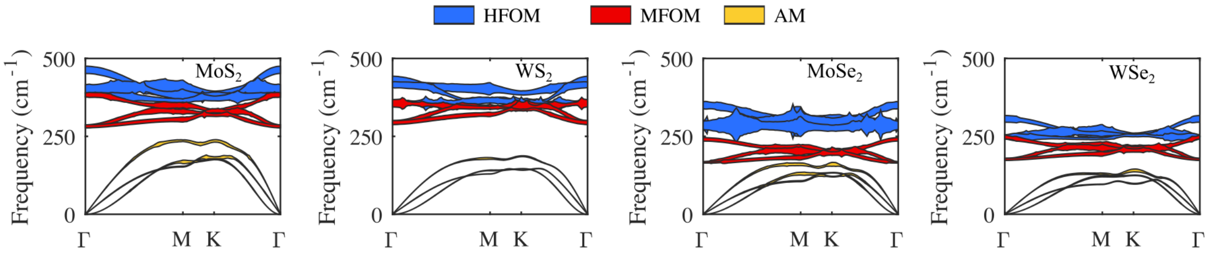

Figure 2.5: Phonon dispersions of MoS_2, WS_2, $MoSe_2$ and WSe_2. Each phonon branch is shadowed with anharmonic phonon Full Width at Half Maximum (FWHM) at 300 K, expressed in cm^{-1} and amplified by a factor of 30. The phonon branches are categorized into acoustic modes (AM, highlighted in yellow), mid-frequency optical modes (MFOM, highlighted in red) and high-frequency optical modes (HFOM, highlighted in blue). The small bandgap of $MoSe_2$ along with the coupling of AM and HFOM through MFOM creates large scattering.

Fig. 2.2(c) and Fig. 2.2(d) show κ within a smaller sample size range at 100 K and 300 K, respectively. With an increasing temperature, the order of the thermal conductivity reverses between MoS_2 and WS_2, and between $MoSe_2$ and WSe_2. For example, at 100 K, when the anharmonic scattering is relatively weak, the order of κ follows the one with only ballistic contributions (Fig. 2.2(a)); however, at 300 K, when the anharmonicity becomes stronger, the order of κ reverses. This inverted ordering occurs for MoS_2 and WS_2 when the sample length is 38.8 nm, and at 51.5 nm for $MoSe_2$ and WSe_2.

The inverted order of thermal conductivity in MX_2 can be explained by a comparison of the scattering rates (Fig. 2.4). The scattering rate of WS_2 is lower than that of MoS_2 for acoustic phonons (Fig. 2.4(a)), which yields a longer MFP of WS_2 near the acoustic phonon band edge (Fig. 2.3(c)). This difference in scattering rate can be attributed primarily to the difference in the phonon bandgap. The bandgap limits the range of three phonon scattering processes subject to energy conservation. WS_2 has a larger phonon bandgap than MoS_2, which explains why anharmonic scattering is less profuse in WS_2 than in MoS_2. The differences in phonon bandgaps among these MX_2 materials also manifest in the $M(\omega)$ illustrated in Fig. 2.1. The bandgaps in $M(\omega)$ are 6.8 Trad/s, 18.5 Trad/s, 5.4 Trad/s and 5.4 Trad/s for MoS_2, WS_2, $MoSe_2$ and WSe_2, respectively. WS_2 exhibits the largest phonon bandgap, while $MoSe_2$ and WSe_2 have the smallest bandgaps, as shown in Fig. 2.1 and Fig. 2.5. **Notably, the bandgap of $MoSe_2$ does not lie between acoustic and optical phonon branches like the other three materials (between yellow and red bands in Fig. 2.5), but lies instead between mid-frequency optical modes and high-frequency optical modes (between red and blue bands in Fig. 2.5).** This unique phonon dispersion with the smallest phonon bandgap is mainly responsible for the overall higher scattering rate of $MoSe_2$ over all three of its relatives (Fig. 2.4), especially for optical phonons.

In general, the phonon branches in MX_2 are distributed into three frequency regions, which can be categorized into AM, MFOM and HFOM, as illustrated in Fig. 2.5 with the AM modes shad in yellow, MFOM modes shad in red, and HFOM modes shad in blue. For

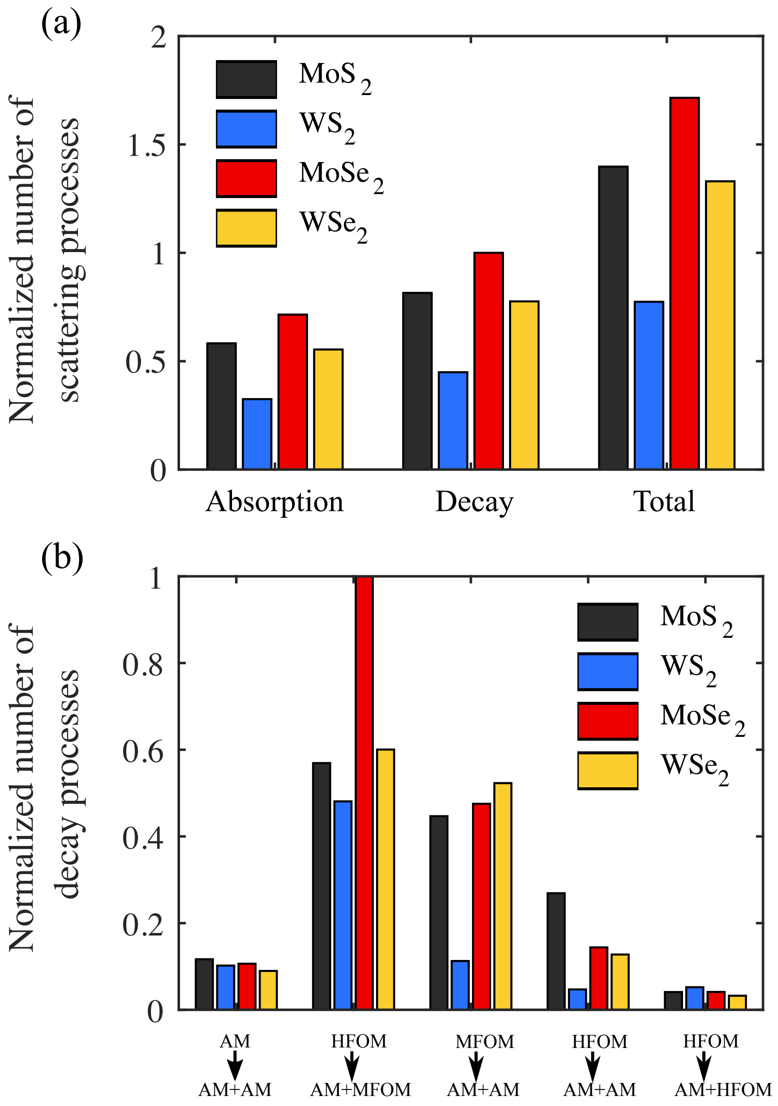

Figure 2.6: (a) The normalized number of scattering processes. (b) The normalized number of branch dependent decay processes in MX_2.

$MoSe_2$, the three mid-frequency branches arise from vibrations of the Se atoms. Distinct from the other three materials, these mid-frequency branches span almost the entire bandgap between the acoustic and high-frequency optical branches, while in the other three materials, they are separated from the acoustic branches and tangled together with the high-frequency optical branches. Besides the differences in bond strengths, this can be largely attributed to the differences in atom masses among the four materials [46]. Taking $MoSe_2$ and WSe_2 for example, the mid-frequency optical modes are located roughly around the same frequency range (Fig. 2.5), since they are associated with the vibration of the Se atoms. However, for the high-frequency optical modes that are typically related to both the metal and Se atoms, their frequencies are notably lower for WSe_2 compared to $MoSe_2$ and thus they are closer to the mid-frequency optical modes in the case of WSe_2, since the W atom (mass 183.84) is much heavier than the Mo atom (mass 95.95). Similarly, the heavier W atoms in WSe_2 lower the acoustic modes, rendering them further away from the mid-frequency optical modes (Fig. 2.5). In short, the mass difference between W and Mo atoms is a primary reason why the MFOM are not located in the middle of the HFOM and AM for WSe_2. Due to the different relative locations of the mid-frequency branches, the Full Widths at Half Maximum (FWHM) of optical phonons in $MoSe_2$ are visibly higher than those of the other three materials, consistent with Fig. 2.4 where the overall scattering rate of $MoSe_2$ is also higher. FWHM linewidth is a scattering strength that can be measured from Raman or infrared experiments, and equals the inverse phonon lifetimes, indicating the scattering rates for each phonon mode. As shown in Fig. 2.5, each phonon branch is shad with its FWHM at 300K, amplified by a factor of 30.

To further understand the influence of the unique dispersion of $MoSe_2$ and its high scattering rate, Fig. 2.6(a) shows the number of available scattering processes in MX_2 normalized by the number of available decay scattering in $MoSe_2$. This quantity is obtained by considering the number of three phonon modes that satisfy both momentum and energy conservation, determined by the phonon dispersion alone. We notice that the number of available scattering processes is largest in $MoSe_2$, and then MoS_2, WSe_2 and WS_2. In Fig. 2.6(b), we show the number of branch dependent decay processes in these four TMDs. All the available scattering processes are normalized by the number of high frequency modes decaying to acoustic and middle frequency optical phonons (HFOM to AM+MFOM) in $MoSe_2$.

The decay process involves five different types of scatterings: an acoustic phonon decays to 2 acoustic phonons (AM to AM+AM), a high-frequency optical phonon decays to 2 acoustic phonons (HFOM to AM+AM), a high-frequency optical phonon decays to a high-frequency optical phonon and an acoustic phonon (HFOM to HFOM+AM), a mid-frequency optical phonon decays to 2 acoustic phonons (MFOM to AM+AM), and finally HFOM to AM+MFOM. We notice that in the first four types of processes, the number of available scattering channels is quite similar between $MoSe_2$ and WSe_2, due to their similar phonon bandgaps. However, what is interesting is that the process of HFOM to AM+MFOM is much more significant in $MoSe_2$, which is a whopping 170% of the largest of the remaining three materials, as shown in Fig. 2.6(b). This means that in $MoSe_2$ the decay process of high-frequency modes into acoustic phonons is increased significantly due to coupling by the mid-frequency modes. We note once again that only for $MoSe_2$, the position of mid-frequency modes is around the middle of the gap between HFOM and AM (Fig. 2.5). It is expected that this special position of MFOM in $MoSe_2$ facilitates the decay process of HFOM to AM, subject to overall energy conservation. Note that in the calculations of phonon scattering, we considered phonons in the whole Brillouin zone, instead of only the modes illustrated by band dispersions in Fig. 2.5. With $100 \times 100 \times 1$ q-mesh sampling, we counted the three-phonon pairs among 9×10^4 phonon modes that satisfy the conservation rules of both momentum and energy.

2.4 Isotope engineering of thermal conduction in MoS_2 monolayers

In the above section, we discussed how the ordering of the thermal conductivity of monolayer TMDs varies from the ballistic to diffusive regime, and how we can tune the thermal conductivity by varying the atomic composites. However, the thermal conductivity and the mean free paths of TMDs are not only dependent on temperature, but also sensitively on defects and isotopes [67, 68]. In the following section, we will discuss the effect of isotopes and defects on the thermal conduction in TMDs, and show how conductivity can be greatly enhanced due to isotope enrichment, both experimentally and theoretically.

The following content is reprinted in part with permission from ACS Nano 2019, 13, 2, 2481-2489 [44] coauthored with Xufan Li, Alexander A. Puretzky, Anthony Yoshimura, Xiahan Sang, Qiannan Cui, Yuanyuan Li, Liangbo Liang, Avik W. Ghosh, Hui Zhao, Raymond R. Unocic, Vincent Meunier, Christopher M. Rouleau, Bobby G. Sumpter, David B. Geohegan and Kai Xiao. Copyright [2019] American Chemical Society.

2.4.1 Raman thermal conductivity measurement

The laser power-dependent and temperature-dependent Raman spectra of the suspended and Si_3N_4-supported MoS_2 monolayers were measured in a home-built micro-photoluminescence (PL)/Raman setup with similar configuration as for a PL measurement, except for an 1800 groves/mm grating. The power-dependent spectra were acquired at room temperature with the laser power ranging from ~15 to 150 μW, while the temperature-dependency were measured within the temperature range of 290-470 K. The sample preparation and Raman measurement were performed by Xufan Li from CNMS at ORNL.

Our calculation of κ_{sus} follows closely the established method described in ref. [69]. This method is based on solving the heat diffusion equation in cylindrical coordinates:

$$\begin{aligned}\frac{1}{r}\frac{d}{dr}(r\frac{d\mathbf{T}}{dr}) + \frac{q'''}{\kappa_{sus}} = 0, (r \leq \mathbf{R})\\ \frac{1}{r}\frac{d}{dr}(r\frac{d\mathbf{T}}{dr}) - \frac{g}{\kappa_{sup}t}(\mathbf{T}-\mathbf{T}_a) + \frac{q'''}{\kappa_{sup}} = 0, (r \geq \mathbf{R})\end{aligned}$$

in which κ_{sup} is the Bassel thermal conductivity in the supported MoS_2, g is the interfacial thermal conductance between the MoS2 monolayer and Si_3N_4 substrate, $\mathbf{T}_a$ is the environment temperature, t is the thickness of monolayer MoS_2 (0.65 nm), R is the hole radius of the suspended region (1 μm), q''' is the volumetric optical heating, expressed as:

$$q''' = \frac{I\alpha}{t} exp(-r^2/r_0^2) \tag{2.9}$$

where α is the absorbance of the monolayer MoS_2 (9% based on ref. [47] since we share the same Si_3N_4 substrate), r_0 is the radius of the laser beam spot size (0.2 μm) and $I = P/(\pi r_0^2)$ is the peak laser power per unit area at the center of the beam. The relation between g and κ_{sup} was obtained using the converged solution for equation 8 in ref. [70].

2.4.2 Mean free path and scattering rates calculations

To consider the influence of isotope scattering and defect scattering on the thermal conductivity of MoS_2, we use the same methods and steps described in the previous section, and we briefly repeat here. We obtained λ by calculating the phonon lifetime, the inverse of the scattering rates and phonon velocities. The phonon lifetime includes phonon-phonon scattering and isotope scattering, and is obtained using Matthiessen's rule by summing over the scattering rates: $\frac{1}{\tau} = \frac{1}{\tau_{ph-ph}} + \frac{1}{\tau_{iso}}$. The scattering rates are simulated by solving BTE interactively using ShengBTE [62], with the 2^{nd} order and the 3^{rd} order force constants. Three-phonon processes are considered to obtain the phonon-phonon scattering rate $\frac{1}{\tau_{ph-ph}}$, and the isotope scattering rate $\frac{1}{\tau_{iso}}$ is included by the Tamura formula (ref. [71]). Once the scattering rates were obtained, the length dependent thermal conductivity (Figure 2.10) is calculated by the Landauer equation [56].

Vacancy scattering calculations

We tested the influence of Sulfur vacancies on the thermal conductivity of MoS_2. This influence is taken into account by adding two additional scattering rates to the Matthiessen's summation: the scattering rate of missing mass of the S vacancy ($\frac{1}{\tau_v}$) and the scattering rate due to change in interatomic force constants between the missing S atom and its under-coordinate Mo neighbors ($\frac{1}{\tau_A}$). These two kinds of scattering rates are calculated by following the Klemens's formula: [72, 73]

$$\frac{1}{\tau_v} = x_v(\frac{\Delta\mathbf{M}}{\mathbf{M}})^2\frac{\pi}{2}\frac{\omega^2 D(\omega)}{\mathbf{G}}$$
$$\frac{1}{\tau_A} = x_A(\frac{\Delta\mathbf{K}}{\mathbf{K}})^2 4\pi\frac{\omega^2 D(\omega)}{\mathbf{G}}$$

where $\mathbf{G}$ is the number of atoms in the unit cell, $D(\omega)$ is the phonon density of states, x_v is the mole fraction of the S vacancies and $x_A = zx_v$ is the mole fraction of the under-coordinate Mo atoms (the coordinate number z is 3 for MoS_2). The perturbation of mass due to S vacancy is $\frac{\Delta\mathbf{M}}{\mathbf{M}} = -\frac{\mathbf{M}_S}{\bar{\mathbf{M}}} - 2$, where $\mathbf{M}_S$ is the mass of the missing S atom and $\bar{\mathbf{M}}$ is the average atomic mass in the MoS_2 unit cell; The force constant change due to S vacancy, $\frac{\Delta\mathbf{K}}{\mathbf{K}}$, is included by considering the local potential change for the under-coordinate atoms and the change in the bond-contraction coefficient $\frac{\Delta\mathbf{K}}{\mathbf{K}} = (\frac{C_z-1}{C_z})^{-(m+2)} = \{\frac{1+exp[(12-z)/(8z)]}{1+exp[(13-z)/(8z-8)]}\}^{-(m+2)}$, where C_z is the bond-contraction coefficient and m is the a parameter to indicate the bonding nature of a specific material. [73–75]

2.4.3 Experimental and theoretical results

It was observed that within the environmental temperature range ($\sim 290 - 470$ K) and the laser power range ($\sim 15 - 150\mu$W), the Raman modes of all the MoS_2 monolayers shift linearly towards lower frequencies in response to either increasing laser power (Figure 2.7(a) and (b)) or increasing the environment temperature (Figure 2.7(c) and (d)), which both result in heating the monolayers. The nonlinearity of the Raman mode shift is not considered here since that only matters at higher temperatures [41,76] or larger laser powers (> 0.25mW). [40] The slope of the linear curves in Figure 2.7(a) (d) are the temperature-coefficient (χ_T) and the power-coefficient (χ_P) of the A_{1g} mode for suspended Mo_2 monolayers (the values are shown in Table 1).

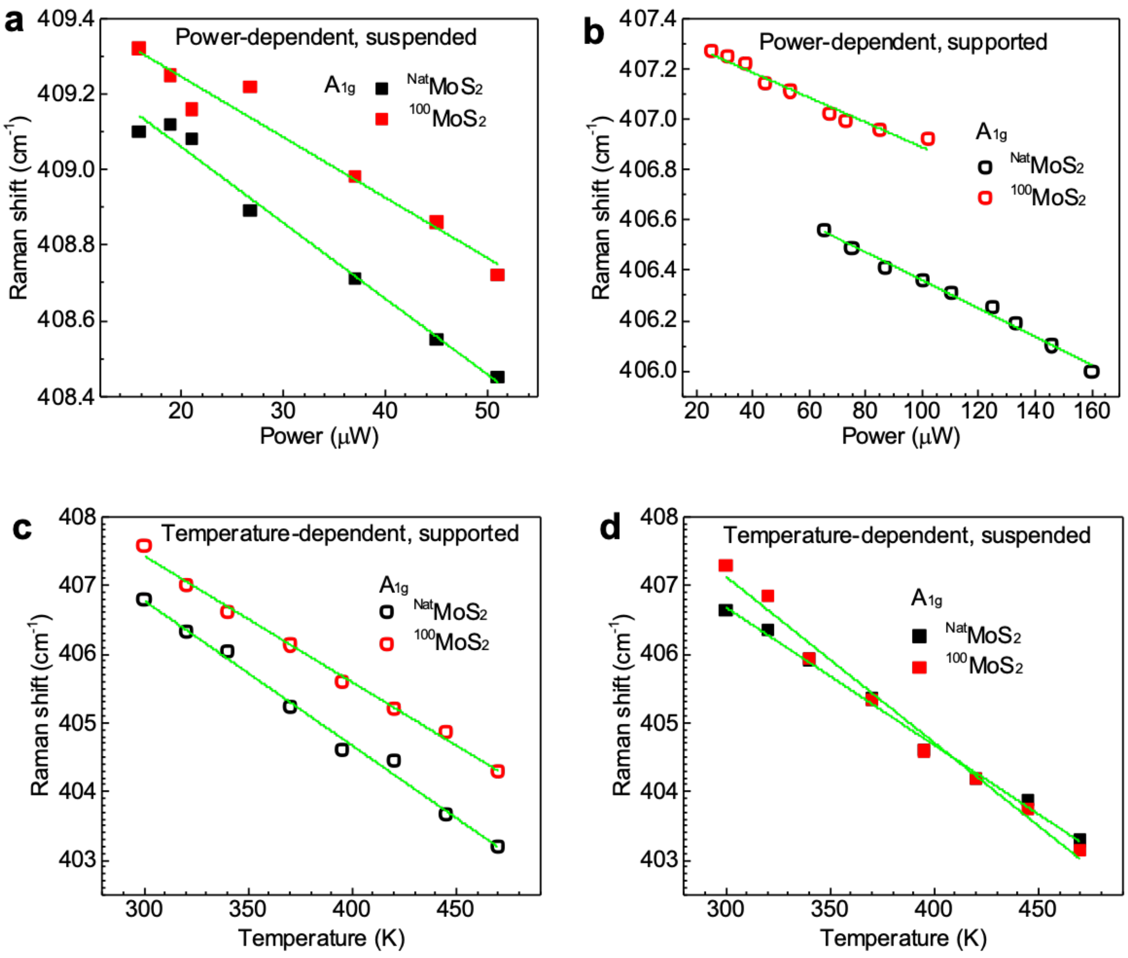

Figure 2.7: Excitation laser power-dependent energy of A_1g mode of (a) suspended $^{Nat}MoS_2$ (black scattered symbols), $^{100}MoS_2$ (red scattered symbols) and (b) supported $^{Nat}MoS_2$ (black scattered symbols), $^{100}MoS_2$ (red scattered symbols) monolayers at room temperature. Temperature-dependent energy of A_1g mode of (c) suspended $^{Nat}MoS_2$ (black scattered symbols), $^{100}MoS_2$ (red scattered symbols) and (d) supported $^{Nat}MoS_2$ (black scattered symbols), $^{100}MoS_2$ (red scattered symbols) monolayers at a fixed excitation laser (532 nm) power. The solid curves are the linear fitting. This figure is reproduced from ref. [44]. The Raman measurements data are provided by Xufan Li and Prof. Kai Xiao from CNMS, Oak Ridge National Lab.

The MoS_2 monolayer that is more isotopically enriched shows a smaller χ_P and larger χ_T values, and thus a lower thermal resistance ($R_m = \chi_P/\chi_T$) (Figure 2.7(a)–(d) and Table 1), suggesting the highest in-plane thermal conductivity is in $^{100}MoS_2$ monolayers, followed by the 50% $^{100}MoS_2$, and $^{Nat}MoS_2$. R_m also equals to the measured temperature versus

Table 1: Temperature coefficient (χ_T), power coefficient (χ_P), thermal resistance (R_m), of Si_3N_4-supported and suspended MoS_2 monolayers, and the suspended thermal conductivity (κ_{sus}) of the monolayer. The theoretical suspended thermal conductivity using first-principles calculation (CAL.), as well as the values reported previously (ref. [40, 69]) are also presented for comparison. This table is reproduced from ref. [44].

Materials	χ_T(cm^{-1}/K)		χ_P(cm^{-1}/μW)		R_m(K/μW)		κ_{sus} (W/mK)
	Supported	Suspended	Supported	Suspended	Supported	Suspended	
$^{Nat}MoS_2$	-0.0211± 0.0007	-0.0201± 0.0006	-0.0056± 0.0002	-0.020± 0.001	0.2654± 0.0007	0.995± 0.020	40.8± 0.8
$^{100}MoS_2$	-0.0184± 0.0006	-0.0242± 0.0012	-0.0049± 0.0004	-0.016± 0.002	0.2663± 0.0131	0.661± 0.050	61.6 + 5.6/ -4.0
$^{Nat}MoS_2$ (CAL.)	-	-	-	-	-	-	87.81
$^{100}MoS_2$ (CAL.)	-	-	-	-	-	-	100.52
$^{Nat}MoS_2$ (ref. [47])	-	-0.013	-0.010	-0.0109	-	0.769	34.5
$^{Nat}MoS_2$ (ref. [40])	-0.0167 (Au/SiO_2-supported)	-0.0203	-0.0204 (Au/SiO_2-supported)	-0.00987	4.862	1.222	84

total absorbed laser power (T_m/P), which was subsequently used to calculate the values of thermal conductivity of the MoS_2 monolayers based on the equations established in previous reports [40, 43, 47]. As a result, the in-plane thermal conductivity (κ_{sus}) of the suspended $^{100}Mo_2$ and 50% $^{100}Mo_2$ monolayers are 61.6 ± 6.0 W/mK and 52.8 ± 2.4 W/mK, respectively, showing a 50% and a 30% enhancement compared with the $^{Nat}Mo_2$ (40.8 ± 0.8 W/mK). Both of these values may be underestimated due to our assumption that all phonon modes probed by the Raman thermal measurement are in equilibrium. However, the reduced thermal resistance R_m in enriched Mo_2 indicates that the enhancement should not be underestimated. Our results demonstrate that the in-plane thermal conductivity is enhanced in crystals containing pure Mo isotopes, which could be due to a reduction in phonon scattering.

In our thermal conductivity calculation, we used the temperature- and power-dependence of the A_{1g} mode because it is insensitive to in-plane strain, and does not significant affact its Raman frequency from the substrate. Note that the A_{1g} mode is independent of the mass of Mo isotopes under only a harmonic approximation, but is strongly sensitive to local temperature variations due to thermal expansion. Therefore, it can be used as a direct measurement for the thermal conductivity. To determine κ_{sus} using our calculations, we also need to measure χ_T and χ_P in the monolayer region supported by the Si_3N_4 film (Figure

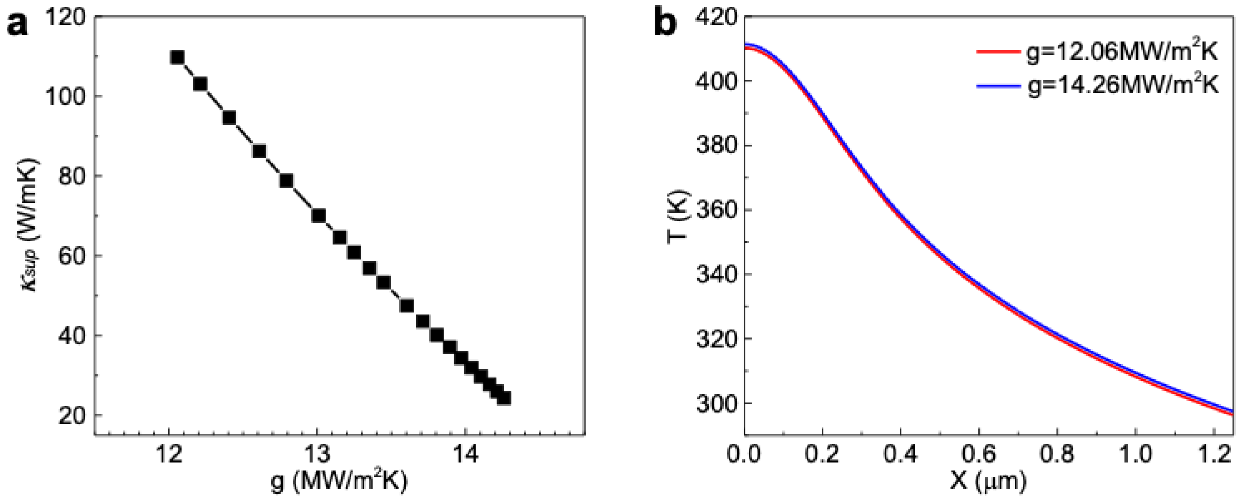

Figure 2.8: (a) Dependence of the supported thermal conductivity on the interfacial thermal conductance between the MoS_2 monolayers and Si_3N_4 film. (b) Local temperature distribution in the MoS_2 monolayers with different interfacial thermal conductance. This figure is reproduced from ref. [44].

2.7(b)(c)). Note that the R_m (χ_P/χ_T) of supported Mo_2 monolayers includes a relationship between g (the interfacial thermal conductance between the monolayers and Si_3N_4) and κ_{sup} (in-plane thermal conductivity in the supported monolayers), which is needed in the calculation of κ_{sus} (see detailed calculation methods). As shown in Table 1, the R_m values for the supported $^{\mathrm{Nat}}Mo_2$ and $^{100}Mo_2$ monolayer under the same external conditions are almost the same, which means that if the interfacial thermal conductance is insensitive to the Mo isotopes in the Mo_2 monolayers, the κ_{sup} of $^{\mathrm{Nat}}Mo_2$ and $^{100}Mo_2$ monolayer are similar. Within a reasonable range of κ_{sup} from 24.3 to 110 W/mK for monolayer Mo_2 supported by the Si_3N_4 film, [47] the g value varies only from 14.26 to 12.06 MW/m^{2}K (Figure 2.8). By solving the radial heat diffusion equation using these g and κ_{sup} values (see detailed calculation methods), κ_{sus} of the Mo_2 monolayers is seen to vary only by less than 3% (i.e., from 40.0 to 40.8 W/mK for $^{\mathrm{Nat}}Mo_2$ and from 60.8 to 62.4 W/mK for $^{100}Mo_2$). This also indicates that the local temperature distribution in the Mo_2 monolayers is independent of the interfacial thermal conductance, as shown in Figure 2.8. This phenomenon is consistent with a previous report on monolayer Mo_2 supported by the Si_3N_4 film. [47]

The thermal conductivity change induced by isotopic compositions in Mo_2 monolayers

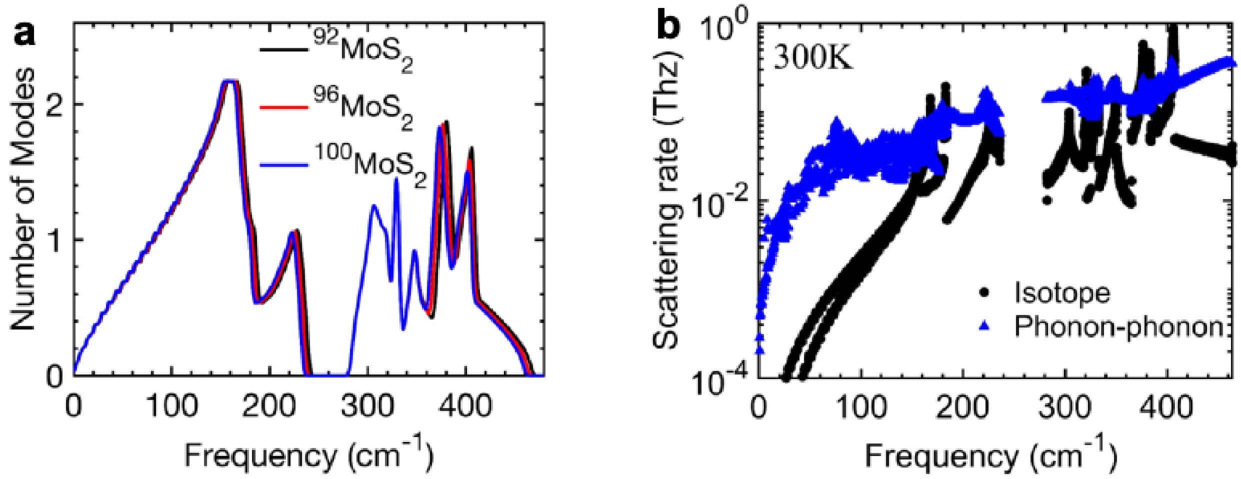

Figure 2.9: (a) The number of modes in Mo-isotopically enriched $^{92}MoS_2$, $^{96}MoS_2$ and $^{100}MoS_2$ monolayers calculated using Non-Equilibrium Green's Functions with first principles parameters. (b) Phonon-phonon scattering rates (blue symbols) and isotopic scattering rates (black symbols) at 300 K. This figure is reproduced from ref. [44].

can be caused by the following mechanisms: harmonic (ballistic) properties including the frequency spectrum, the difference in the number of modes (i.e., conducting channels), and the difference in scattering-based mechanisms including phonon-phonon and isotope scattering. To find the dominant mechanism, we first used the Non-Equilibrium Green's Functions (NEGF) with first-principles parameters to obtain the number of modes in Mo-isotopically pure $^{92}MoS_2$, $^{96}MoS_2$, and $^{100}Mo_2$ monolayers (Figure 2.9). The number of modes shows trivial differences as a result of the mass difference of Mo. Since the ballistic thermal conductivity can be expressed as the sum of all the conducting modes over the whole frequency spectrum (Eq. 2.1), the ballistic thermal conductivity should also show a small difference due to the mass difference of isotopes.

Next, we calculated the in-plane thermal conductivity of the $^{92}MoS_2$, $^{96}MoS_2$, $^{100}Mo_2$ and $^{Nat}Mo_2$ monolayers using self-consistent Boltzmann Transport Equations (BTE) by considering multiple scattering mechanisms. [62] Convergence is achieved when the relative change in thermal conductivity is less than 10^{-5}. The self-consistent calculations, beyond the relaxation time approximation, are performed to make sure the scattering processes only take into account the backscattering phonons. Phonon-phonon scattering is included for $^{92}MoS_2$,

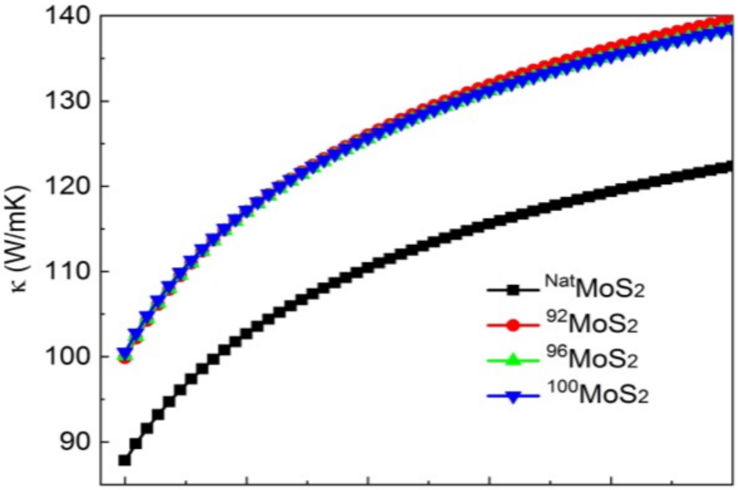

Figure 2.10: First-principles calculations of thermal conductivity of monolayer natural and Mo-isotopically enriched MoS2 as a function of sample length. The $^{92}MoS_2$, $^{96}MoS_2$, and $^{100}Mo_2$ only consider phonon-phonon scattering and boundary scattering, while $^{Nat}MoS_2$ also includes extra isotope scattering. This figure is reproduced from ref. [44].

$^{96}MoS_2$, and $^{100}Mo_2$ monolayers, while isotope scattering is also included in calculating the thermal conductivity of the $^{Nat}Mo_2$ monolayer. Boundary scattering, or the classic size effect, is considered by comparing the mean-free-path (MFP) λ versus the sample size L in the Landauer equation (Eq. 2.1). The sample sizes are varied from 1μm to 6 μm to match the experimental sample parameters. This modified Landauer method can cover the transport regimes all the way from the ballistic regime, when the MFP is much larger than the sample size (average transmission $\bar{T} = \frac{\lambda}{\lambda+L} \approx 1$, $\lambda \gg L$), to the diffusive regime when the MFP is much smaller than the sample size (average transmission $\bar{T} = \frac{\lambda}{\lambda+L} \approx \frac{\lambda}{L}$, $\lambda \ll L$). Our results are shown in Figure 2.10. The in-plane thermal conductivities of the Mo-isotopically pure $^{92}MoS_2$, $^{96}MoS_2$, and $^{100}Mo_2$ monolayers do not show significant difference (Figure 2.10, blue, green, and red lines), and are at 100 W/mK at 1 μm, matching the experimental dimensions (1 μm radius of suspended monolayers). The result suggests that the small mass difference in isotopes does not lead to enough changes in dispersion or phase space to significantly affect phonon-phonon scattering. Unlike phonon-phonon scattering, once the multiple Mo masses as in natural Mo_2 are considered, the thermal conductivity (Figure

2.10, black curve) is significantly reduced (87.81 W/mK at 1 μm length) compared to those Mo-isotopically enriched ones. This is because the mass deviation from the average due to Mo isotopes acts as a perturbation that induces a scattering mechanism into the materials, referred to as isotope scattering, which greatly shortens the phonon lifetime τ (Figure 2.9(b)) and MFP, and hence reduces the thermal conductivity. The MFP is expressed as $\lambda = \frac{2\langle \tau \nu^2 \rangle}{\langle |\nu| \rangle}$, as introduced in the previous section. The strength of isotope scattering rates $\frac{1}{\tau_{iso}}$ is of the same order of magnitude as the phonon-phonon scattering rates $\frac{1}{\tau_{ph-ph}}$ at 300 K for phonons with wavenumber larger than 150 cm^{-1}, as shown in Figure 2.9(b), thereby greatly reducing the lifetime and MFP for those phonons. Based on the above analyses, the increased thermal conductivity in the Mo-isotopically pure Mo_2 monolayers is attributed to a reduced isotope scattering.

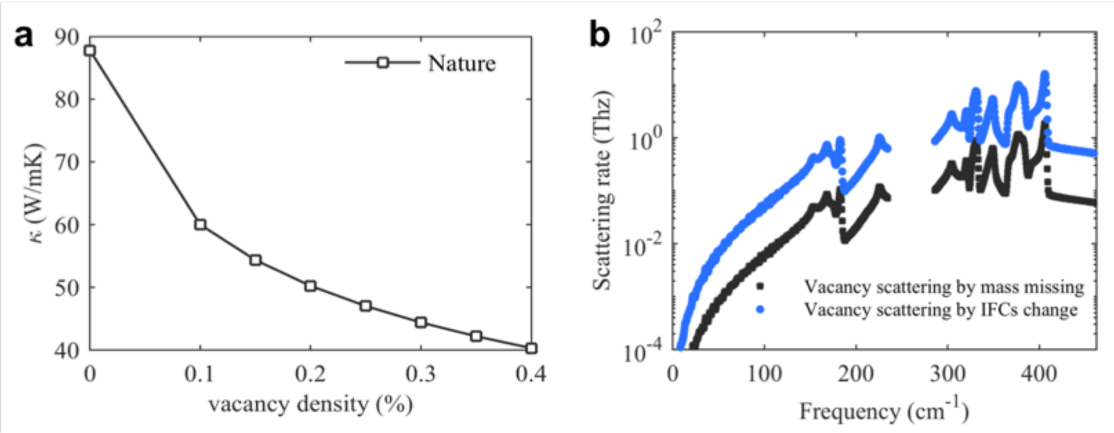

Figure 2.11: (a) Calculation of thermal conductivity at 1 μm sample size $^{Nat}MoS_2$ monolayer due to S vacancies. (b) Vacancy scattering (due to missing mass (black) and a change in interatomic force constants (IFCs) around the missing atoms (blue)) for 0.4% mole fraction of S vacancies. This figure is reproduced from ref. [44].

We also considered the influence of S vacancies on thermal conduction. Figure 2.11 shows the thermal conductivity of $^{Nat}MoS_2$ versus concentration of S vacancies. A small amount of vacancy defect significantly suppresses the thermal transport in MoS_2 (Figure 2.11(a)) with major contributions from scattering of high frequency phonons (Figure 2.11(b)). Note that the typical density of S vacancies in MoS_2 is around 1–2%, whereas in this calculation 0.3–0.4% density of S vacancies decreases the thermal conductivity to 40–45 W/mK (the range of ${}^{\mathrm{Nat}}\mathrm{MoS}_2$ thermal conductivity measured in this study). This is due to the overestimation of the scattering rates of high frequency phonons by Klemen's formula. [77, 78]

2.5 Conclusion

By combining the number of modes from Non-Equilibrium Green's Function calculations with mean free paths from iterative Boltzmann calculations, we calculated and compared thermal conductivities of TMDs from the ballistic to the diffusive regime. A reverse of order is seen for the thermal conductivity between MoS_2 and WS_2 at a sample size of 38.8 nm, and between MoSe_2 and WSe_2 at a sample size of 51.5 nm. This inversion arises from the trade-off between the frequency spectral range and the anharmonic scattering strength. Interestingly, we discovered a significantly high scattering rate in optical modes in MoSe_2, originating from its unique phonon dispersion. The mid-frequency optical modes in MoSe_2 lie around the middle of the gap between high-frequency optical modes and acoustic modes, enabling the decay process of the high-frequency modes to acoustic ones while conserving overall energy. As a result, MoSe_2 can exhibit the smallest diffusive thermal conductivity while WS_2 can show the largest thermal conductivity, with the increasing sample size and temperature. This systematic study of all four TMDs family members in both the ballistic and the diffusive transport regimes provides a full picture of anharmonic scattering rates, mean free paths, and phonon decay channels. These results show how by manipulating the composition of metal chalcogen atoms, sample size, isotopes and temperatures, we can tune the thermal properties in 2-D TMDs for applications ranging from 2-D electrons, photonics, spin- and valley-tronics, thermoelectricity and quantum information sciences.

Chapter 3

Interfacial thermal bridges: harmonic to anharmonic

3.1 Introduction

In the previous chapter, we discussed phonon transport in homogeneous bulk TMDs, where only the mode average transmission $\bar{T}$ changes between the ballistic and diffusive regimes. In this chapter, we move on to phonon transport across a hetero-structure, specifically an intermediate layer bridging interface, where both M and $\bar{T}$ vary between the harmonic and anharmonic limits.

The miniaturization of modern semiconductor devices to the nanoscale has led to a significant increase in heat density in integrated circuits [3, 79, 80]. The accumulated heat is challenging to dissipate due to the elevated thermal resistance resulting from a large number of material interfaces. Currently, the resistance at a single interface can account for up to 30-40% of the total device thermal resistance, as in the case of the GaN/SiC interface in GaN high electron mobility transistors [81]. The resistance to heat dissipation caused by interfaces is an important bottleneck towards the further scaling of semiconductor devices. However, the existing gap in our fundamental understanding of heat transfer across single and multiple interfaces in nanostructures hinders the development of effective thermal management methodologies. [1, 2, 82]

One promising approach to decreasing the thermal resistance at an interface is adding a bridging layer or intermediate thin film at the interface (Fig. 3.1(a)) [58, 83–87]. This can effectively enhance interfacial thermal conductance by bridging either acoustic impedances (ie. enhancing phonon transmission) or the phonon frequency spectra (ie. enhancing the phonon frequency range by inelastic transport) [84, 86, 88–90]. Nevertheless, the advantage of a bridging layer only exists in the 'additive' regime, that is, when the total resistance can be treated as the sum of the resistances at the boundaries and the intrinsic resistance of the added layer. For instance, in the harmonic limit, where this assumption cannot be made, conductance is limited by the available modes that can conserve both energy and transverse (parallel to the interface) momentum across the materials composing the bridged interface. As a result, the bridging layer, in the non-additive harmonic regime, decreases the number of available modes, and limits the possibility of enhancing the thermal conductance, G, for many combinations of materials. [58, 59, 88]

The transition from the non-additive to the additive regimes relies on anharmonic phonon-phonon scattering processes, and thus on the length of the intermediate layer, L, on the strength of the anharmonicity V_0 (the third order expansion of the interatomic potential energy $\frac{\partial E}{\partial r_i r_j r_k}$) , and on the temperature, $\mathbf{T}$. A comprehensive study on how phonons flow across bridged interfaces in different transport regimes, accessible by varying these parameters, is still missing. Such a study could clarify how different scattering processes determine the transition between additive and non-additive regimes and thus enable better thermal engineering of devices.

The critical length scale at which the additive regime is valid is of significant importance for measurements of thermal conductivity of thin films, typically sandwiched between two bulk materials. Extraction of the thermal conductivities of these thin films, e.g. by time-domain thermoreflectance (TDTR) or Raman spectroscopy [91–93], normally relies on the assumption that the total resistance can be treated as a summation of resistances in series. The validity of summing resistances is usually determined by comparing the bulk mean free paths (MFPs) with the thin film thicknesses. In many cases, however, the comparison is difficult, as thicknesses of the thin films are often on the order of nanometers while the bulk phonon MFPs span a wide range of scales from nanometers to micrometers. Under these conditions, it is debatable whether the comparison between the bulk MFPs and the thin film thickness is an accurate measure to determine the transport regimes. In this work, we vary the thin film thickness under different temperatures to determine the length scales at which the additive regime is valid. These length scales are then compared with the bulk MFPs to validate the role of bulk MFPs in determining the various transport regimes.

In sec. 3.2, the thermal transport across a prototype model argon–bridge–“heavy argon” interface (Fig. 3.1(a)) is investigated, with varying layer thickness, L, and temperature, $\mathbf{T}$. Our results demonstrate the existence of a minimum interfacial thermal conductance, G, with L when anharmonicity is weak (low $\mathbf{T}$), and the existence of a maximum G with L when anharmonicity is strong (high $\mathbf{T}$) (Sec. 3.2.4). The minimum thermal conductance at low $\mathbf{T}$ appears at a short L and is due to the competing roles of phonon tunneling and thermalization. The maximum thermal conductance at high $\mathbf{T}$ is a result of two competing effects of anharmonicity: thermalization and Umklapp scattering. We show that the effect of anharmonicity on the conductance can be tuned by varying temperature or intermediate layer thickness, as both parameters can change the number of phonon-phonon scattering processes. In Section 3.2.5, we study the critical length, L_s, at which the total resistance can be separated into components as resistances in series. Additionally, we compare the critical length with the bulk MFPs λ_b, and demonstrate that L_s is much smaller than λ_b, suggesting that the additive regime can be extended to much smaller length scales than the bulk mean free path, contrary to popular wisdom.

In sec. 3.3, we introduce a new design rule for solid-solid interfaces to potentially best enhance interfacial thermal transport: nano-engineered, exponentially mass-graded interfaces.

We extend our results on size effects to this special multilayer system. Our simulations confirm the key role played by anharmonic phonon-phonon interactions on interfacial phonon transport and show how the conduction changes with dimensions of the interface.

Much like the single interface system, in the harmonic limit, increasing the number of layers of the multilayer system, results in better acoustic impedance matching at the boundaries and higher phonon transmission at those individual interfaces, thus facilitating thermal transport. On the other hand, adding more layers in the junction decreases the number of transport channels, eventually hindering the transport. These opposing actions thus result in increasing the overall conductance initially, then turning into an asymptotic saturation of thermal conductance when the number of layers is large. At low temperature, our results exhibit an increase in thermal conductance as the junction thickness increases, contradicting the usual expectation of decreasing conductace with thickness. This surprising trend is caused by phonon thermalization via anharmonic processes in the neighborhood of material boundaries, which enhances thermal boundary conductance beyond the expected intrinsic decrease. Our results suggest that the influence of a mass-graded junction on thermal conductance is dominated by the phonon thermalization through anharmonic effects, while elastic phonon transmission due to better impedance matching plays a secondary role.

Our findings contribute to the fundamental understanding of thermal transport across phonon-mediated solid-solid interfaces, a phenomena not yet fully understood. Using this knowledge, we introduce an efficient approach to enhance the interfacial thermal conductance, optimizing the , which can be critical in the design of more efficient heat dissipation devices, nanostructures and other applications from CNET self driven shades etc.

3.2 Size effects on single layer bridged interfaces

3.2.1 Methodology

Figure 1(a) depicts the system studied in this paper, a “bridged interface.” The left and right contacts as well as the bridge layer share the same face-centered cubic (fcc) crystal structure with interatomic interactions given by the same Lennard-Jones potential. The boundaries between adjacent materials are abrupt and clean without any lattice mismatch or defects. The atomic masses of the left and right materials are $m_l = 40$ amu and $m_r = 120$ amu respectively, and the atomic mass of the bridge layer is the geometric mean $m_b = \sqrt{m_r m_l}$ of those two. This choice of m_b maximizes the enhancement of the conductance by a bridge layer in the ‘additive’ regime. [59, 88] Since the additive resistance at each interface depends on the mass ratio, the optimal total resistance is when the mass ratios are equal, giving the geometric mean. The dissimilar atomic masses cause different vibrational properties in those materials. To study the dependence of conductance on the intermediate layer thickness and to determine the critical length L_s to separate the resistances, the bridge layer thickness is varied from 1 to 60 conventional unit cells (lattice constant a is 0.522 nm), and the temperature $\mathbf{T}$ is set to 0 K, 2 K or 30 K. Further details of the system are provided in section 3.2.2.

By changing temperature, $\mathbf{T}$, we calculate thermal conductance across the system in three regimes: without anharmonicity ($\mathbf{T}$=0 K), with weak anharmonicity ($\mathbf{T}$=2 K), and with strong anharmonicity ($\mathbf{T}$=30 K). Conductance at $\mathbf{T}$=2 K, without any anharmonic interactions, is computed using the Landauer formalism according to

$$G_{GF} = \frac{1}{A}\int_0^\infty \frac{\hbar\omega}{2\pi}\frac{\partial N}{\partial \mathbf{T}} M\bar{T} d\omega \xrightarrow[\text{limit}]{\text{classical}} \frac{k_B}{2\pi A}\int_0^\infty M\bar{T} d\omega, \tag{3.1}$$

where A is the cross-sectional area, $\hbar$ is the reduced Planck constant, N is the Bose–Einstein distribution, k_B is the Boltzmann constant, M is the number of available propagating modes and $\bar{T}$ is the average transmission per mode. $M\bar{T}$ is determined using Non-Equilibrium

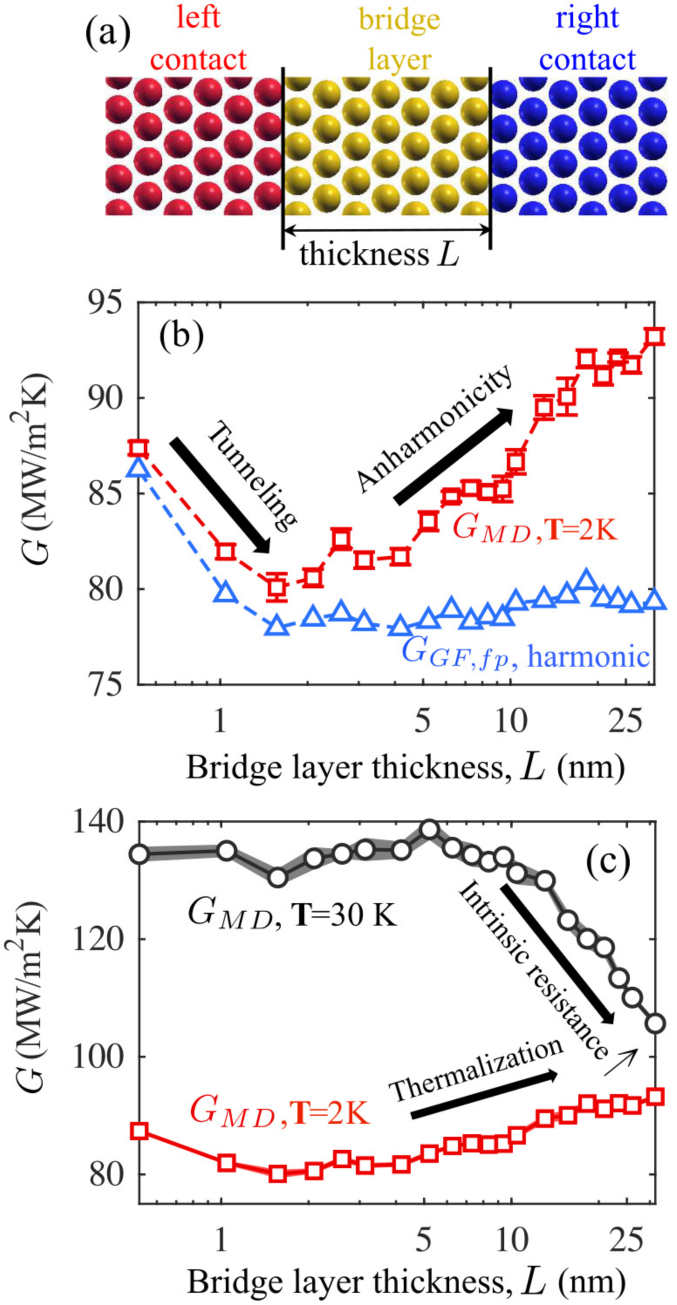

Figure 3.1: (a) Schematic of a bridged interface. The bridge layer mass is the geometric mean of masses of the materials at the interface $m_b = \sqrt{m_l m_r}$. This choice of the bridge layer mass can maximize the enhancement of the interfacial thermal conductance G in the 'additive' limit. [59,88] (b) The calculated interfacial thermal conductance in the harmonic limit, $G_{GF,fp}$,(blue triangles) decreases to saturate with L, while conductance with weak anharmonicity G_{MD}, **T**=2 K shows a minimum. (c) The conductance with strong anharmonicity G_{MD}, **T**=30 K shows a maximum. The shad in (c) denote the uncertainty based on 5 sets of NEMD simulations. We attribute the rise in the former (red squares) due to thermalization, and the drop in the latter (black circles) due to Umklapp scattering.

Green's Function (NEGF) by $M\bar{T} = \text{Trace}[\Gamma_l \mathbf{G} \Gamma_r \mathbf{G}^\dagger]$, with $\mathbf{G}$ the retarded Green's function and Γ_l (Γ_r) the broadening matrix describing the interactions between the device—in this case, the bridge layer—and the left (right) contact material. The number of modes in each individual bulk material ($M_{l/b/r}$ left, bridge and right materials) can be determined using the same method for calculating $M\bar{T}$ but with the contacts and device chosen as the same material, in which case, the average transmission $\bar{T}$ is unity for each mode. Conductance including weak and strong anharmonicity are computed using Non-Equilibrium Molecular Dynamics (NEMD) at $\mathbf{T}$=2 K and $\mathbf{T}$=30 K respectively. Details of our NEGF and NEMD simulations are presented in section 3.2.2, including tests checking for domain size effects. (G_{GF} in this paper denotes the harmonic conductance without any anharmonic interactions, but in principle NEGF can include anharmonic interactions despite the simulation is computationally expensive. [94,95]) To calibrate the conductances from NEGF (G_{GF}) and NEMD (G_{MD}), the high temperature limit of Eq. 3.1 is used in NEGF calculations ($\hbar\omega_{max} \ll k_B\mathbf{T}$, with ω_{max} the maximum vibrational frequency of the system), so that phonons across the whole spectrum contribute equally to transport as in the classical limit. Furthermore, contact resistance is excluded from G_{GF} using

$$G_{GF,fp} = G_{GF}\frac{\Delta\mathbf{T}_c}{\Delta\mathbf{T}_i}, \tag{3.2}$$

,where $\Delta\mathbf{T}_i$ and $\Delta\mathbf{T}_c$ are temperature differences at the interface and between the contact baths in NEMD simulations at $\mathbf{T}$=2 K, as illustrated in Fig. 3.2(a) of the section 3.2.3. In this way, the two-probe conductance measurement from NEGF is converted to a four-probe measurement that captures only temperature drops at the interface. The four probe conductance in NEGF without using the temperature differences from NEMD is provided in sec. 3.2.3. NEMD simulations were performed by Rouzbeh Rastgar from the Norris research group at UVa.

3.2.2 Simulation Details

We study thermal transport across bridged interfaces shown in Fig. 1(a). In this study, all material properties (interatomic potentials, crystal structures and lattice constants) except the atomic masses stay invariant throughout the whole system. The crystal structure for the three components is face-centered cubic, with one atom per primitive unit cell, and the lattice constant a is 0.522 nm. Interfaces are abrupt, free of defects and without any lattice mismatch. The atomic mass in the bridge layer is the geometric mean of the contact masses $m_b = \sqrt{m_l m_r}$ (m_l=40 amu, m_r=120 amu and m_b=69.28 amu), thus its impedance and vibrational spectrum bridge those of the contacts. The bridge layer thickness L is varied from 1 u.c. (a) to 60 u.c. (a), and the ambient temperature is set to either 0 K, 2 K or 30 K.

The Lennard-Jones (LJ) potential is used to describe the interatomic interactions: $U_{LJ}(r_{ij}) = 4\epsilon[(\sigma/r_{ij})^{12} - (\sigma/r_{ij})^{6}]$, with parameters $\epsilon = 0.0503$ eV and $\sigma = 3.37$ Å. These parameters are identical to those in our previous works. [59, 88] The cut-off distance for the potential is 2.5σ, which includes atomic interactions up to 5^{th} nearest atomic neighbors. In our harmonic Green's function calculations, the interatomic force constants come from the 2^{nd} order expansion of the same LJ potential, and the interactions also include up to 5^{th} nearest atomic neighbors. To benchmark the two methodologies used to compute thermal conductance, NEMD and NEGF simulations, we calculate the conductance of an abrupt interface, without the bridge layer. The conductance of such a system given by NEMD at 2 K, G_{MD} is 71.71±0.36 MWm^{-2}K^{-1}, and given by harmonic NEGF without contact resistances (by approach (b) in sec. 3.2.3) in the classic limit G_{GF} is 70.14 MWm^{-2}K^{-1}. These values show excellent agreement with each other, allowing us to compare results from these two methods.

NEGF simulations are performed with 200 grid points, sampling the frequency interval from 0–40 Trad s^{-1} and a 100×100 wavevector mesh, sampling the Brillouin zone of an FCC conventional unit cell. All simulation results exclude the contact resistances (see details in sec. 3.2.3).

NEMD simulations are performed using the LAMMPS software with a domain size of $10 \times 10 \times 302$ conventional unit cells. [96] One atomic layer at each end of the domain is set as a wall, and periodic boundary conditions are imposed along x and y directions. Langevin thermostat is used to add heat from the left side and remove heat from the right side with 2 fs time step. The bath at each side is 50 unit cells thick, and the bath temperature is maintained at $\mathbf{T}_{bath} = (1 \pm 0.1)\mathbf{T}$ with a time constant of 1.07 ps. Such thermostat setup ensures sufficient phonon-phonon scattering to prevent potential size effects at low temperatures. Following previous work [59,88], comprehensive tests of size effects have been performed. The results for system sizes and temperatures relevant to the present work are summarized in Table 1, and no significant impact on the interfacial thermal conductance from those factors was observed.

Table 1: Size effect tests for NEMD simulations on the thermal conductance of a bridged interface ($\mathrm{MWm^{-2}K^{-1}}$). All these tests are done on a L=20 u.c. system using 5 independent simulations.

	G ($\mathrm{MWm^{-2}K^{-1}}$)			
Size (u.c.)	90	120	240	300
$\mathbf{T}$ = 2 K	84.39±0.53	85.18±0.36	86.71±0.21	86.66±0.63
$\mathbf{T}$ = 30 K	124.98±0.38	126.24±0.49	132.63±0.73	131.24±1.96

Thermal expansion of the system was also taken into consideration. To find the temperature dependence of the lattice constant $a(\mathbf{T})$, we fitted it to the following function using the isothermal-isobaric ensemble under zero pressures:

$$a(\mathbf{T}) = 5.2222 + 0.0004\mathbf{T} + 10^{-6}\mathbf{T}^2 - 4 \times 10^{-9}\mathbf{T}^3\text{Å}. \tag{3.3}$$

where $\mathbf{T}$ is in Kelvin. The thermal conductances reported in this paper are the average of 5 sets of simulations with randomly generated initial atomic velocities. The conductance is computed by dividing the heat flux over the temperature drop across the bridge interface ($\Delta\mathbf{T}_i$ in Fig. 3.2). The temperatures at the edges of the contacts used to calculate $\Delta\mathbf{T}_i$ result from a linear extrapolation of the temperature profile within each contact.

3.2.3 Temperature profile and contact resistance

The harmonic thermal conductance calculated using the Landauer formula (Eq. 3.1) yields a two-probe measurement of conductance, which is the heat flux over the temperature difference between the baths (shown as $\Delta\mathbf{T}_c$ in Fig. 3.2(a)). To convert this value to a four-probe measurement of conductance using the temperature difference immediately at the interface ($\Delta\mathbf{T}_i$ in Fig. 3.2(a)), we deduced the contact resistances following two approaches:

(a) To fairly compare calculations from NEGF with those from NEMD under weak anharmonicity ($\mathbf{T}$=2 K), we combined the temperature differences from NEMD simulations with Eq. 3.2. Thus, the four-probe conductance inferred from NEGF is given by $G_{GF,fp} = G_{GF}\frac{\Delta\mathbf{T}_c}{\Delta\mathbf{T}_i}$. The corresponding four-probe conductances $G_{GF,fp}$ are shown as blue triangular symbols in Fig. 3.1(b) and Fig. 3.3.

(b) Instead of using the temperature differences obtained from NEMD simulations, we can use the temperature differences in Green's function simulations. This requires assigning a temperature to the non-equilibrium distributions between the baths ($\mathbf{T}_{1e}$ and $\mathbf{T}_{2e}$ shown in Fig. 3.2(a)). Under the equilibrium assumption [87,97], $\mathbf{T}_{1e}$ and $\mathbf{T}_{2e}$ can be expressed as $\mathbf{T}_{1e} = \mathbf{T}_1 + (\mathbf{T}_2 - \mathbf{T}_1)G_{GF}/(2G_1)$ and $\mathbf{T}_{2e} = \mathbf{T}_2 - (\mathbf{T}_2 - \mathbf{T}_1)G_{GF}/(2G_2)$, where G_{GF} is the two-probe conductance for the whole system and, G_1 and G_2 are the conductances of the pure contact materials. As a result, the four-probe conductance can be written as [87,88,97]:

$$G_{GF,fp} = G_{GF} \times \frac{1}{1 - \frac{1}{2}[\frac{G_{GF}}{G_1} + \frac{G_{GF}}{G_2}]} \tag{3.4}$$

The four-probe conductances $G_{GF,fp}$ calculated by this method are shown as green triangular symbols in Fig. 3.3.

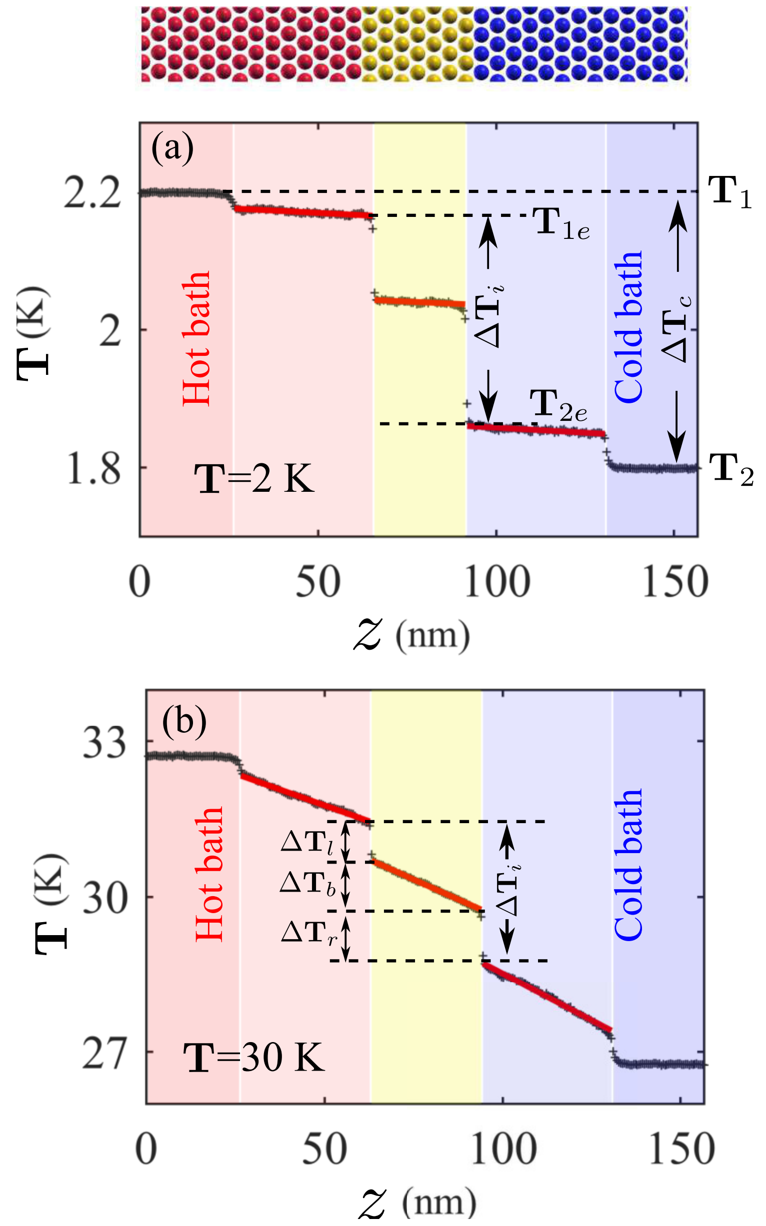

Figure 3.2: (a) The temperature profile at **T**=2 K when L=60 u.c.. $\Delta\mathbf{T}_i$ and $\Delta\mathbf{T}_c$ are temperature differences at the interface and between the bath contacts respectively. (b) The temperature profile at **T**=30 K when L=50 u.c.;$\Delta\mathbf{T}_l$ and $\Delta\mathbf{T}_r$ are the temperature drops at the left and right boundary respectively, $\Delta\mathbf{T}_b$ is the temperature drop within the bridge layer and $\Delta\mathbf{T}_i$ is the total temperature drop at the bridged interface.

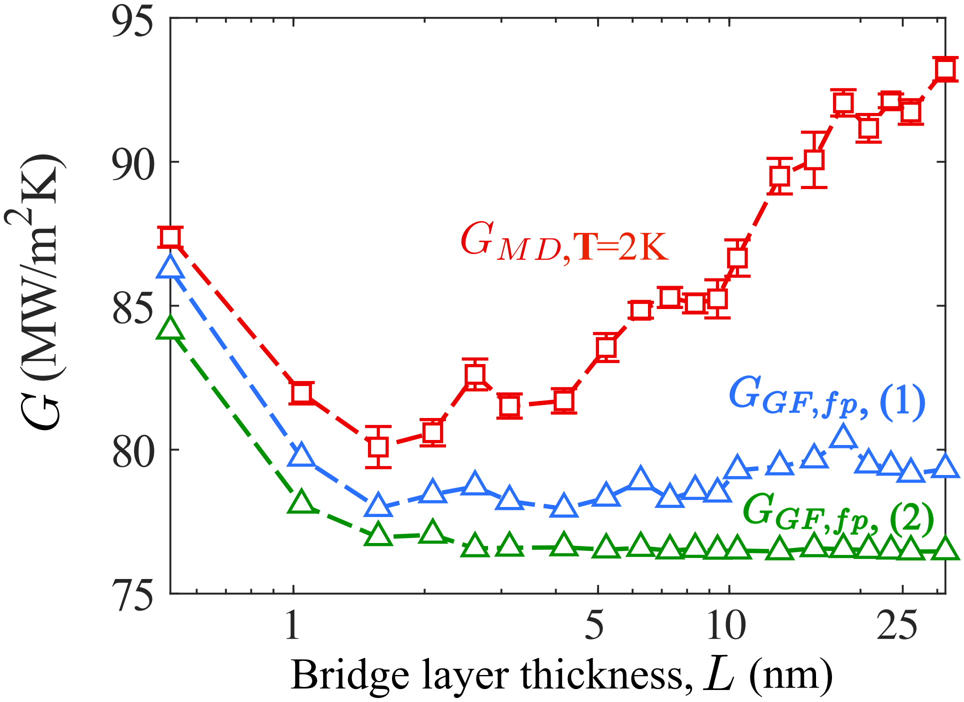

Figure 3.3: The interfacial thermal conductance in the harmonic limit by method (a) ($G_{GF,fp}$, (1)) and method (b) ($G_{GF,fp}$, (2)) in section 3.2.3, compared to the conductance with weak anharmonicity G_{MD}, **T**=2 K.

3.2.4 Minimum and maximum conductance versus bridge layer thickness

Depending on the anharmonic scattering rates (as controlled by temperature), the conductance across the bridged interface exhibits different trends as the thickness of the intermediate layer increases (Figs. 3.1(b) and 3.1(c)). With zero anharmonicity, $G_{GF,fp}$ initially decreases and quickly saturates at ~ 2 nm (Fig. 3.1(b)). With weak anharmonicity, an initial decrease of G_{MD} at **T**=2 K is followed by an upward trend (Fig. 3.1(b)), resulting in a local minimum in conductance with respect to bridge layer thickness. Finally with strong anharmonicity, G_{MD} at **T**=30 K decreases after ~ 5 nm following Fourier's law (Fig. 3.1(c)). In this section, each trend is explained in terms of three different transport mechanisms: phonon tunneling, thermalization processes, and intrinsic resistance by Umklapp scattering.

Phonon tunneling explains the decreasing trend of G versus L in the harmonic limit or at low temperature (**T**=2 K) in Fig. 3.1(b). By "phonon tunneling," we refer to a non-zero, elastic phonon transmission across a bridged interface via an evanescent vibrational wave in the intermediate (bridge) layer. Contrary to propagating waves, i.e. eigenvectors of the harmonic equation of motion whose amplitudes are constant along the crystal (normal phonons), evanescent waves decay exponentially in the crystal and thus cannot carry heat over long distances. Nevertheless, for layer thicknesses shorter than the decay length, evanescent waves can bridge propagating waves or phonons across two materials. [98, 99]

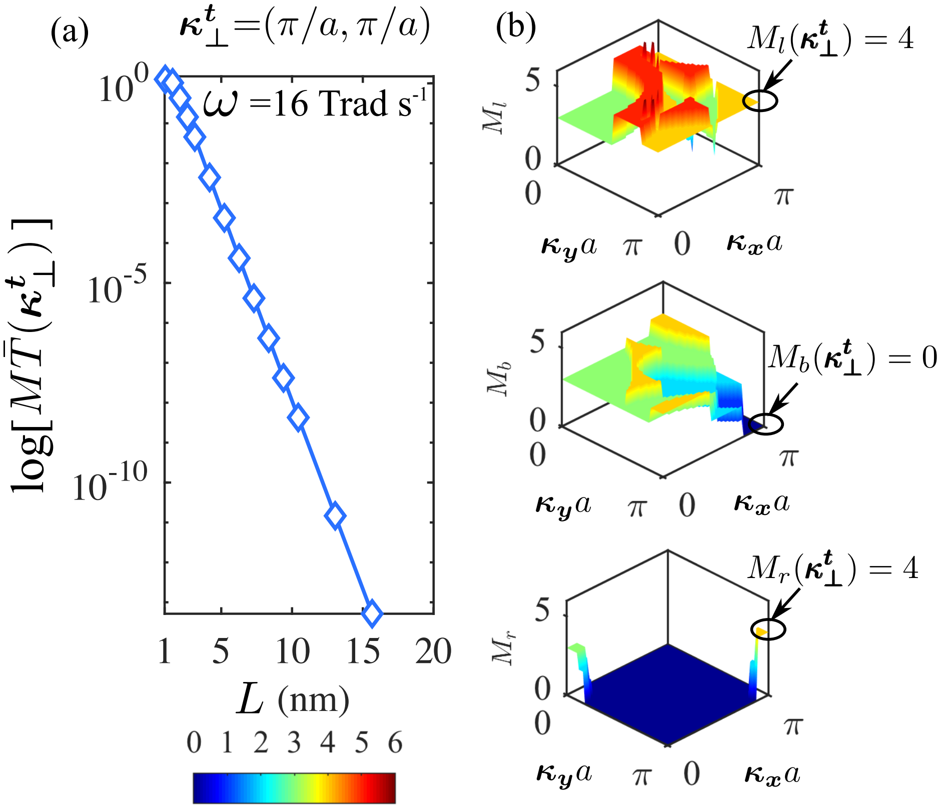

Figure 3.4: At frequency ω=1.6 Trad s^{-1}, (a) transmission for modes at $\boldsymbol{\kappa}^{\boldsymbol{t}}_{\perp}=(\pi/a,\,\pi/a)$ is an exponentially decaying function of L, where $a=0.522$ nm is the conventional unit cell lattice constant; (b) number of modes in the left (M_l), bridge layer (M_b) and right (M_r) material respectively, showing an absence of modes in the bridging layer (black circles) leading to tunneling.

Phonon tunneling can be unambiguously identified in the harmonic limit, where nonzero transmission across the bridged interface *is only possible if* phonons conserve energy and transverse wavevector $\boldsymbol{\kappa}_{\perp}$ (in the boundary plane). Conservation of $\boldsymbol{\kappa}_{\perp}$ results from the transverse symmetry of the abrupt material boundaries of our system free from impurities, defects, lattice mismatch or interatomic mixing. Phonons across such boundaries are not acted upon by any force in the transverse directions, and hence do not have any momentum (velocity) scattering in those directions.

Evidence of phonon tunneling in our system is given in Figure 3.4. Figure 3.4(a) shows $M\bar{T}$ versus L for phonons at frequency ω=16 Trad s^{-1} and transverse wavevector $\boldsymbol{\kappa}^{\boldsymbol{t}}_{\perp}$=$(\pi/a, \pi/a)$. $M\bar{T}$ arises from phonon tuneling because there are available propagating modes or phonons at $\boldsymbol{\kappa}^{\boldsymbol{t}}_{\perp}$=$(\pi/a, \pi/a)$ only in the left and right contact materials but not in the bridge layer (see circled regions in Fig. 3.4(b)). Thus vibrational energy transport across the bridge is only possible via evanescent modes. Also, $M\bar{T}$ decreases exponentially with length, are expected for heat-carrying evanescent waves. At $\boldsymbol{\kappa}^{\boldsymbol{t}}_{\perp}$=$(\pi/a, \pi/a)$ there are similar phonon tunnelling contributions to conductance for frequencies between 15 and 16 Trad s^{-1}, where propagating modes are available only in the contacts but not in the bridge (see Fig. 3.5).

Phonon tunneling sets in when the bridge modes at a given (ω,$\kappa_{\perp}$) fall significantly below the mode counts in the contacts, not just when the former is zero. The sum of the decaying transmission of all evanescent vibrations in the bridge material results in a decreasing trend of $M\bar{T}$ and thus of G_{GF} at short L (Fig. 3.1(b)). When the contribution to $M\bar{T}$ from phonon tunneling becomes negligible, $M\bar{T}$ and G_{GF} saturate because the Fabry-Perot oscillations in the transmission due to wave interference are partially destroyed by the sum over phonons with different wavelengths and then further averaged out by the integral over frequency.

Phonon tunneling and the initial decrease in G_{GF} vs. L can also be explained from another equivalent point of view from electrons, the Metal Induced Gap States (MIGS), using local density of states (LDOS). When L is very short, the LDOS in the bridge layer is permeated with levels from the contact materials that are not present in the DOS of the bulk bridge

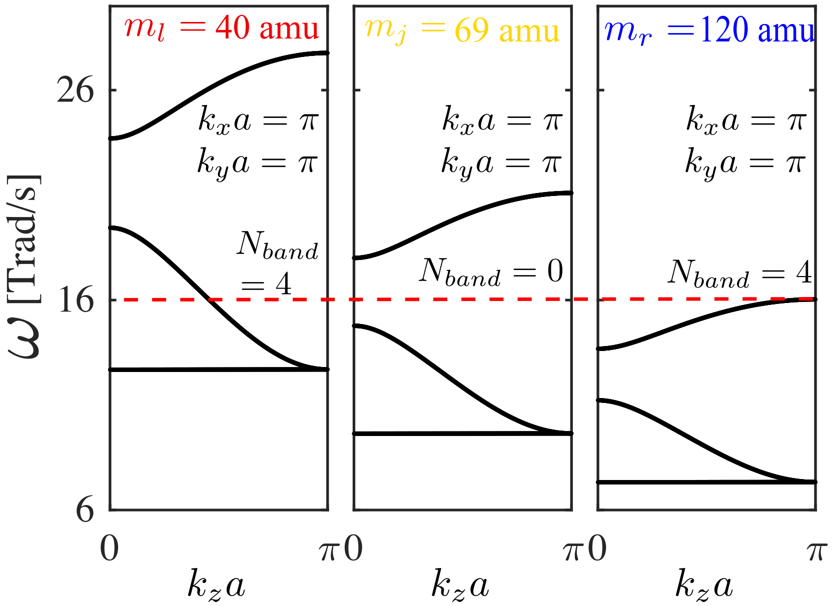

Figure 3.5: The projected phonon dispersion of left (red), right (blue) contact materials and of the bridge (yellow) layer when $\boldsymbol{\kappa}^{\boldsymbol{t}}_{\perp} = (\pi/a, \pi/a)$. In the frequency range $\omega \in (15 \sim 16)$ Trad s^{-1}, the number of phonon bands in the contacts is 4, while in the bridge layer is none. Thus non-zero $M\bar{T}$ in this range is due to phonon tunneling. There are four atoms in the fcc conventional unit cell, so each line represents 4 degenerate bands.

material, which may allow phonon transport across the interface. However, as L increases, the LDOS of atoms in the bridge layer away from the boundaries recovers the DOS of the bulk bridge material, and the extra transport levels assisting conduction disappear. This example emphasizes the importance of interfacial eigenmodes when considering transport. [100–102]

When weak anharmonicity is included ($\mathbf{T}$=2 K), conductance follows the harmonic limit behavior at short length, then deviates from it and starts increasing with L (Fig. 3.1(b)). This increase results from thermalization processes, which can be analyzed using the spatial energy distribution of normal modes (Fig. 3.6). To that end, we apply a wavelet transform on the time series of atomic velocities during MD simulations and obtain their kinetic energy density spectra as a function of both spatial position and wavevector; details of the calculation are the same as those in our previous publications. [103] The kinetic energy density along longitudinal $\langle 001 \rangle$ modes is converted to an equivalent temperature $\mathbf{T}_{\text{equiv}}(z, \boldsymbol{\kappa})$ and plotted

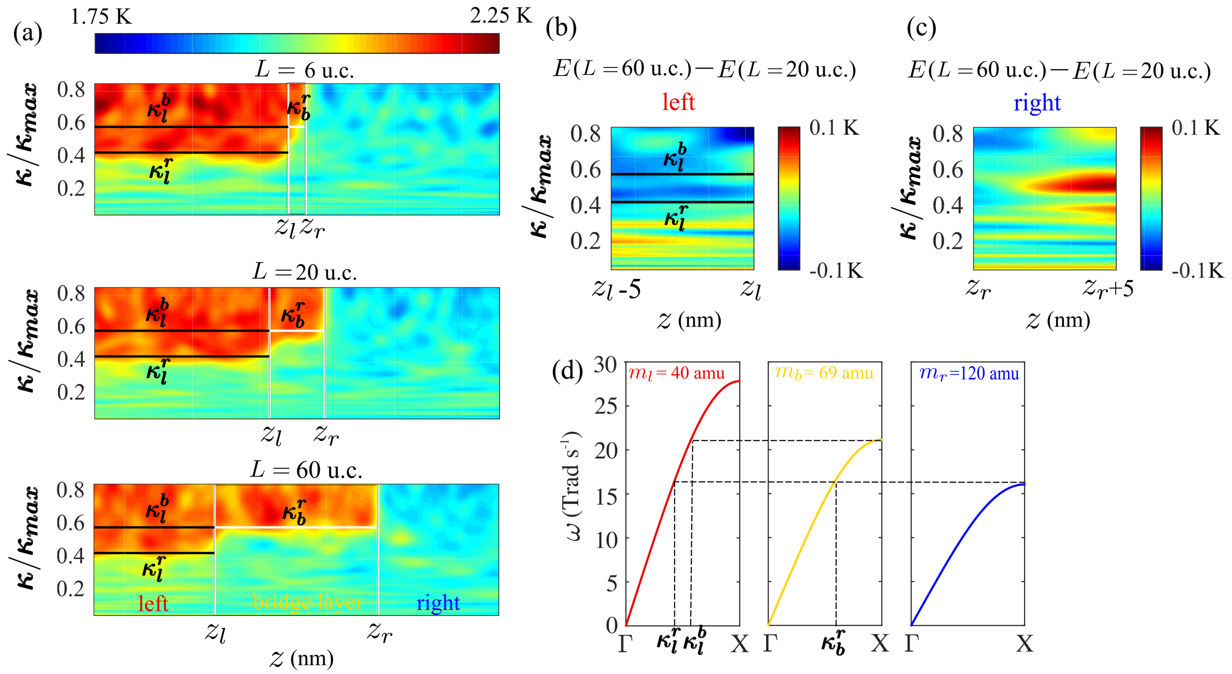

Figure 3.6: (a) The kinetic energy density distribution along longitudinal ⟨001⟩ modes when L is 6 u.c., 20 u.c. and 60 u.c. respectively. Modes with wavevector $\boldsymbol{\kappa_l^r}$ in left and $\boldsymbol{\kappa_b^r}$ in bridge layer material have the same frequency as the cut-off frequency in the heavy material (right contact material). z_l and z_r denote the location of the left and right boundaries. Phonons above the cut-off frequency of the heavy material accumulate in the left and in the bridge materials at 2 K. (b, c) The energy density difference between 60 u.c. and 20 u.c. systems at the 5 nm regions in the left and right materials close to the left boundary (z_l-5 nm to z_l) and right boundary (z_r to z_r+5 nm), showing signature of thermalizaiton where high frequency phonons on the left scatter to low frequency regimes and transport across the interface. (d) Dispersion curves of the longitudinal phonon branches in the three different materials and relationship with the critical wavevectors, $\boldsymbol{\kappa_l^r}$, $\boldsymbol{\kappa_l^b}$, and $\boldsymbol{\kappa_b^r}$.

for bridged interfaces with L equal 6, 20 and 60 u.c. in Fig. 3.6(a). Phonons above the cut-off frequency of the heavy material (right contact) ω_r^{cut}, corresponding to those with wavevector larger than $\boldsymbol{\kappa_l^r}$ in the left or $\boldsymbol{\kappa_b^r}$ in the bridge material (see Fig. 3.6(d)), accumulate in the left and bridge materials at 2 K (i.e., energy density in those modes is much higher than lower-wavevector modes). This indicates that phonons almost transport elastically at the average temperature of 2 K, and those phonons with frequencies higher than ω_r^{cut} cannot transmit. The energy density can also be plotted for the transverse modes and shows similar behaviour, albeit at a correspondingly lower cut-off frequency than the longitudinal modes.

We further analyze the difference in energy density distributio of bridged interfaces with L=60 u.c. (31.32 nm) and L=20 u.c. (10.44 nm). Figure 3.6(b) shows such difference before the left boundary (from z_l-5 nm to z_l, where z_l is the location of their respective left boundary), and Fig. 3.6(c) shows the difference after the right boundary (from z_r to z_r+5 nm, where z_r is the location of their respective right boundary). Just before the left boundary (Fig. 3.6(b)), $\mathbf{T}(L\text{=60 u.c.})\text{-}\mathbf{T}(L\text{=20 u.c.}) < 0$ K when $\boldsymbol{\kappa} > \boldsymbol{\kappa_l^r}$ or $\omega > \omega_r^{cut}$, and the inequality reverses when $\boldsymbol{\kappa} < \boldsymbol{\kappa_l^r}$ or $\omega < \omega_r^{cut}$. This implies that when the bridge layer thickness L increases, more energy above ω_r^{cut} scatters to frequencies below ω_r^{cut}. Just after the right boundary (Fig. 3.6(c)), the energy density is greater in the 60 u.c. system in all frequency regimes. This indicates that phonon transmission is greater to the right material, consistent with the observed higher conductance for the thicker intermediate layer (Fig. 3.1(b), G_{MD}, $\mathbf{T}$=2 K). We conclude that as the bridge layer thickness L increases, more high frequency phonons with low or no transmission scatter via weak anharmonic interactions to frequencies below ω_r^{cut} where transmission is higher, thereby bringing up the conductance in Fig. 3.1(b)(c).

That thermalization processes initially drive the increase in conductance with bridge layer thickness L can also be verified by comparing the slopes of G versus $\mathbf{T}$ for systems with different layer thicknesses (Fig. 3.7(a)). G generally increases linearly with $\mathbf{T}$ for an abrupt interface due to thermalization [103, 104]. Increasing $\mathbf{T}$ increases the anharmonic scattering rates that scatter high frequency phonons to low frequency regimes, and facilitates broadband transport [103,104]. Larger slopes indicate this kind of scattering-assisted transport enhancement is larger. Compared to the abrupt interface, the bridged interface conductance G increases with $\mathbf{T}$ with a larger slope, and this slope increases with L. Accordingly, we conclude that increasing the bridging layer thickness introduces more thermalization processes and thus increases the conductance.

As temperature $\mathbf{T}$ rises further and the bridge layer thickness L increases, the conductance of the bridged interfaces ultimately decreases (Fig. 3.7(b) and Fig. 3.1(c)) at 30 K. This happens when strong anharmonicity is present, and arises from Umklapp back scattering

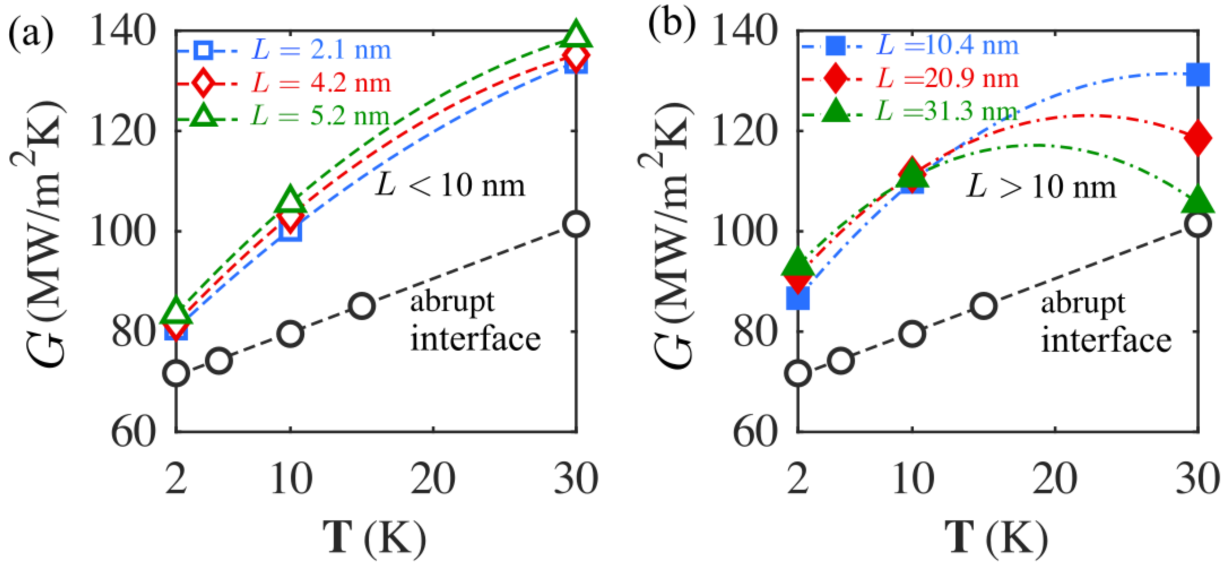

Figure 3.7: (a) At short length, conductance G increases with $\mathbf{T}$ with a larger slope than that of an abrupt interface. Meanwhile, the longer the bridge layer thickness, the larger the conductance and the slope. These increases are due to thermalization. (b) When the bridge layer thickness is large enough, increasing $\mathbf{T}$ tends to decrease the conductance due to Umklapp scattering.

processes, where phonons moving in the transport direction are scattered to phonons with opposite velocity. We thus conclude that weak anharmonicity can effectively increase phonon transport across moderately thick bridging interfaces by increasing thermalization, while strong anharmonicity can reduce phonon transport across thick interfaces by increasing resistive scattering.

Our results show that the bridge layer thickness L can be used as another parameter to tune the strength of anharmonicity in addition to temperature $\mathbf{T}$. The effects of these two parameters can be explained by the scattering processes similar to the Fermi's Golden Rule. Take the three-phonon decay scattering rate derived from Fermi's golden rule as an example:

$$\Gamma_j^- = \frac{1}{N}\sum_{j'j''}\frac{\hbar\pi}{4}\frac{N_0' + N_0'' + 1}{\omega_j\omega_{j'}\omega_{j''}}|V_{jj'j''}^-|^2\delta(\omega_j - \omega_{j'} - \omega_{j''}) \tag{3.5}$$

, where N_0' (similar for N_0'') is the Bose-Einstein occupancy for mode $\omega_{j'}$ (or mode $\omega_{j''}$) and $V_{jj'j''}^-$ is the three-phonon anharmonic scattering matrix element relating modes j, j'

and j''. [62, 105] Increasing the bridge layer thickness L increases the space for phonons to interact with each other, i.e, increases the scattering phase space $\sum_{j'j''} \delta(\omega_j - \omega_{j'} - \omega_{j''})$. Meanwhile, increasing the temperature $\mathbf{T}$ increases the displacement of atoms, which increases the occupation of phonons $N'_0 + N''_0 + 1$.

3.2.5 Length scale to separate resistance L_s versus mean free path λ_b

The Boundaries and the bridge layer of a bridged interface system contribute to the total thermal resistance ($R_{tot} = 1/G$) in two different ways. In the ballistic transport regime, phonons transport through the bridge layer without any backscattering, thus the major contribution to the resistance stems from the boundaries. On the other hand, if the system is in the diffusive regime, both boundaries and the bridge layer contribute to the total resistance, and their resistances can be summed together. In addition, the bridge layer resistance behaves as an intrinsic resistor following Fourier's law, while the boundary resistances should be independent of each other and of the bridge layer thickness L.

We quantified the boundary resistances ($R_{l,by}$,$R_{r,by}$ are resistances for the left and right boundary respectively) and the intrinsic resistance of the bridge layer (R_b) as the ratio of temperature drop over heat flux, such that:

$$\begin{aligned} R_{l/r,by} &= \Delta\mathbf{T}_{l/r}/q = [(\Delta\mathbf{T}_{l/r}/\Delta\mathbf{T}_i]R_{tot} \\ R_b &= \Delta\mathbf{T}_b/q = [\Delta\mathbf{T}_b/\Delta\mathbf{T}_i]R_{tot} \end{aligned} \tag{3.6}$$

, where $\Delta\mathbf{T}_l$ and $\Delta\mathbf{T}_r$ are the temperature drops at the left and right boundary respectively, $\Delta\mathbf{T}_b$ is the temperature drop within the bridge layer and $\Delta\mathbf{T}_i$ is the total temperature drop across the bridged interface (as illustrated in Fig. 3.2(b) in section 3.2.3).

The near zero value of R_b at 2 K indicates the majority of phonons transport ballistically through the bridge layer, and all scattering events leading to resistance happen at the

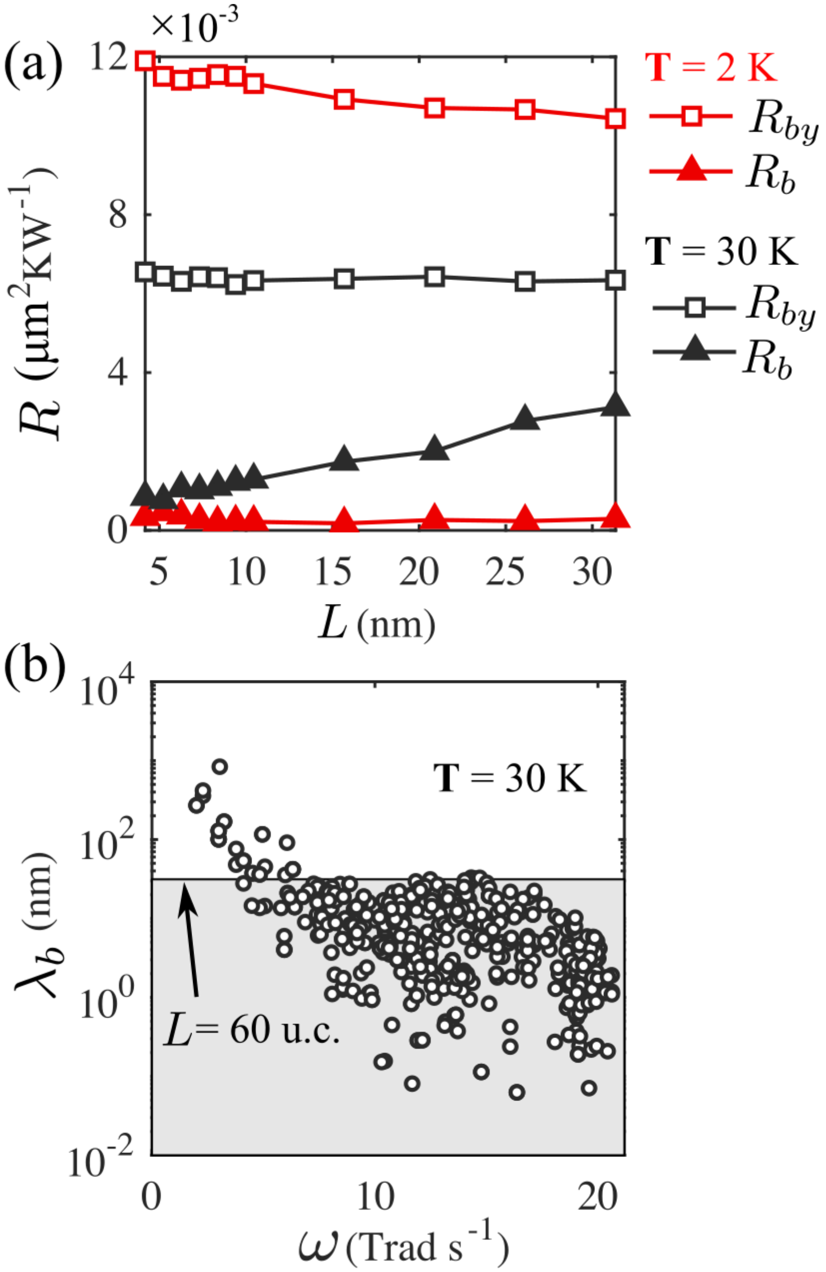

Figure 3.8: (a) The thermal boundary resistance R_{by} (open square) and the thermal resistance in the bridge layer R_b (solid up-triangle) at 2 K (red) and 30 K (black); Note the linear increase of R_b versus L and the constancy of boundary resistances indicating the Ohmic behavior at 30 K. (b)Bulk mean free path of the bridge layer λ_b from normal mode decomposition. A quite small percentage of the modes, which have frequencies below 5 Trad s^{-1} are expected to propagate ballistically while the rest follow a diffusive process.

boundaries (Fig. 3.8(a)). R_{by} (R_{by}=$R_{l,by}$+$R_{r,by}$) decreases with L, in agreement with the previous discussions on G versus L, suggesting that all benefits on the conduction by thermalization processes are at the boundaries. The ballistic feature of $R_b \sim 0$ μm^{2}KW^{-1} also suggests that the resistance cannot simply be treated as resistances in series at 2 K.

At 30 K, the trends of resistances versus L reverse, indicating that bridge interfaces with layer thickness larger than ∼5 nm are in a diffusive transport regime, and the resistances can be treated as resistances in series. This is supported by the following observations. First, R_{by} does not change with L, suggesting R_{by} is not influenced by the bridge layer thickness. Second, comparing the bulk mean free path of the bridge layer material λ_b at 30 K (Fig. 3.8(b)) with the bridge layer thickness L (λ_b is computed by the normal mode decomposition technique [106]), only a few phonons have bulk mean free paths longer than 60 u.c. (L=31.3 nm). This L independence of R_{by} indicates the L=60 u.c. system is almost in the diffusive limit, and R_{by} from ∼5 nm is the same as R_{by} in the diffusive limit (R_{by} at 60 u.c.). Last but not the least, the intrinsic resistance of the bridge layer R_b increases linearly with L, demonstrating a behavior following the Fourier's law. Note that R_{by} at 5 nm is the same value as R_{by} in the L=60 u.c. (31.3 nm) system. This indicates that the resistances can be treated as resistances in series from a very short length scale(∼5 nm). The majority of phonons have λ_b longer than 5 nm at 30 K. Therefore, the common criterion for diffusive transport $\lambda_b < L$ appears to be stricter than necessary. The reason could be that the bulk junction material MFP does not take the interface scattering, which can be quite large, into consideration.

3.3 Size effects on multilayer bridged interfaces

In the previous section, the size effect on a single layer bridged interface is studied. In this seciton, we extend the geometric idea [88, 103] to a multiple layer bridged interface – the exponential mass-graded interface. This idea is an analogy to the design for best refractive AR coatings. [107, 108] This design for a multilayer bridged interface is illustrated in Fig. 3.9. The atomic mass of each layer (m_n) is defined as the geometric mean relative to the masses of its neighboring layers, which would generate an exponential rule of the atomic masses relative to the left contact mass (m_l):

$$m_n = m_l e^{\zeta n}, \tag{3.7}$$

with $\zeta = \ln(m_r/m_l)/(N_l + 1)$.

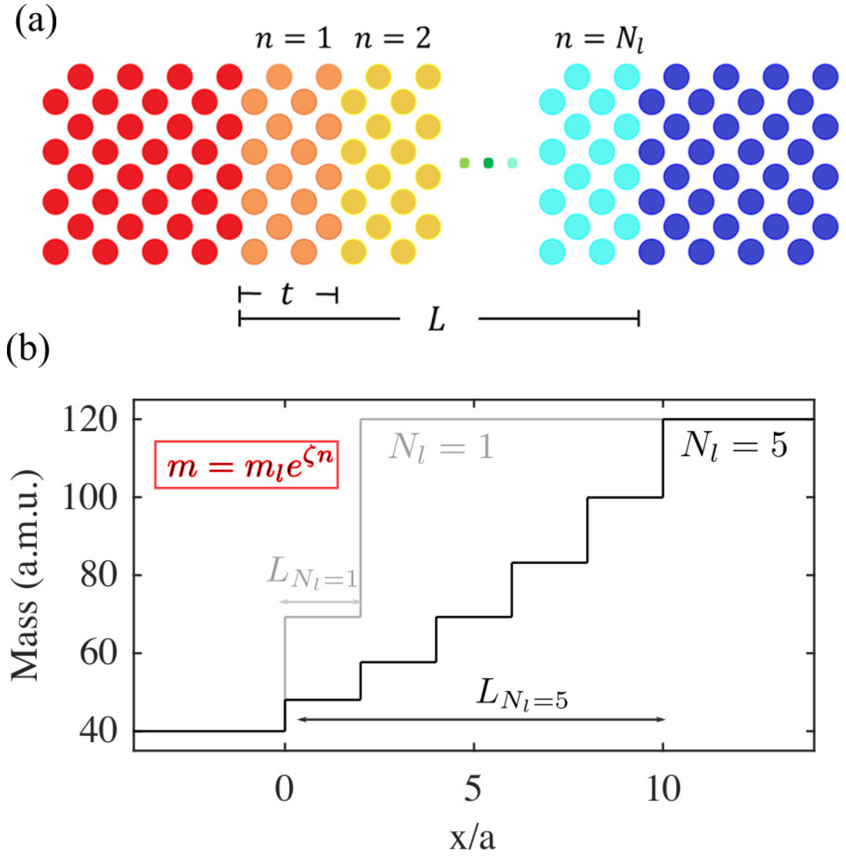

Figure 3.9: (a) Schematic of a mass-graded interface with N_l layers. In this case, each layer has a thickness of 2 unit cells ($t = 2$ u.c.) and the thickness of the junction is $L = t \times N_l$ u.c. (b) The spatial variation of masses for N_l=1 and N_l=5 (t=2 u.c.). m_l and m_r are 40 a.m.u. and 120 a.m.u. respectively and a is the lattice constant for 1 u.c. This figure is reproduced from ref. [59]

We compared this exponential mass-graded interface with the single interface system in the previous section, and we show that this choice of mass can lead to 2 times larger enhancement ($\sim$ 56% enhancement compared with abrupt interface 102.40±1.70 MW m^{-2} K^{-1}) than the single layer bridged interface ($\sim$ 23% enhancement) if the mass ratio $\frac{m_r}{m_l} = 3$. We also compared this exponential mass graded interface with the linear mass-graded interface, and showed the conductance can be maximally enhanced by 308% for the exponential mass-graded interface, compared to 289% given by the linear grading when the mass ratio is $\frac{m_r}{m_l} = 10$. All these comparisons and discussions are in ref. [59].

The focus of this section is to discuss size effects on a multilayer bridged interface from the harmonic limit to the anharmonic limit. The enhancement by this geometry and design is not within the scope of the size effects study, and can be found in ref. [59]. The simulations for the exponential mass-graded interface are the same as the ones for the single layer bridged interface. The only difference is that the multilayer setup and the choice of mass followed the exponential rule. The following content is reproduced in part with permission from [59] coauthored with Rouzbeh Rastgar, Carlos A. Polanco, Nam Q. Le, Avik W. Ghosh and Pamela M. Norris. Copyright [2019] Royal Society of Chemistry. Cite This: Nanoscale, 2019,11, 6254-6262. NEMD simulations were performed by Rouzbeh Rastgar from the Norris research group at UVa.

3.3.1 Harmonic limit

The analysis of our mass-graded interfaces in the harmonic limit is simplified using the system symmetry. Since all the material boundaries are perfectly abrupt, the potential energy is translationally invariant in the transverse direction, parallel to the boundaries. Thus, the force in that direction is zero and only phonons that conserve their transverse momentum or wavevector ($k_\perp$) can contribute to thermal transport. We define the number of combinations of phonons that conserve momentum along the system as the number of conserving channels M_c and count them using [88]

$$M_c(\omega) = \sum_{k_\perp} \min_{\alpha} M_\alpha(\omega, k_\perp), \tag{3.8}$$

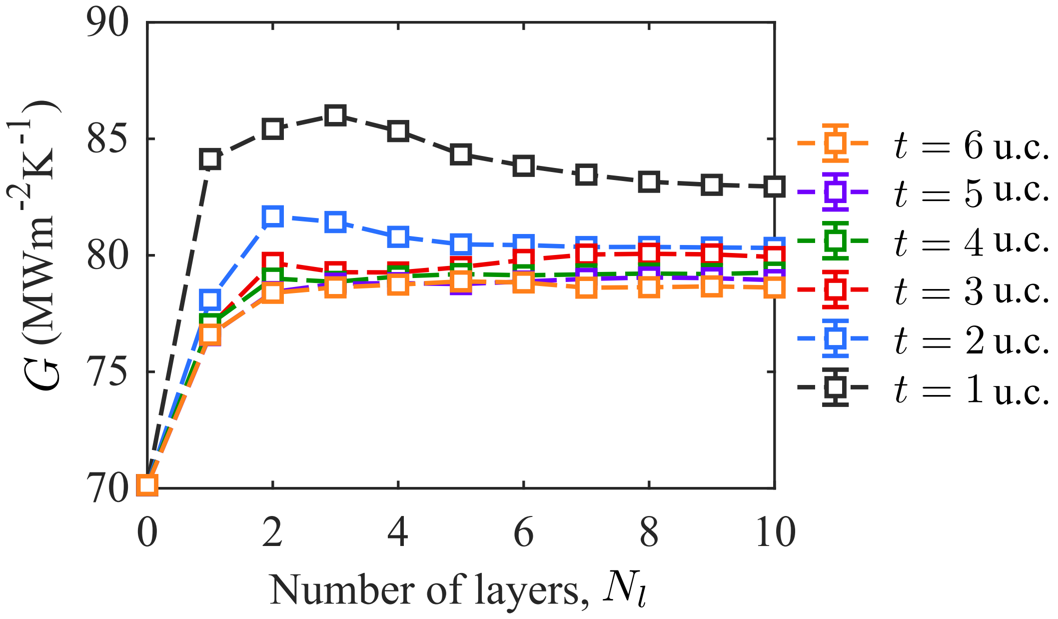

Figure 3.10: G_{hl} vs. N_l in the harmonic limit. G_{hl} quickly saturates as N_l increases. This figure is reproduced from ref. [59].

with α varying over the contacts and intermediate layers. M_α is the number of propagating modes in material α, which can be obtained by calculating MT from NEGF for each bulk material. In that case, the transmission for each mode is unity and thus $MT = M$. Since the conserving modes are the only ones that contribute to transport, we define an average transmission over those modes as $T_c(\omega) = MT(\omega)/M_c(\omega)$. Replacing MT in Eq. 3.1 by M_cT_c allows us to separate G_{hl} into a phase space of available transport channels, M_c, and its average phonon transmission, T_c.

Figure 3.10 shows the conductance across mass-graded interfaces in the harmonic limit. As the number of intermediate layers N_l increases, the harmonic conductance initially increases but saturates after $N_l > 5$. This trend is due to the interplay (see Eq. 3.1) between increasing transmission T_c (Fig. 3.11(a) and (d)) but decreasing number of transport channels M_c (Fig. 3.11(a) and (c)). The gain in T_c is due to the decrease in thermal impedance (acoustic impedance in linear dispersion regime) mismatch between adjacent layers [1, 109]. This gain happens mostly below 10 Trad/s (Fig. 3.11(d)) and is responsible for the increase of $MT(\omega)$

over the same frequency range (Fig. 3.11(b)) since M_c does not change much in that range. Note that the cut-off frequency for the lowest acoustic branch is 10.98 Trad/s, which seems to suggest that decreasing the mass mismatch helps phonon transmission for states with similar polarization (Fig. S1). The monotonic decrease of M_c follows from Eq. 3.8 as adding more intermediate layers can only decrease the minimum of modes at each $k_\perp$ and ω. The interplay between M_c and T_c yields a modest conductance enhancement in the saturated regions ($N_l > 5$ in Fig. 3.10), between 11% and 17%.

The saturation of G_{hl} follows from a combined saturation of M_c and T_c. $M_c(\omega, k_\perp)$ is obtained taking the minimum of modes (Eq. 3.8) over a set of materials with the same force constants and crystal structure, but with masses varying exponentially from one contact to another. Thus the dispersions and $M_\alpha(\omega, k_\perp)$ for those materials change gradually according to the mass. As N_l increases, the interval of this function is sampled more finely by the set of $M_\alpha(\omega, k_\perp)$, and thus M_c saturates to the lower bound. The transmission enhancement also saturates as it approaches its maximum value, unity (Fig. 3.11(d)).

The conductance of a mass-graded junction does not only depend on the number of layers, but also depends on the thickness of each layer t (Fig. 3.10). Thin layers yield larger conductance, but this enhancement disappears at about $t = 3$ u.c. We attribute the sharp increase in G_{hl} when the layer thickness is ultra-thin to phonon tunneling. For very thin layers (in our case, 2–3 conventional unit cells), phonons can tunnel even when the middle layers do not have propagating modes at a particular ω and momentum $k_\perp$ but the adjacent materials do. The transport of those extra phonons across the system enhances the overall conductance. This phenomenon was previously observed by English *et al.* [86] and Liang and Tsai [84] and they related it to the resulting sharp and narrow density of states associated with the thin film which can influence the elastic vs. inelastic thermal transport at the boundaries.

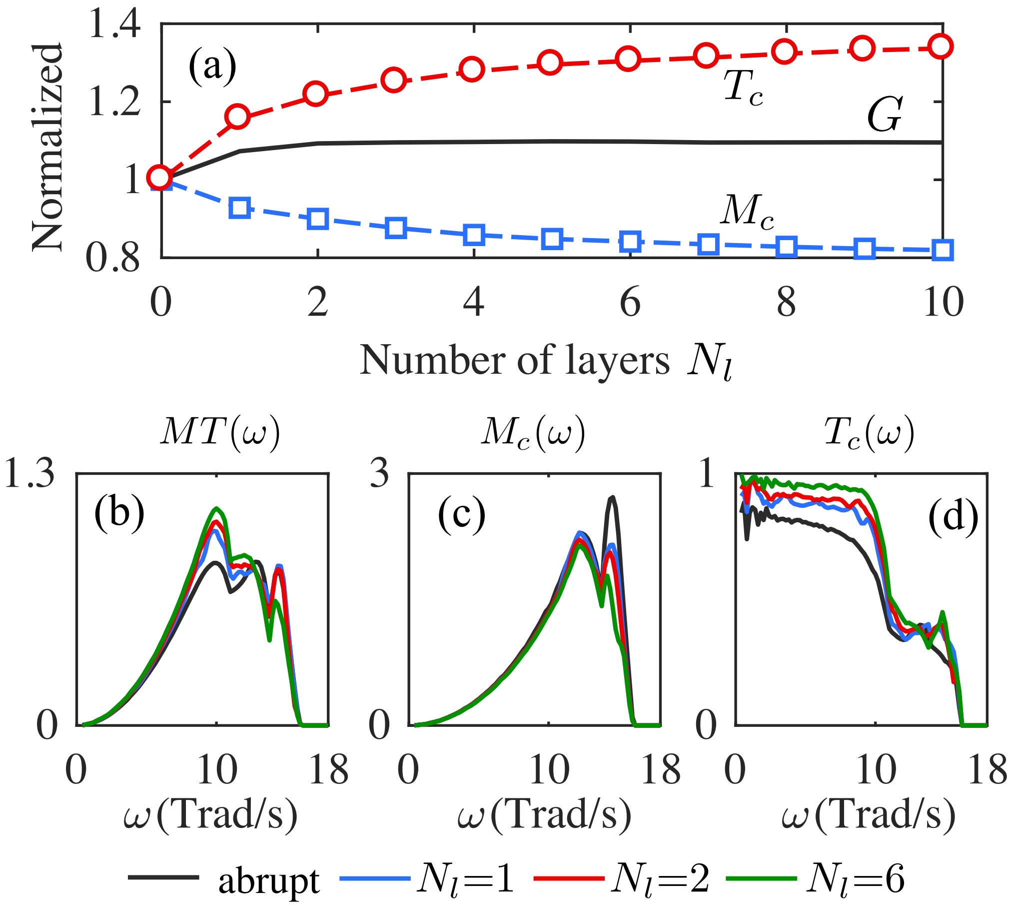

Figure 3.11: (a) Normalized values of G_{hl}, M_c, and T_c with respect to the abrupt interface vs. N_l. $M_c = \int_0^\infty M_c(\omega)d\omega$ and $T_c = \int_0^\infty T_c(\omega)d\omega$. T_c increases while M_c decreases with N_l, leading to the saturation of G_{hl}. NEGF results of (b) number of modes times transmission MT(ω), (c) number of available modes $M_c(\omega)$ and (d) average transmission $T_c(\omega) = \frac{MT(\omega)}{M_c(\omega)}$ when N_l is 0 (abrupt), 1, 2 and 6. All simulations are performed for $t = 6$ u.c. Enlarged versions of figures (b)-(d) can be found in the Supplemental Information for a better visualization. This figure is reproduced from ref. [59].

3.3.2 Weakly anharmonic limit

Surprisingly, at low temperature when anharmonicity is weak, the trend of G vs. N_l from our NEMD simulations (Fig. 3.12(a)) differs from that obtained in the harmonic limit by NEGF. We were expecting similar trends because at low temperature ($\mathbf{T} = 2$ K, which is about 1% of the melting temperature), atomic displacements in our NEMD simulation are small and thermal transport should be mostly harmonic. Nevertheless, this expectation seems to hold only for systems with $t = 1$ u.c. and $N_l < 10$, where we see a peak followed by a saturation (Fig. 3.10 and 3.12(a)). We have verified that the observed trends do not result from size effects on the simulation domains (see section A in Supporting information).

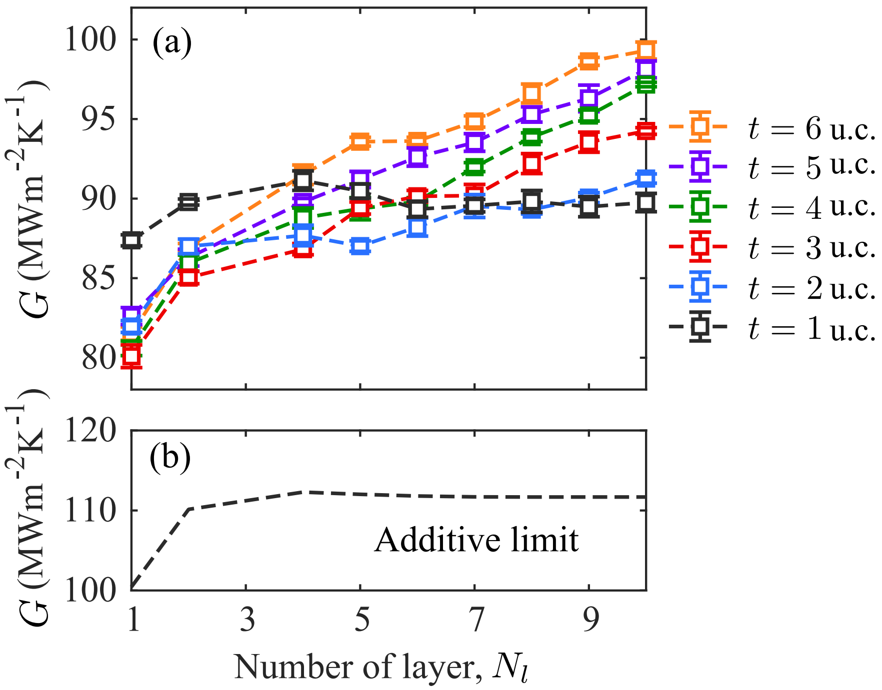

Figure 3.12: G vs. N_l in the presence of anharmonicity at $\mathbf{T} = 2$ K when the layer thicknesses vary from 1 u.c. to 6 u.c. (a) NEMD results. G increases almost linearly with N_l. Furthermore thicker layers yield larger G_{al}. b) additive limit (Eq. 3.9). G_{al} increases with N_l and quickly saturates. This figure is reproduced from ref. [59].

The increasing trend of G vs N_l in our ultra-low temperature NEMD simulations (Fig. 3.12) is not dictated by additive phonon transport either. In the additive limit, the conductance of the system, G_{al}, can be defined as the inverse of the sum of resistances:

$$1/G_{al} = \sum_{i=1}^{N_l} 1/G_{blk,i} + \sum_{j=1}^{N_l+1} 1/G_{int,j}, \tag{3.9}$$

where $1/G_{blk,i} = t/\kappa_i$ is the resistance intrinsic to the i^{th} intermediate layer, κ_i is the intrinsic thermal conductivity of material i and $1/G_{int,j}$ is the interfacial resistance for the j^{th} boundary. We neglect $1/G_{blk,i}$ in our analysis since it is significantly less than $1/G_{int,j}$ at $\mathbf{T} = 2$ K. For instance for a mass-graded interface with $t = 6$ u.c. and $N_l = 5$, the temperature drop at the interfaces is 93% of the total drop between the contacts (Fig. S2). Figure 3.12(b) shows the trend of G_{al} vs. N_l with each $G_{int,j}$ calculated on a single, independent boundary using NEGF and neglecting $1/G_{blk,i}$. G_{al} initially increases as neighboring layers become more similar and then saturates. The saturation is not seen in NEMD results and thus we conclude that the monotonic increase of conductance at very low temperatures results from neither purely harmonic nor additive transport.

The increasing trend in Fig. 3.12 hints at the important role played by phonon-phonon interaction in enhancing the conductance of mass-graded interfaces. Conductance seems to increase linearly with N_l and the slope increases with t. Larger N_l and t values result in a thicker total junction length, L, which allows more phonon-phonon scattering in this region. Given the conductance increases as phonon-phonon scattering increases, we hypothesize that scattering promotes thermalization that helps high frequency phonons with lower chance of transmission jump to modes with lower frequencies and higher transmission. This behavior is similar to the linear increase of interfacial thermal conductance with temperature, in which stronger anharmonicity contributes to better thermalization in the neighborhood of the interface [88,103].

The contributions to the enhancement of G from both anharmonicity and elastic phonon transmission are further analyzed in Fig. 3.13. Conductance increases with L with a similar slope when $t >1$, suggesting that anharmonicity constitutes the major contribution in the enhancement. This idea is further supported by comparing the enhancement from varying N_l while fixing L (i.e. varying phonon transmission at a fixed strength of anharmonicity) with the results from fixed N_l while varying L (varying the strength of anharmonicity with fixed phonon transmission). Figure 3.13 suggests that the contribution from the latter is larger than the former. To make this argument quantitative, we turn to the conductance values shown in the inset of Fig. 3.13. At a fixed $L = 30$ u.c., doubling N_l results in only 3% enhancement in G, whereas at a fixed N_l, increasing L from 30 to 60 u.c. results in more than 7% improvement in conductance. When fixing L, the enhancement would solely be

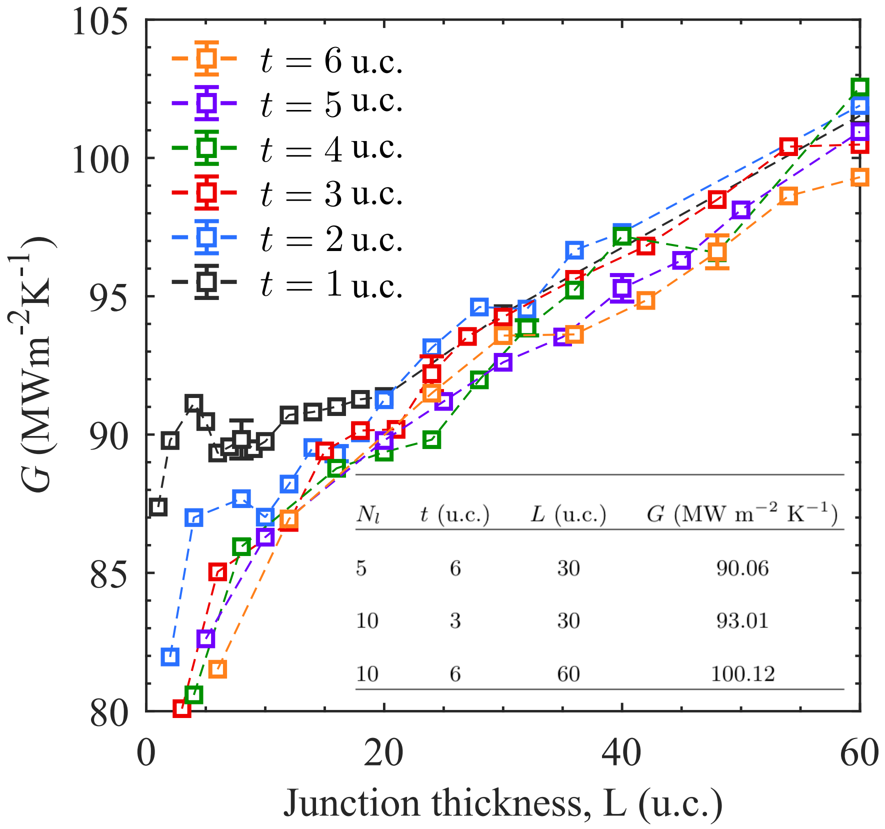

N_l	t (u.c.)	L (u.c.)	G (MW m^{-2} K^{-1})
5	6	30	90.06
10	3	30	93.01
10	6	60	100.12

Figure 3.13: Interfacial thermal conductance values from NEMD simulations at $\mathbf{T} = 2$ K for different junction thicknesses. Each color represents a different sub-layer thickness. Note that total thickness $L = N_l \times t$. Sample error bars are shown at L = 8, 16, 24, 32, 40, and 48 u.c. (inset) conductance values are shown for three cases of varying number of layers, layer's thickness and junction thickness based on an linear fitting in Fig. 3.14. This figure is reproduced from ref. [59] and provided by Rouzbeh Rastgar from Norris research group.

due to increases in phonon transmission at the boundaries; however, this enhancement is very small without the presence of anharmonicity. Bridging layers not only introduce better matching at each boundary, but also provide phonons with opportunity for thermalization, providing thereby a larger contribution to the overall enhancement.

The values of G in the weak anharmonic limit (Fig. 3.12(a) and 3.13) are bounded by those in the harmonic limit (lower bound) (Fig. 3.10) and those in the additive limit (upper bound) (Fig. 3.12(b)). Also, as N_l or L increases, G seems to transition from the harmonic to the additive limit. To quantify the ratio of harmonic vs. additive phonon transport across the junction, we define a quantity β such that $G = \beta G_{hl} + (1 - \beta) G_{al}$, where the harmonic

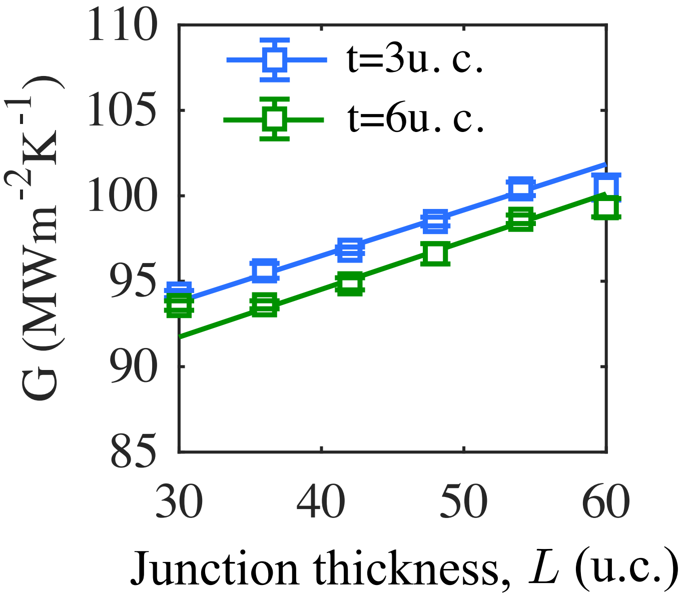

Figure 3.14: Interfacial thermal conductance values from NEMD simulations at $\mathbf{T} = 2$ K versus junction thickness. The square markers represent data from NEMD simulations while the solid lines represent linear fittings to the data. This figure is reproduced from ref. [59].

conductance G_{hl} is obtained from NEGF (Eq. 3.1) calculations across multiple layers in the same way Fig. 3.10 was obtained, while the additive limit conductance G_{al} is obtained from Eq. 3.9 by adding NEGF calculations at single boundaries exactly like Fig. 3.12(b) was obtained. Figure 3.15 shows that as N_l increases, G approaches the additive limit and thus β decreases, meaning less phonons can transport across all the interfaces without being scattered by other phonons. This is consistent with our conjecture that the bridging layers facilitate more phonons participating in the thermalization process.

3.4 Conclusion

First, we studied the size effect of bridging layer thickness on the thermal conductance of a single layer bridged interface. Our results demonstrate the existence of a minimum and also eventually a maximum conductance by varying either temperature or layer thickness. These phenomena are due to the dual roles of anharmoncity in that it can either enhance

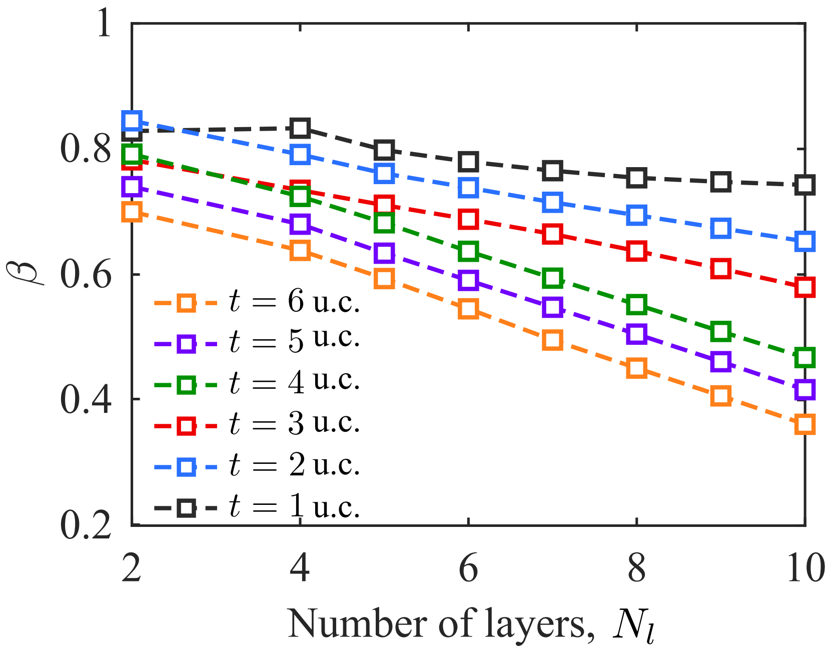

Figure 3.15: Contribution to G from harmonic vs. additive phonon transport across various mass graded junctions ($G = \beta G_{hl} + (1-\beta)G_{al}$). $\beta = 1$ represents purely harmonic transport while $\beta = 0$ purely additive transport.This figure is reproduced from ref. [59].

or hinder phonon transport. The minimum thermal conductance is a result of "phonon tunneling" plus thermalization effects in presence of weak anharmonicity. The maximum thermal conductance is due to additional Umklapp scattering with strong anharmonicty. Furthermore, we demonstrated that additivity of thermal resistances can occur at a much shorter layer thickness than the bulk mean free path of the intermediate layer. This indicates the comparison between bulk mean free path and intermediate layer thickness is too strict a rule and irrelevant to determine transport regimes for thin films bridging two materials. Instead, it is set by an equivalent interface scattering MFP when the interfacial scattering dominates.

We further studied size effects in multilayer exponential mass-graded interfaces from the harmonic o the anharmonic limit, and we showed that all the physics found in single layer bridged interface can be applied to the multilayer bridged interface. In the harmonic limit, the bridge lowers the conductance due to few conserving modes, while in the anharmonic limit, the anharmonicity enhances the thermal conductance due to added inelastic Umklapp scattering channels.

Chapter 4

Artificial heterostructures: superlattices for a microscopic understanding of coherence

4.1 Introduction

“Anomalous heat conduction” [110,111], referring to the breakdown of the classic Fourier’s law, is when thermal conductivity κ increases almost linearly with material dimension L. This so called “anomalous conduction” is no longer anomalous since it is the well-known conductance behavior in the ballistic transport regime. In mesoscopic devices, the “ballistic regime” refers to a regime where there is little to no resistivity to phonon transport when across materials or nanostructures. A characteristic length, the mean free path (MFP), is introduced to distinguish between ballistic transport regime and diffusive transport regimes [112]. MFP is defined as *the average length that a carrier (in this case, phonon) can travel freely before its momentum is changed by scatterings.* [113] In thermal conduction, momentum scattering centers that lead to finite MFP include nonlinear atomic interactions, defects, impurities, interfacial mismatch and roughness. In bulk materials, these scattering effects are taken into consideration by calculating the scattering rates and phonon lifetimes [114], while in heterostructures, the MFP can be extracted by plotting the spatial variation of spectral heat current versus the system dimensions by either Non-Equilibrium Green's Fuction (NEGF) or by Non-Equilibrium Molecular Dynamics (NEMD) . [115, 116] These theoretical advancements along with new achievements in nanotechnology [7, 117] open up a window towards tailoring thermal conductivity, by material dimensions, when the mean free path exceeds that dimension. [4, 6, 118, 119]

Another characteristic length that can be used to tailor thermal conductivity with device dimensions is the coherence length (l_c). Coherence length is of great interest due to its important role in utilizing the wave nature of phonons. [26,120] A notable example can be found in phononic crystal. [23, 25, 26] Bandgaps in the acoustic phonon frequency range, engineered by tweaking the periodicity of phononic crystals, can significantly reduce thermal conductivity at room temperatures. Some of the low frequency phonons, which are the dominant carriers at room temperature, no longer exists inside the bandgaps. Another topic that has attracted attention is the size effect governing coherent phonons in superlattices. [121–123] Superlattice is a hetero-structure with two length scales and a large volume density of interface scattering centers. The period thickness and total sample thickness can be systematically varied in nanofabrication to study their impact on transport mechanisms of heat carriers. One particular phenomenon observed when varying the length scale of superlattices is a minimal thermal conductivity κ_{SL} (corresponding to a length scale denoted as d_{SL0}) of the superlattice structure. [24, 124] Below d_{SL0}, an increasing d_{SL} leads to a decreasing κ_{SL} due to the formation of band structures of SLs; above d_{SL0}, an increasing d_{SL} leads to an increasing κ_{SL} due to the reduced number of interface resistances. [124, 125] The former is referred to coherent phonon transport regime while latter is often described as the size effect of transport in the diffusive regime, regardless of the fact that the sum over interfacial resistance rule requires adding momentum-scattering to the system.

Despite a large amount of simulations in literature reporting the engineering of thermal conductivity in periodic structures (phononic crystals, superlattices) by coherent or incoherent phonons, fundamental key concepts, definitions and methods are rarely discussed. We want to follow the definition of coherence in quantum mechanisms, where coherence is a term that determines whether phonons can behave like waves and interfere with each other. *The coherence regime, can be measured spatially by the coherence length – the propogation distance that a carrier (in this case, a phonon) can travel while still preserving its phases* [126–128]. In thermal conduction, scattering centers that destroy phases are phonon interactions, random interfacial mixings/roughness, random distributed defects/impurities, random spacings and any other event leading to stochasticity. So far, the only method being used to study the coherence length and spatial coherence is NEMD [129, 130], in which the coherence length is obtained from the spatial extension of phonon wave packets. We thus need new ways to quantify phonon coherence.

Additionally, the phase scattering is often intertwined with momentum scattering. For instance, at a finite temperature, anharmonicity, introduces both kinds of scattering. As a result, it is hard to distinguish the major scattering contribution or to identify the transport regime. To conclude that a certain transport behavior is present in a specific regime, it is ideal if we can separate the scatterings even phenomenologically. For instance, a proper classification of thermal transport regime in superlattices and size effects is missing due to lack of that capability.

In this section, we propose a method built on NEGF to illustrate the scattering mechanisms and transport regimes. Along with four different scenarios for scattering processes (no scattering; phase scattering only; momentum scattering only; momentum and phase scattering), we propose models where we can adjust the degrees of phase and momentum scattering separately are proposed. We apply the method to superlattices to study their size effects of thermal conductivity.

4.2 Classifying scattering based on the correlation function G^n.

4.2.1 A description of Non-equilibrium Green's function for heat transfer

We distinguish different scattering processes and transport regimes using the Non-Equilibrium Green's Function (NEGF) formalism. NEGF is generally used to treat carrier transport properties under open boundary conditions, where the system can be partitioned into a transport region (device) and left/right contacts (Fig. 4.1). For heat flow, NEGF solves the equation of motion under open boundary conditions [60, 61]:

$$[\omega^2 \mathbf{M_d} - \mathbf{K_d}]u - \Sigma u = S \tag{4.1}$$

where S is the source of injecting phonon waves, and $\mathbf{M_d}$ and $\mathbf{K_d}$ are the mass matrix and force constant matrix for the device respectively. Σ is the self-energy contribution from all contacts (l and r) and scattering centers (s): $\Sigma = \Sigma_l + \Sigma_r + \Sigma_s$.

The solution to the equation of motion is $u = GS$, where $G = [\omega^2 \mathbf{M_d} - \mathbf{K_d} - \Sigma]^{-1}$ is the retarded Green's function. The self-energies from the contacts are expressed as: $\Sigma_c = \mathbf{K_{dc}} g_c \mathbf{K_{dc}}'$, where c stands for left(l) or right(r) contact, $\mathbf{K_{dc}}$ is the coupling force constant matrix between the device or channel (d) and the contact (c). The surface Green's function g_c can be achieved by using a recursive algorithm for the contact c [113, 131].

To obtain the steady state current and conductance for a non-equilibrium system including dephasing/inelastic/momentum scattering mechanisms (introduced by scattering matrix Σ_s), the following sets of equations should be solved self-consistently (Σ_s and $\Sigma_s^{in,out}$ usually depend on G and $G^{n,p}$):

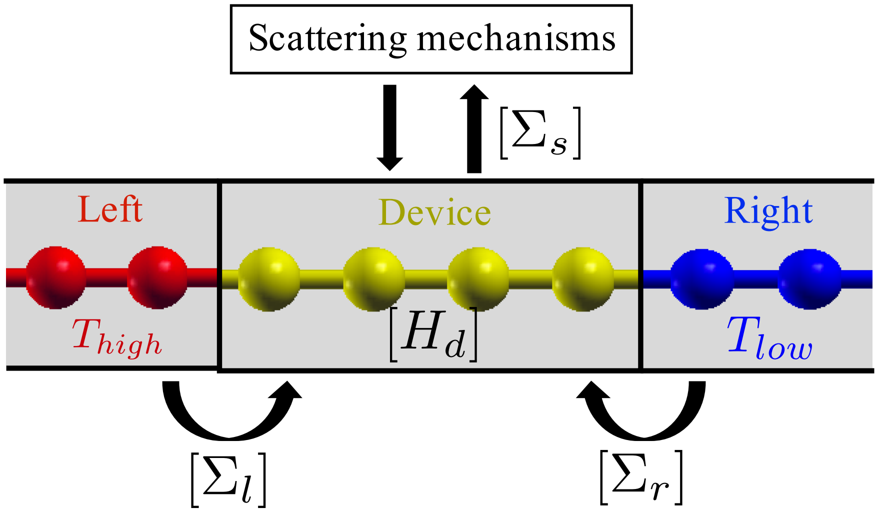

Figure 4.1: A schematic illustration for simulating 1 dimensional heat flow in NEGF including various scattering mechanisms. The left and right contacts are in local equilibrium at $\mathbf{T}_{high}$ and $\mathbf{T}_{low}$.

$$
\begin{aligned}
G &= [\omega^2\mathbf{M_d} - \mathbf{K_d} - \Sigma_l - \Sigma_r - \Sigma_s]^{-1} && \text{(Retared Green's function)} \\
A &= i[G(\omega) - G^\dagger(\omega)] && \text{(Spectral function)} \\
G^n &= G(\Sigma_l^{in} + \Sigma_r^{in} + \Sigma_s^{in})G^\dagger && \text{(Correlation or lesser Green's function)} \\
G^p &= G(\Sigma_l^{out} + \Sigma_r^{out} + \Sigma_s^{out})G^\dagger && \text{(Greater Green's function)} \\
\Sigma_c^{in}(\omega) &= N_c(\omega)\Gamma_c(\omega) && \text{(In-scattering function)} \\
\Sigma_c^{out}(\omega) &= [N_c(\omega)+1]\Gamma_c(\omega) && \text{(Out-scattering function)} \\
\Gamma_c(\omega) &= i[\Sigma_c(\omega) - \Sigma_c(\omega)^\dagger], c = l \text{ or } r && \text{(Broadening matrix)}
\end{aligned}
\tag{4.2}
$$

where $N_c(\omega)$ is the Bose-Einstein distribution for contacts; Γ_c is the broadening matrix describing the interaction between the channel (or device) and the contacts; A is the spectral function of which diagonal terms are the local density of states, G^n $(-iG^<)$ and G^p $(-iG^>)$ are the lesser and greater Green's functions respectively. In addition, G^n is the phonon correlation function of which the diagonal terms represent the phonon density.

The average steady state current can be obtained by calculating the current inflow from the hot contact to the channel I_l (assuming left contact is the hot bath as shown in Fig. 4.1) or the outflow current from the channel to the cold contact I_r:

$$I_c = \int_0^\infty \frac{\hbar\omega}{2\pi}\text{Trace}[\Sigma_c^{in} A - G^n \Gamma_c] d\omega, \quad c = l \text{ or } r \tag{4.3}$$

We can define an average transmission $M(\omega)\bar{T}(\omega)$:

$$M(\omega)\bar{T}(\omega) = \text{Trace}[\Sigma_l^{in} A - G^n \Gamma_l]/[N_l(\omega) - N_r(\omega)] \tag{4.4}$$

so that current can be written as:

$$I_c = \int_0^\infty \frac{\hbar\omega}{2\pi} M(\omega)\bar{T}(\omega)[N_l(\omega) - N_r(\omega)] d\omega, \quad c = l \text{ or } r \tag{4.5}$$

Note that this is usually the format of current when the system is coherent and Σ_s and $\Sigma_s^{in,out}$ are zero. Under such condition, the transmission can be solved by a well-known Fisher-Le equation $\bar{T}(\omega) = \text{Trace}[\Gamma_l G \Gamma_r G^\dagger]$.

4.2.2 Introducing dephasing scattering

In NEGF, the scattering mechanisms, including energy exchange, momentum scattering and wave dephasing, are introduced by adding a scattering self-energy Σ_s to the channel (device) Hamiltonian (as sketched in Fig. 4.1). Importantly, this self-energy Σ_s can be added to introduce specific kinds of scattering process phenomenologically, an ideal tool to study the impact on transport from one particular kind of scattering. This method has been developed in electronic quantum transport, [56, 132] however, but has not been applied to study heat flow to our knowledge. In the following, we demonstrate simulating heat flow under various scattering mechanisms.

By changing the scattering self-energies, we can add in ‘phase scattering only’ and ‘phase and momentum scattering’ into the device:

$$\begin{aligned}\Sigma_s(i,j) &= D(i,j)G(i,j) \\ \Sigma_s^{in,out}(i,j) &= D(i,j)G^{n,p}(i,j)\end{aligned} \tag{4.6}$$

These two types of scattering processes can be defined in the matrix $D(i,j)$ [132]:

$$\begin{aligned}&D(i,j) = d_m\delta_{i,j} \text{ (Both momentum and phase scattering)} \\ &D(i,j) = d_p \text{ for all } i,j \text{ (Dephasing only scattering)}\end{aligned} \tag{4.7}$$

where d_m and d_p are parameters representing the strength of scatterings. The reason why such format of $D(i,j)$ can introduce *dephasing only (momentum conserved)* or *both momentum and dephasing* scattering mechanisms is that $D(i,j)$ represents the correlation between scattering potentials at point i and point j: $D(i,j) \propto \langle U(i)U^*(j)\rangle$, where $\langle ...\rangle$ is the ensemble average. [56, 132, 133] Because $D(i,j)$ is the correlation between potentials, it is only a function of the relative distance $i-j$. From the Fourier transform of the correlation of the perturbation potentials at wavevector q, the loss of the momentum $\hbar q$ can be obtained [134]. In the *dephasing only* method, $D(i,j)$ is independent of $i-j$, so that its Fourier transform leads to delta functions of q: $F[D(i,j)=d_p]=\sqrt{2\pi}\delta q$, implying that the wavevector q is not changed or scattered to other wavevectors. In the *momentum and dephasing scattering* method, $D(i,j)$ is non-zero when $i=j$, thus the Fourier transform of it is independent of q: $F[D(i,j)=d_m\delta_{i,j}]=d_m/\sqrt{2\pi}$, meaning the momentum q is scattered equally to other wavevectors.

4.2.3 Illustration of momentum scattering and dephasing scattering in NEGF

In the previous section, we talked about introducing momentum scattering (resistance) and dephasing scattering (decoherence) by varying the content of the correlation of deformational potential $D(i,j)$. In this section, we show how the scattering events can be visualized.

In phonon transport, G^n is the correlation function of atomic displacement: [60,61]

$$G^n(x,x',t,t') = \frac{1}{\hbar}\langle u(x,t)u(x',t')\rangle \tag{4.8}$$

, where $u(x,t)$ and $u(x',t')$ are the collective motion of phonons at time t or t', position x or x' respectively. Converting to average and relative coordinates $(x,x',t,t') \rightarrow (x+x', x-x', t+t', t-t')$, we can write the slowest decay term as:

$$G^n \propto AA'e^{-|x-x'|/l_c}e^{-|x+x'|/\lambda}e^{-|t-t'|/\tau_c}e^{-|t+t'|/\tau_E}. \tag{4.9}$$

We can see that $G^n(x,x',t,t')$ plotted along each coordinate represents a different kind of scattering process. The momentum scattering reduces the wave transmission and amplitude, and causes a decay along the $|x+x'|$ axis, while dephasing scattering destroys the spatial correlations and influences $G^n(x,x',t,t')$ along the $|x-x'|$ axis. In an analogy to the spatial case, in the temporal situation, energy relaxation can be visualized along $|t+t'|$ axis, while temporal incoherence can be seen along $|t-t'|$ axis.

In this work, we explicitly consider the spatial situation. Assuming time translational invariance, we Fourier transform the time difference $|t-t'|$ to convert $G^n(x,x',t,t')$ to $G^n(x,x',\omega)$ to illustrate its frequency dependent spatial correlation decay. In addition, to achieve a better interpretation, the first order correlation function G^n is normalized as $g^n(x,x') = \frac{G^n(x,x')}{G^n(x,x)^{1/2}G^n(x',x')^{1/2}}$. In our study, we choose the $x=0$ axis to visualize the phonon displacement correlations, and consequently a $g^n(x=0,x')$ is used. The carrier density is also normalized to compare with the highest density to visualize the decrease in transmission probability. In the study of phonon transport, the diagonal term of $G^n(x,x)$ is normalized by the density in the hot contact. We assume the hot contact is located at the beginning of the device, thus $g^n(x,x) = \frac{G^n(x,x)}{G^n(x=0,x=0)^{1/2}G^n(x,x)^{1/2}}$ is used to interpret the momentum scattering.

Four different scenarios of scattering processes are tested to verify our approach: no scattering (case 1), dephasing only scattering (momentum conserving) (case 2), momentum only scattering (case 3) and both momentum and phase scatterings (case 4). A one-dimensional chain with a mass of 20 amu and a spring constant of 100 N/m is used in the simulation. For case 2 and case 4, the scattering mechanisms are added by Σ_s and $\Sigma_s^{in,out}$ as described above. $d_{m/p} = 10^3$ amu (Trad/s)^2 are chosen for the simulations. For 'momentum only' scattering, a point defect with a mass of 40 amu is set in the middle of the chain. In all the cases, the average temperature is 300 K, and the temperature difference between the two ends of the chain is 10 K.

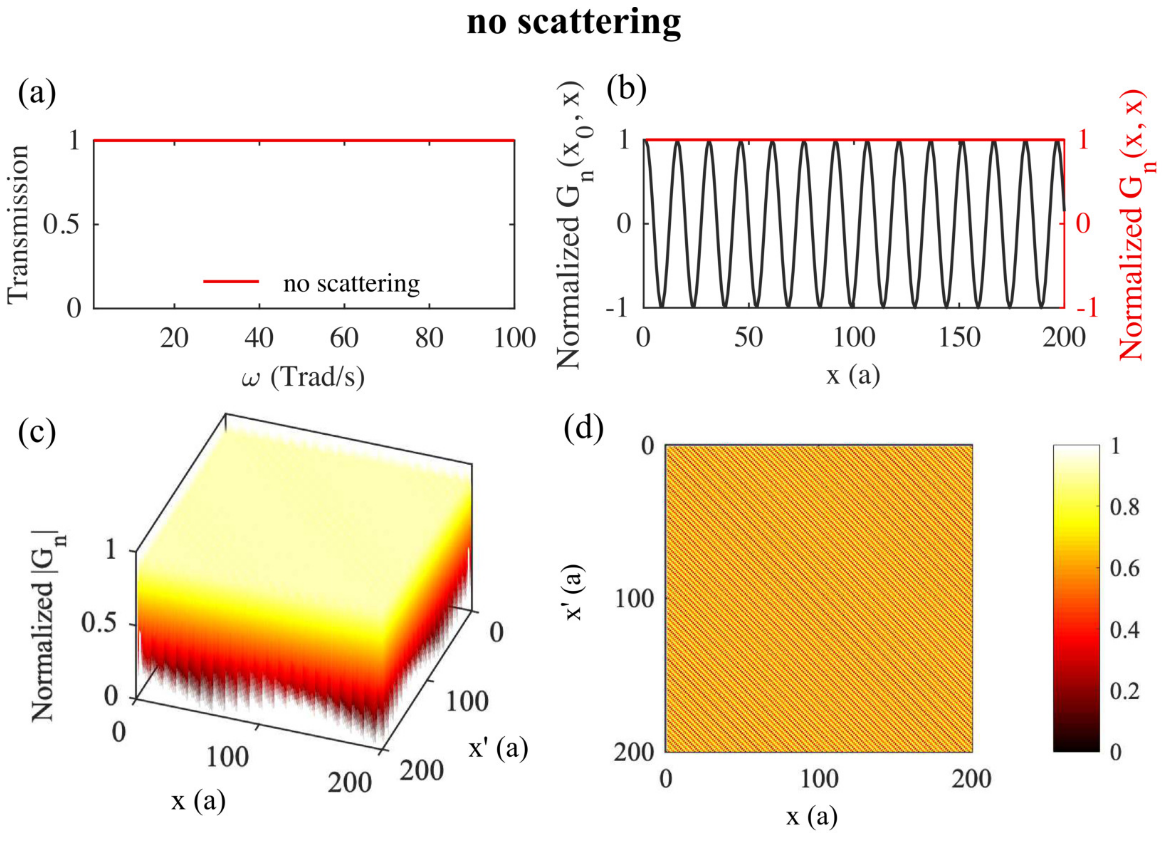

Figure 4.2: At frequency ω=28.95 Trad/s, without any scattering, (a) Transmission; (b) scaled $G_n(x_0, x)$ and scaled $G_n(x, x)$; (c) Scaled $G_n(x, x')$ (d) Scaled $G_n(x, x')$ in 2D view.

When there are 'no scattering' events in the chain, the transmission is unity, as shown in Fig. 4.2(a). As we mentioned before, the diagonal term of $G^n(x, x', \omega)$ (or $g^n(x, x)$), captures momentum scattering while off-diagonal term ($g^n(x_0, x')$, where x_0 is $x = 0$) capture dephasing. Accordingly, without scattering, $g^n(x_0, x')$ oscillates with a certain phase and the amplitude is unity. The diagonal term $g^n(x, x)$ is also unity (Fig. 4.2(b)), which is consistent with transport with no scatterings. The scaled $|G^n(x,x')|$ is shown in Fig. 4.2(c) and (d), demonstrating no decay along any directions.

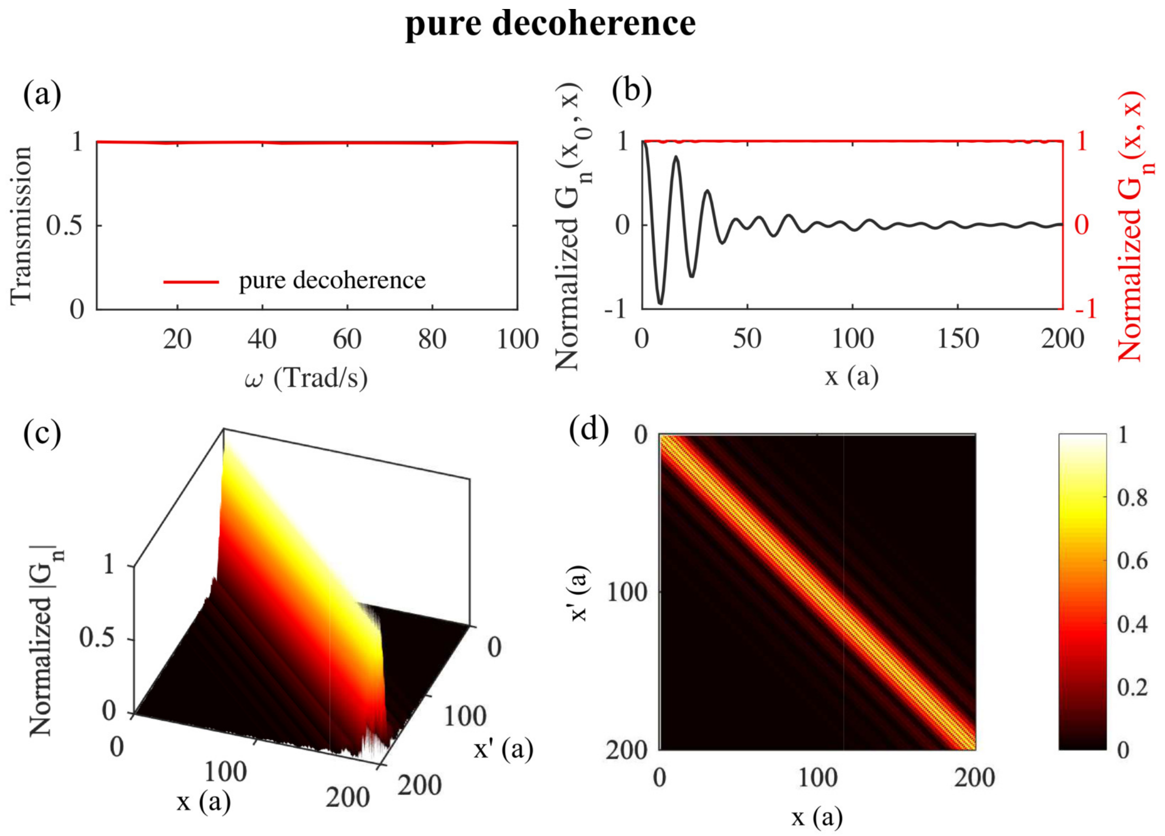

Figure 4.3: At frequency ω=28.95 Trad/s, including only phase scattering, (a) Transmission; (b) scaled $G_n(x_0, x)$ and scaled $G_n(x, x)$; (c) Scaled $G_n(x, x')$ (d) Scaled $G_n(x, x')$ in 2D view.

When 'dephasing scattering' is added to the one-dimensional chain and no momentum scattering events are included, the transmission probability is still unity (Fig. 4.3(a)). Meanwhile, the amplitude of the diagonal term G^n is also unity as shown in Fig. 4.3(b) and (c). The invariance of $G^n(x, x', \omega)$ along the $x = x'$ axis, signifies no carrier density change (or potential change) in the system, and thus no momentum scattering happens in the system. This is expected since dephasing scattering only introduces scattering to phases and destroys any interference and coherence phenomena. In contrast to momentum and transmission conservation, the off-diagonal term of $G^n(x, x', \omega)$ $(g^n(x = 0, x'))$ quickly decays to 0 with a decay length less than 50 Å (Fig. 4.3(b)). $G^n(x, x', \omega)$ along the $x = -x'$ axis acts as a Gaussian function with the bandwidth denoting the coherence length. Pure decoherence can happen in electrons, spins and excitons when coupling to an external thermal bath [135–138]. A possible analogy for phonons can be the low energy long wavelength acoustic phonons that are rapidly thermalized with an external bath. However, further studies are needed to support such statement.

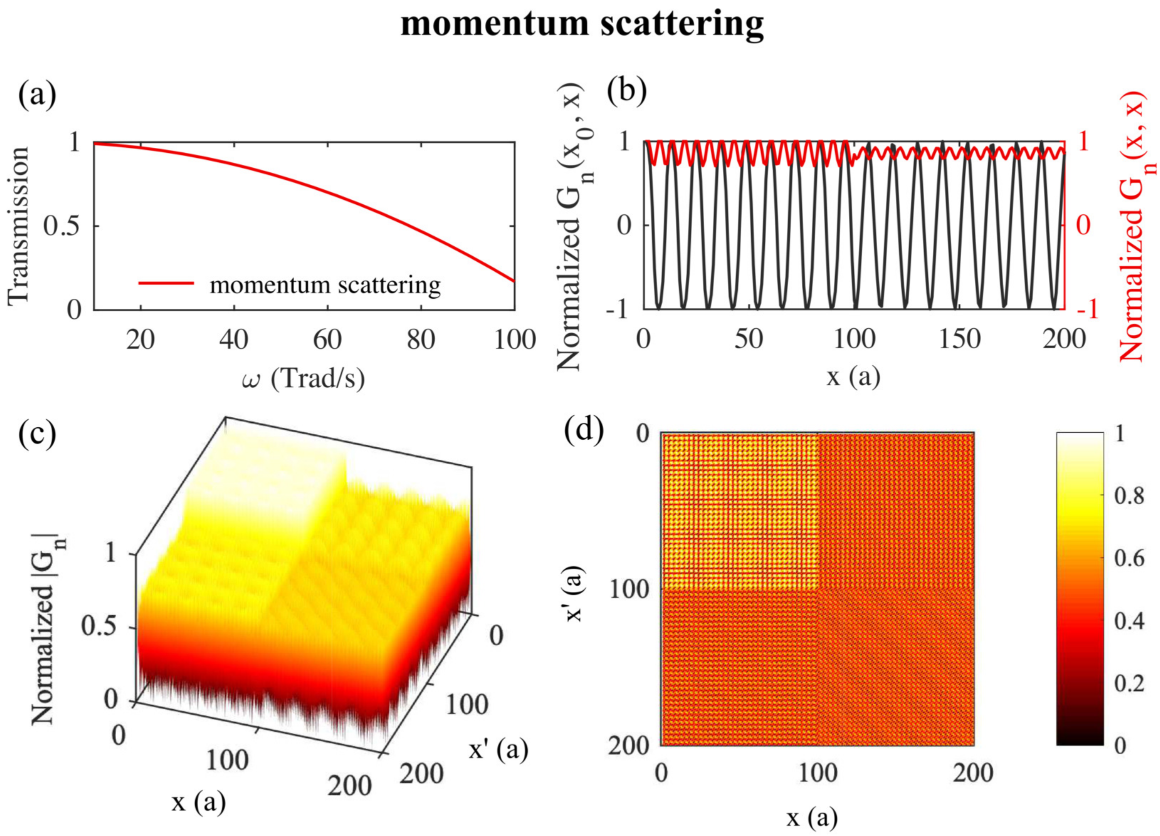

Figure 4.4: At frequency ω=28.95 Trad/s, including only momentum scattering (point defect), (a) Transmission; (b) scaled $G_n(x_0, x)$ and scaled $G_n(x, x)$; (c) Scaled $G_n(x, x')$ (d) Scaled $G_n(x, x')$ in a 2D view.

Any momentum scattering causes the transmission to be less than unity; Fig. 4.4(a) shows one example with scattering by a point defect. In this case, no phase scattering events exist in the system, i.e. it is a system with only elastic ‘momentum scattering’. The normalized correlation function $g^n(x = 0, x')$ is the same as the one with no scattering, while $g^n(x, x)$ shows a small decrease in the amplitude when the point defect is present, consistent with a decrease of transmission. Note that if the correlation function is not normalized, $G^n(x, x', \omega)$ will also show a decay along $x = 0$ axis. This is because the correlation function of phonon modes transports as a wave packet. The decay of phase influences the length of the wave packet, while the amplitude of phonon waves affects the wave packet amplitude. However, if there is no phase scattering in the system, the amplitude of G^n would not decay to zero.

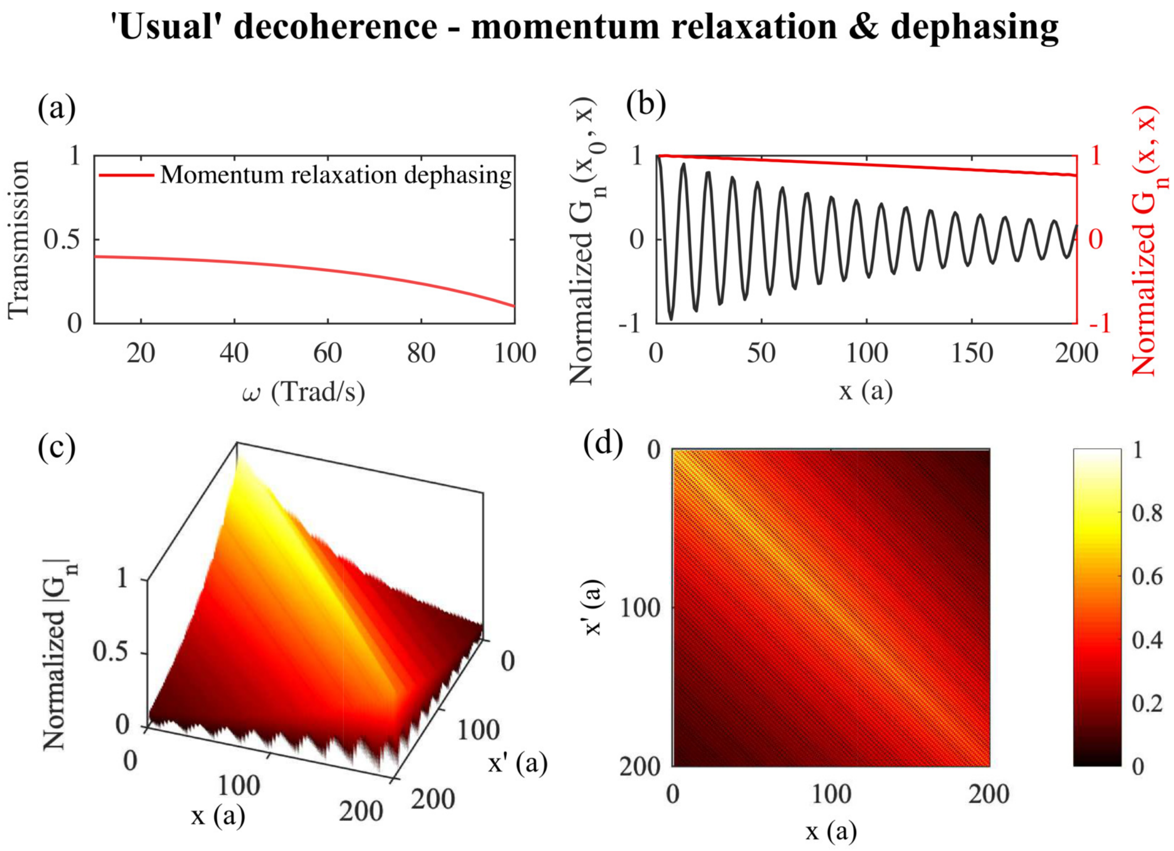
'Usual' decoherence - momentum relaxation & dephasing

Figure 4.5: At frequency ω=28.95 Trad/s, with including both momentum and phase scattering, (a) Transmission; (b) scaled $G_n(x_0, x)$ and scaled $G_n(x, x)$; (c) Scaled $G_n(x, x')$ (d) Scaled $G_n(x, x')$ in 2D view.

When 'momentum and phase scattering' are both included by $D(x, x')$ and Σ_s, clear decays along both diagonal($x = x'$) and off-diagonal ($x = -x'$) axes are observed (Fig. 4.5(b) (c) and (d)). The transmission is less than unity (Fig. 4.5(a)), and the amplitude of $G^n(x, x', \omega)$ also decreases spatially, as shown in Fig. 4.5(c). Similar to the discussions in the above situation, the wave packet of phonon correlations is influenced and limited by the wave amplitude and transmssion, thus the decay of the $G^n(x = 0, x')$ term is stronger than the decay of the $G^n(x, x)$ term, as shown in Fig. 4.5(b).

4.3 Influence of size effects on thermal transport in superlattices

There is rapid growth in the study of size effects on the thermal conduction in superlattices due to its fundemental importance to the overall physics of phonon transport. However a study that separates scattering mechanisms and transport regimes is missing. Phonon interactions can involve both momentum and phase scattering, so when considering a coherence length l_c, it is important to separate the incoherent regime from the diffusive regime. In this section, we separate these mechanisms, and explore the influence of dephasing and momentum relaxation on phonon conduction in superlattices.

The above discussed scattering mechanisms 'dephasing only' and 'momentum and dephasing scattering' are both applied to our studied superlattices. The system in study is an one-dimensional chain with 20/100 a.m.u. mass ratio and spring constant strength of 100 N/m. The semi-infinite left and right contacts are of mass 20 a.m.u.. The average temperature is 300 K and the temperature difference between the contacts is 10 K. When the size effect of period thickness d_{SL} is under study, the total number of atoms in the device in our NEGF simulations is 240. When size effect of the total sample thickness L is under study, the period thickness d_{SL} is 24 atoms.

To determine the coherent transport regime, we follow the general definition and use the coherence length l_c to compare with system dimensions. In order to calculate the coherence length, the built-in spatial correlation function of atomic displacements $G^n(x, x', \omega)$ in NEGF is used. We follow the steps to study and obtain the coherence length in ref. [129]. The degree of coherence can be calculated by the weighted correlation function:

$$\mu(x, x', \omega) = \frac{G^n(x, x', \omega)}{[G^n(x, x, \omega)]^{1/2}[G^n(x', x', \omega)]^{1/2}} \tag{4.10}$$

and the spatial cross correlation $C(\Delta x, \omega)$ is written as:

$$C(k\Delta x, \omega) = \frac{1}{N-k} \sum_{i=1}^{N-k} \mu(x_i, x_{i+k-1}, \omega), k \in (0...N-1) \tag{4.11}$$

where N is the number of atoms in the device (Fig. 4.1), x_i is the location of the ith atom.

The spatial cross correlation function $C(\Delta x, \omega)$ is further normalized in the following way to quantify the decay and thus the correlation length l_c [129]:

$$l_c^2(\omega) = \frac{\sum_{k=0}^{N-1} |C(\Delta x, \omega)|^2 (k\Delta x)^2}{\sum_{k=0}^{N-1} |C(\Delta x, \omega)|^2} - \left(\frac{\sum_{k=0}^{N-1} |C(\Delta x, \omega)|^2 k\Delta x}{\sum_{k=0}^{N-1} |C(\Delta x, \omega)|^2} \right)^2 \tag{4.12}$$

In the following work, $l_c(\omega)$ is compared with two superlattices dimensions: the period thickness d_{SL} and the total superlattice (device) thickness L to discuss the role of size effects and transport regimes.

4.3.1 Size effects in superlattices: κ versus period thickness

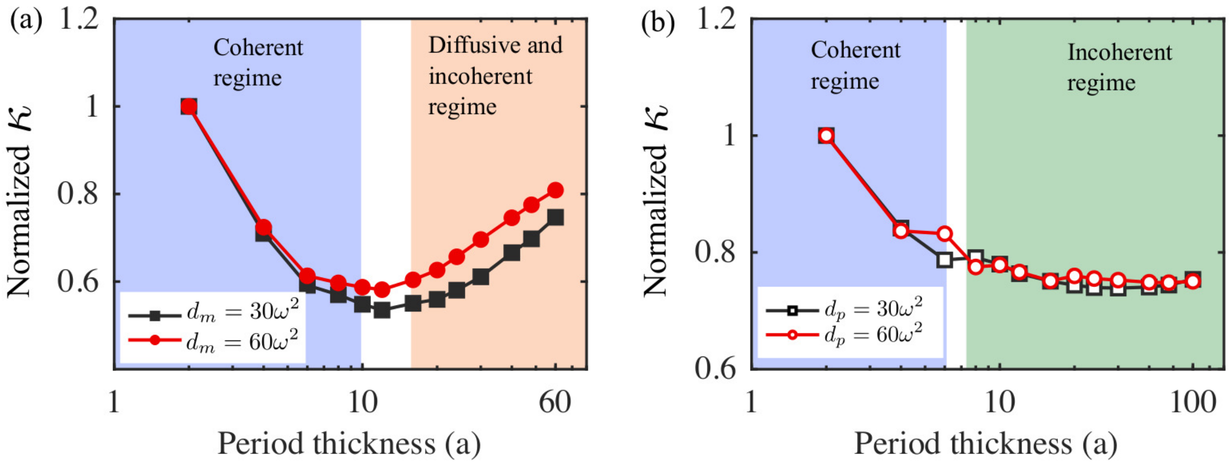

Figure 4.6: Normalized thermal conductivity (relative to the thermal conductivity of d_{SL}=2 u.c. superlattices) of 1D superlattices versus period thickness d_{SL} with scattering mechnism (a) both momentum and phase scattering and (b) dephasing only scattering.

The minimum thermal conductivity of superlattices is reproduced by the “momentum + phase scattering” model (Fig. 4.6(a)). This is consistent with the observed results by experiments [124] and theories [24] since at room temperature the phonon interactions involve both momentum relaxation and dephasing. Moreover, as the scattering strength increases, d_m, the period thickness for the minimum thermal conductivity becomes shorter and the depth of the minimum becomes shallower. This phenomena is again reflected in the experimental data of thermal conductivity of ($SrTiO_3$)-($CaTiO_3$) superlattices with an increasing temperature [124]. However, none of these features can be reproduced using the ‘dephasing only’ scattering model (Fig. 4.6(b)), for which the dephasing process only destroys the phonon wave interference, leaving the transmission to be the average of the one without scattering (Fig. 4.7).

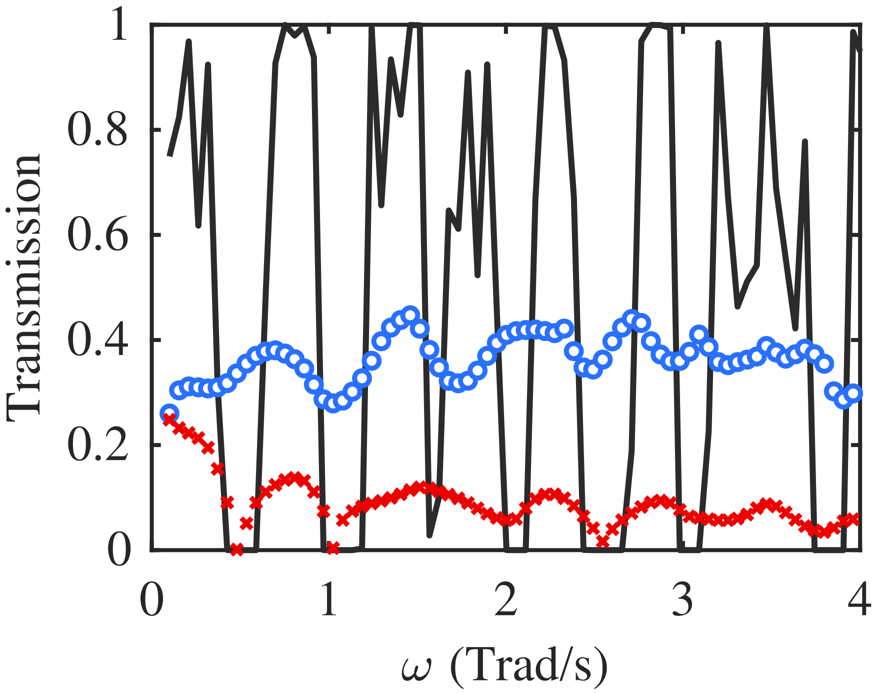

Figure 4.7: Transmission of 1D superlattices without scatterings (black line), with ‘dephasing only’ scattering (blue circles) and with ‘momentum relaxing and dephasing’ (red crosses). Oscillations are destroyed by both scatterings, but the ‘momentum relaxing and dephasing’ scattering introduces additional resistances while dephasing only preserves the average. The period thickness for this plot is d_{SL}=20 u.c. and the scattering strength $d_m = 60\omega^2$ and $d_p = 60\omega^2$.

Figure 4.7 shows the transmission for the coherent SL without scatterings (black line), dephasing only (momentum conserving) scattering (blue circles) and momentum relaxing dephasing scattering (red cross). The phases and oscillations of the transmission are partially destroyed by both 'dephasing only' and 'momentum relaxing and dephasing' scatterings. However, the average transmission of the SLs with the 'momentum relaxing scattering' is much lower than the other, indicating an additional resistance is added by the momentum scattering while the 'dephasing only scattering' only removes the phases and interferences. Consequently, the transmission of 'dephasing only' system is an average of the purely coherent one and the area under both curves should be equal if the system is well converged [132].

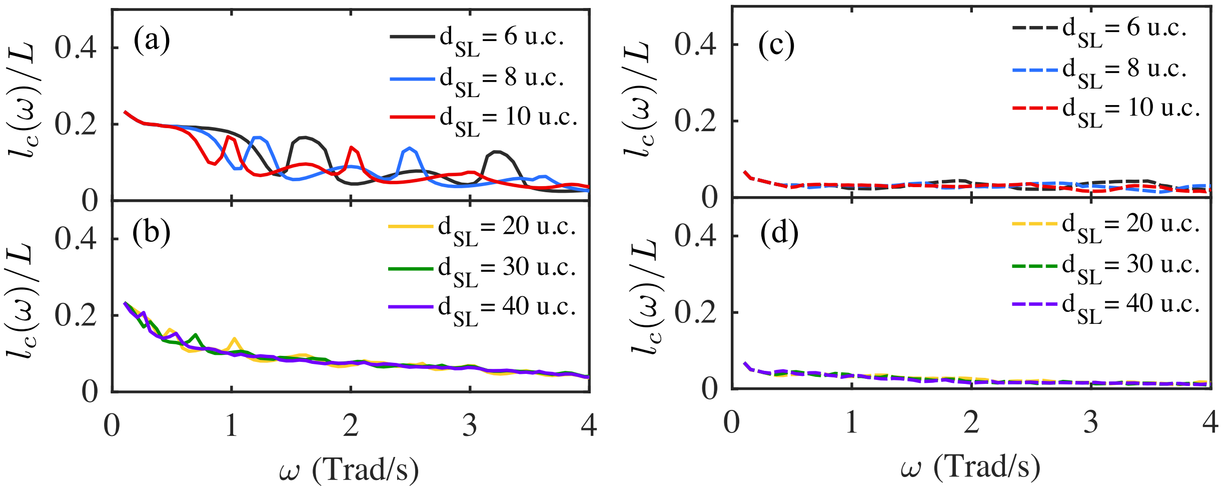

Figure 4.8: The normalized coherence length $l_c(\omega)$ for L is 240 atoms. (a)(b) momentum relaxing and dephasing scattering systems; (c)(d) dephasing only scattering systems. For all the simulations in this figure, the scattering strength $d_m = 60\omega^2$ and $d_p = 60\omega^2$.

The coherence length variations with the period thickness d_{SL} for both scattering mechanisms are presented in Fig.4.8. For momentum relaxing and dephasing, $l_c(\omega)/L$ shows substantial variations with d_{SL} for $d_{SL} <= 10$ u.c. (Fig.4.8(a)). This demonstrates that when $l_c(\omega)$ is longer than 10 u.c., phonon wavefunctions can transport across the interface and interfere with phonon waves in the adjacent periods, forming new band structures and dispersions. These new dispersions depend on the periodicity of the SLs (period thickness), leading to the observed variation of $l_c(\omega)$ with d_{SL}. In contrast, $l_c(\omega)$ becomes independent of

d_{SL} when d_{SL} >20 u.c. (Fig.4.8(b)). This suggests $l_c(\omega)$ <20 u.c., and no phonon dispersion is formed by varying the periodicity above l_c.

The relation between $l_c(\omega)$ and d_{SL} to determine the transport regime for momentum relaxation plus dephasing scattering is further analyzed by plotting $\log_{10}[l_c(\omega)/d_{SL}]$, as shown in Fig. 4.9(a), and for dephasing only in Fig. 4.9(b). The horizontal line in both at zero denotes the separation of the coherent regime and incoherent regime. The transport is coherent in d_{SL} <=6 u.c. systems and incoherent in d_{SL} >=24 u.c. systems. For the 16 u.c., the system is in a transition regime between these two since the low-frequency long-wavelength phonons are coherent and the high-frequency phonons are incoherent. This separation is consistent with the minimum conductivity figure (Fig. 4.6(a)).

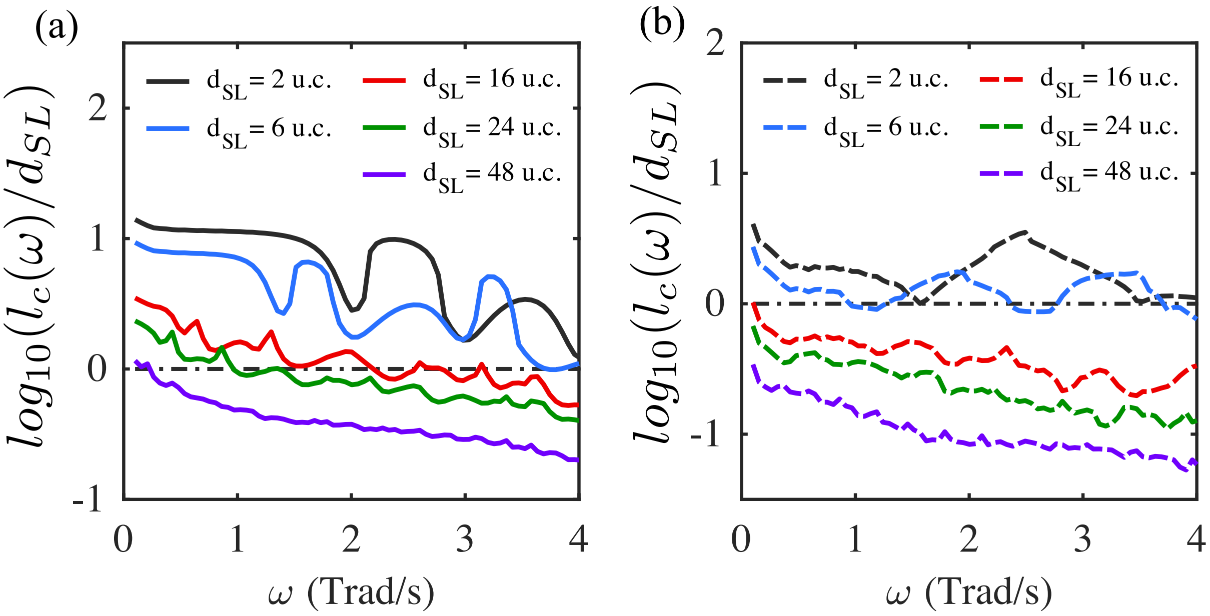

Figure 4.9: $\log_{10}[l_c(\omega)/d_{SL}]$ to determine the transport regime (coherent vs. incoherent) for (a) 'momentum relaxation plus dephasing' systems and for (b) 'dephasing only' systems. The horizontal line in both (a) and (b) denotes the separation of the coherent regime and incoherent regime.

$l_c(\omega)/L$ for the 'dephasing only' system shows a much lower coherent length than the system including momentum scattering (Fig. 4.8)(c)(d) and Fig. 4.9(b)). Varying d_{SL} from 6 u.c. to 10 u.c. leads to negligible change in $l_c(\omega)$. So the system is incoherent from 6 u.c.

which is a much shorter coherent regime than 10 u.c. for the system including momentum scattering, as confirmed by the conductivity versus d_{SL} figure 4.6(b). This comparison is solely due to the mathematical description of these two kinds of scatterings. The 'momentum relaxing dephasing' does not mean adding momentum scattering to the 'dephasing only' system. Instead, it is the difference in the format of the scattering matrix Σ_s (Eq. 4.6, Eq. 4.7). The scattering terms are added to every entry of the potential correlation matrix of the 'dephasing only' system, while they are only added to the diagonal entries of the 'momentum relaxing dephasing' system.

In summary, the discussion in this section tells us that the minimum conductivity for the system including both momentum relaxing and dephasing, is indeed a criteria to determine the transport regimes. The decrease of κ_{SL} versus d_{SL} is a coherent phenomenon. However the increase of κ_{SL} with d_{SL} is a size effect that exists both in the incoherent and the diffusive regime, and κ_{SL} shows a saturation with d_{SL} in the pure incoherent regime without momentum scattering.

4.3.2 Size effects in superlattices: κ versus total sample length

In the previous section, we look at the size effect of period thickness d_{SL} on the heat conduction of superlattices from coherent and incoherent regimes under two different scattering mechansims. In this section, we study the impact of the total sample thickness L. Fig. 4.10 shows the influence of L by including 'momentum relaxing and dephasing'. When the system is in the coherent regime (when d_{SL}=6 u.c.), the coherence length shows a dependency on L, especially for the low-frequency phonons, as shown in Fig. 4.10(a). This can be understood since the coherence length determines the extent of the wave packets [129], thus this length is influenced by the number of wave packets involved in the interaction, and thus by the total number of periods and total thickness. When d_{SL}=24 u.c., and the system enters the incoherent regime, the coherence length is almost independent of L, as shown in Fig. 4.10(b). For high-frequency phonons with coherent length shorter than d_{SL}, their coherent lengths

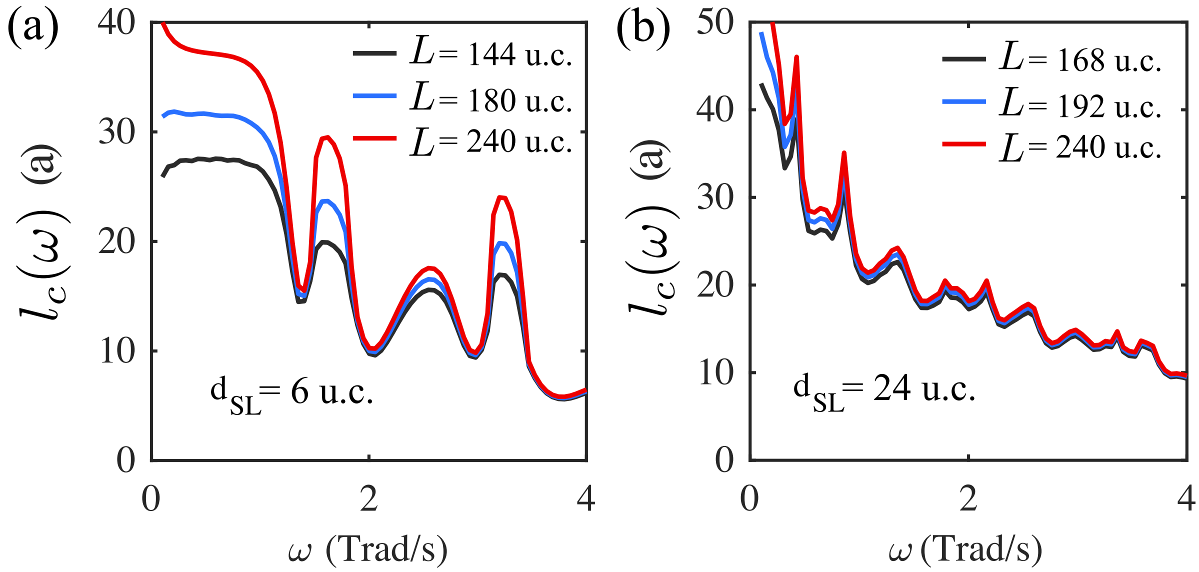

Figure 4.10: The influence of total sample thickness L on the coherence length of superlattices with (a) d_{SL}=6 u.c. and (b) d_{SL}=24 u.c. under 'momentum relaxing and dephasing' scattering.

are independent of L because the phonon wave packets cannot interact with each other. For the small portion of low-frequency phonons that have l_c larger than d_{SL}, the coherent length changes with L.

The coherent regime for systems with 'dephasing only' scatterings happens at d_{SL} <6 u.c., much shorter than that for the systems with 'momentum relaxing and dephasing' scattering. This is further confirmed by $l_c(\omega)$ vs. L with d_{SL} =6 u.c. in Fig. 4.11. The coherence length is almost invariant with L at this point.

The thermal conductivity of the 1D superlattices as a function of L is plotted in Fig. 4.12. Without scattering, κ increase linearly with L, which is interpreted as a ballistic behavior. When 'momentum relaxing and dephasing' scattering is included, κ increases and saturates with L, indicating a ballistic to diffusive transition. However, if only dephasing scattering is included in the system, κ follows the ballistic trend, which is consistent with our previous discussion that the dephasing scattering only removes the oscillations and introduces no resistance to the system.

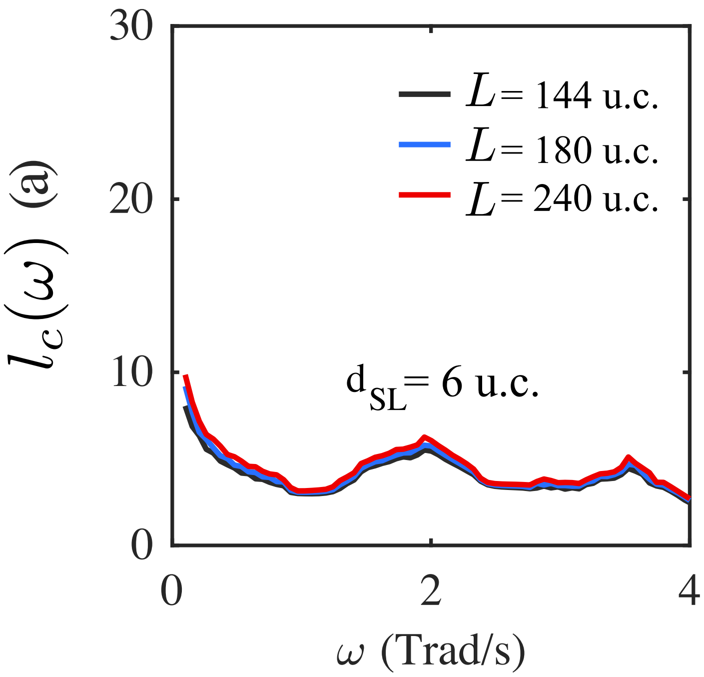

Figure 4.11: The influence of total sample thickness L on the coherence length of superlattices with d_{SL}=6 u.c. under 'dephasing only' scattering.

4.4 Conclusion

In this section, we proposed a method built on NEGF to visualize the scattering mechanisms and transport regimes. In addition, we also introduced two different kind of scatterings to study phonon transport in NEGF. Comparing 'dephasing only' and 'momentum relaxing and dephasing' scatterings, we saw that momentum relaxation is critical to reproduce the minimum thermal conductivity with period thickness d_{SL} and to recover the saturation of thermal conductivty with L. Size effect studies on the coherence length is also performed in this study, with a coherence length funciton that is related to correlation functions in NEGF. We see that a concomitant study of the decay of various correlation components together with the variation of conductance casts clarity on the underlying physics of scattering: momentum versus dephasing scattering and diffusion versus decoherence.

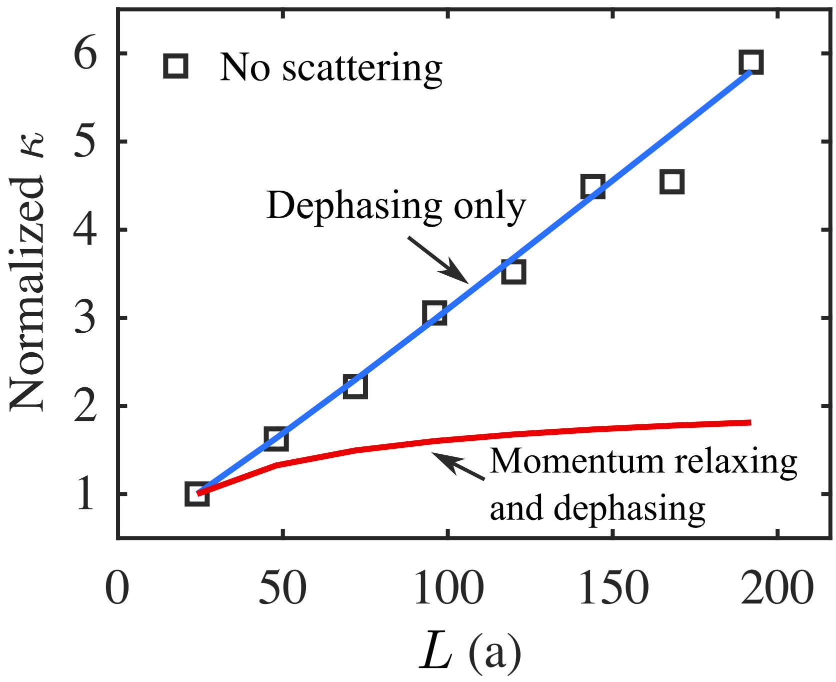

Figure 4.12: Normalized thermal conductivity (relative to the thermal conductivity of L=24 u.c. superlattices) of 1D superlattices versus period thickness L without scattering (black square), with 'dephasing only' scattering (blue line) and with 'momentum relaxing and dephasing' scattering. The period thickness d_{SL} is 24 u.c. for the simulations in this figure.

Chapter 5

Conclusion

This thesis explores the critical role of size effects in various transport regimes for nanoscale thermal transport. The first project of the thesis focuses on bulk thermal transport in two-dimensional materials to quantify the impact of momentum scattering from the ballistic to the diffusive regime; The second project of the thesis looks into nanoscale thermal transport across interfaces; The third project in this thesis introduces a new method to help us understand the transport regimes, to quantify and disentangle various scatterings. Our results greatly expand our fundamental understanding of nanoscale transport physics.

In chapter 2, we compared the thermal conductivity of MoS_2, $MoSe_2$, WS_2 and WSe_2 within the ballistic and the diffusive regimes. We found the order of the thermal conductivity follows the cut-off frequency in the ballistic regime, until the scattering rates take over in the diffusive regime. As a result, there is a flip in the order of the thermal conductivity between these TMDs by either increasing the sample size or the temperature. In addition, we discovered a unique high scattering rate in $MoSe_2$ which results from its unique mid-frequency optical modes that couple acoustic and high frequency optical modes. We conclude in this section that the transport regimes play an important role in comparing the thermal conductivity of bulk materials.

In chapter 3, the impact of size effects on the thermal conductance of a bridging layer is studied. The transport regime is varied either by changing the temperature or by changing the bridge layer thickness. Our results predict a minimum of thermal conductance with varying bridge layer thickness. This minimum separates the coherent regime and a mildly diffusive regime under weak anharmonicity. We also show a maximum in thermal conductance with layer thickness under strong anharmonicity, which is a phenomenon in the strongly diffusive regime. Furthermore, we show that the total resistance can be treated as a summation of interfacial thermal resistances at a length scale much shorter than the bulk mean free path of the intermediate layer, suggesting that the additive regime can be much earlier than the diffusive regime.

In chapter 3, we proposed an exponentially mass-graded interface to maximize thermal conductance by bridging layers. In addition, we demonstrated that the enhancement is strongly dependent on the system dimensions and transport regimes. In the harmonic limit, thermal conductance initially increases with number of layers before saturating. In the transition regime, thermal conductance increases almost linearly with the total junction length by redistributing the phonons from high-frequency modes to the low-frequency high transmission probability modes. Eventually, Umklapp scattering takes over and reduces thermal conductance.

In chapter 4, a method built on Non-Equilibrium Green's Function(NEGF) is proposed to illustrate the scattering mechanisms and transport regimes. Along with four different scenarios of scattering processes (no scattering; only phase scattering; only momentum scattering; momentum and phase scattering), we introduced flexible models to adjust the degrees of phase and momentum separately and applied to superlattices to study the effects of period thickness and total sample length on thermal conductance. By doing so, we find that momentum relaxation is essential in introducing extra resistance to the device/system. Pure dephasing only destroys osscilations and preserves the average transmission.

These studies deepen our fundamental understanding of nanoscale thermal transport not only in bulk materials, but also in heterostructures with interfaces, enabling a better thermal engineering for electronic, optical devices in future.

Future works

Comparing system dimensions with characteristic lengths to determine the transport regimes is not only of fundamental interest, but also of practical importance for engineering heat-dissipation or energy-related applications. There are many challenges left in this topic. One natural extension of this thesis would be to implement the time-dependent Non-Equilibrium Green's Function to study nanoscale transient thermal transport. Injecting phonons from one open boundary contact into the device material at a given wavelength is already discussed in the literature. Visualising how phonons transport across heterostructures with a chosen wavelength, and how they interact with scattering centers like impurities, defects, electrons and other phonons will be substantially useful. The impact on temporal coherence can be additionally studied by this method.

Another topic of great interest is to use band-unfolding techniques to study the scattering rates of phonon modes. The band-unfolding technique can be utilized to study the scattering rates of random scattering centers compared to the original system without those scattering centers. This technique is more accurate than predicting scattering rates by uncorrelated events described by Fermi's golden rule or Klemen's scattering rule. By simulating a large supercell with different scattering centers, and unfolding the dispersions to the original pristine enlarged Brillioun zone, the bandwidth of phonon band branches, which is twice the scattering rates, can be obtained. The successful implementation of this technique with first principles parameters will lead us to understanding of many unresolved experimental data in the ballistic regime for short sample dimensions.

Appendices

Appendix A

Effects of random interface mixing on thermal transport in superlattices

A.1 Background and Motivation

The minimum in thermal conductivity of superlattices (SLs) with the superlattice period thickness is absent in most experiments, despite a large number of simulation works in the literature predicting the existence of the minimum. [24, 139–141] There is actually only one recent work on $SrTiO_3$-$CaTiO_3$ superlattice providing a proof of the minimum in thermal conductivity of SLs in experiment. [124]

The absence of the minimum thermal conductivity in experiments can be caused by many geometry imperfections: large lattice mismatch between materials composing the superlattices, the imperfect periodicity of superlattices and interfacial interatomic mixing. A possible explanation of its absence is that these geometrical imperfections destroy phonon coherence and add incoherent contributions to the phonon transport. Among various factors, random interfacial mixing is the most common, and inevitably exists in superlattice samples based on current fabrication technology.

The role of random interfacial mixing in thermal transport across superlattices was studied intensively in recent literature. That random interfacial mixing eliminates the minimum of κ_{SL} with period thickness d_{SL} was verified by simulations of NEMD [142–144], NEGF [143] and lattice dynamics [144,145] on specific superlattices (composed by Lennard-Jones models of Argon-heavy Argon [142], Si-Ge [143] and Gr-hBN [144]) heterostructures. Random interfacial mixing is also reported to lower the lifetime [145](and transmission [143]) of medium to high frequency phonons, while it broadens the entire phonon power spectra to add more propagating channels [145]. However, detailed explanations of the relation between random interfacial mixing and phonon incoherence are scarce in the literature.

One recent paper initiated the discussion on this relation from Ghosh's group and Hopkins's group, combining simulation and experimental studies on GaAs-AlAs superlattices. [146] This work provided a comprehensive study on the size effects of superlattices demonstrating coherent phonons. To that end, both period thickness d_{SL} and total sample thickness L were varied systematically, with d_{SL} changed from 2 nm, 12 nm to 24 nm and L changed from 20.1 nm to 2160 nm in experiments. The same sizes setup were also used in simulations. Non-equilibrium Green's Function based simulations with first principles parameters were performed for the same material structures with both clean interfaces and interfaces with random mixings. (In this work, Ramez Cheaito did measurements of the thermal conductivity of GaAs-AlAs superlattices, Jingjie Zhang extracted first principles parameters and simulated the superlattices with random interfacial mixings, and Carlos Polanco simulated the superlattices with clean interfaces.)

The most important result from this work was that it validated the two prevailing approaches for demonstrating phonon coherence. Other than the aforementioned approach of the minimum κ_{SL} with d_{SL}, the other approach is the linear dependence of κ_{SL} with the total sample thickness L. The linear dependence of κ_{SL} implies that the interfacial thermal conductance G_{SL} is a constant and so is the transmission. As a result the superlattice is treated as a new homogeneous material, and no phonons are scattered by the interfaces.

This linear dependence on L of GaAs-AlAs superlattices thermal conductivity is reported

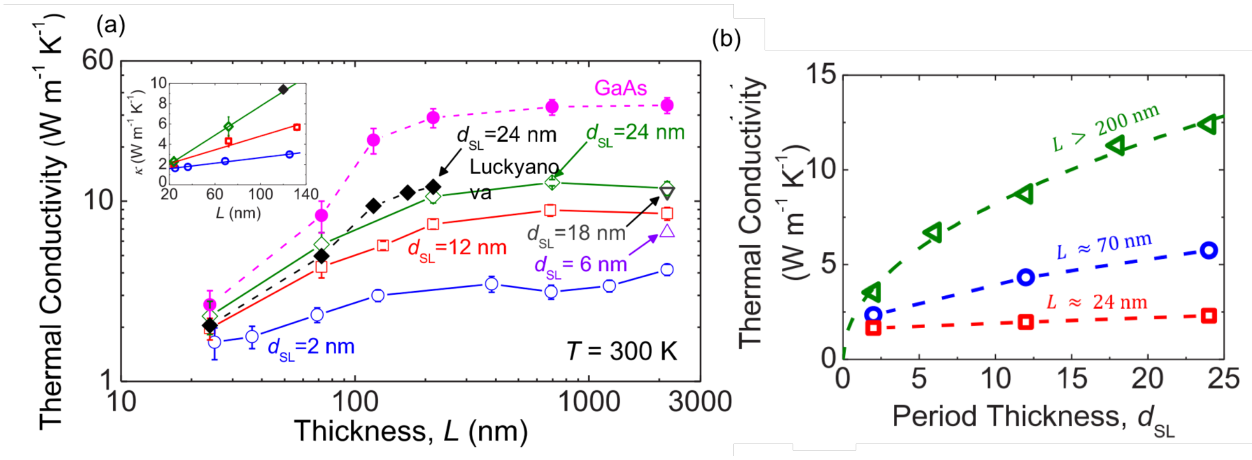

Figure A.1: (a) The measured thermal conductivity of three sets of GaAs-AlAs SLs with 2, 12, and 24 nm period thicknesses and a set of GaAs thin films plotted versus the total sample thickness, L, at room temperature. The inset is a zoomed view of the data for samples with $L < 136$ nm plotted on a linear-linear scale. (b) Selected data from (a) plotted versus period thickness, d_{SL}. This figure is reproduced from our previous publication Physical Review B 97, no. 8 (2018): 085306. [146]. The figures are plotted and the measurements are conducted by Ramez Cheaito from Prof. Patrick Hopkins's group.

recently [125], suggesting the existence of phonon coherence. However, this reported data is only measured for samples with d_{SL} fixed at 24 nm, and as a result cannot be used to verify the existence of a minimum of κ_{SL} with varied d_{SL}. In our paper, Ramez measured κ_{SL} of GaAs-AlAs superlattices with systematically varied d_{SL} and L, and showed a consistency with the data measured in Ref. [125] (Fig. A.1(a)). However, κ_{SL} increases with d_{SL}, showing no minimum in κ_{SL} (Fig. A.1(b)). A monotonic increase of κ_{SL} versus d_{SL} is found, suggesting that the phonon transport is incoherent, contradicting the previous theoretical conclusion.

The simulation results assist us in identifying the origin of the discrepancy between these two approaches. First of all, the approach of linear dependence of κ_{SL} on L is validated by our clean interface calculations (note the simulation is performed with the harmonic Green's function method, where anharmonic scattering is not included). As the number of periods and the length of the SLs increase, the clean interface conductance (S) initially decreases and then plateaus (Fig. A.2(a)). The plateau results from coherent phonon transport, since the conductance does not decrease in spite of the increase in the number of interfacial scattering

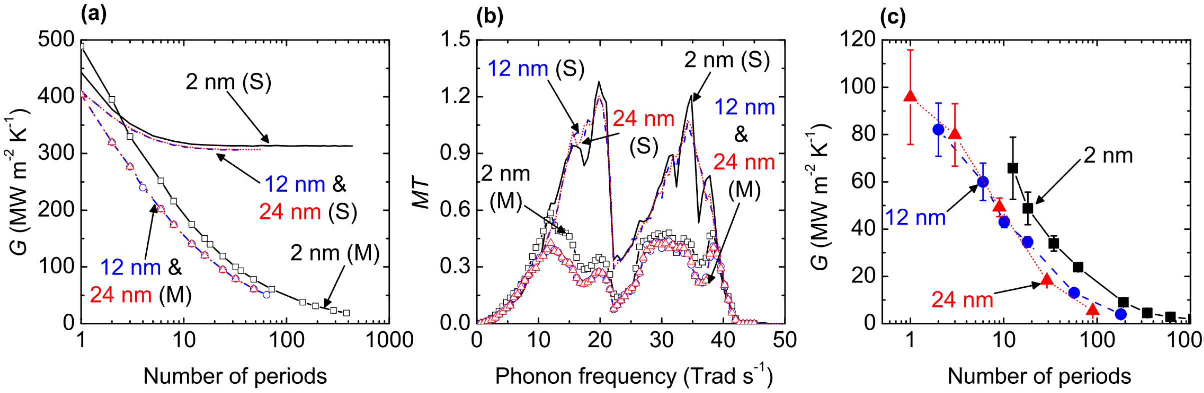

Figure A.2: (a)Conductance vs. number of periods for SL with atomically smooth (S) and mixed (M) interfaces.The decrease in conductance of the SLs with interatomic mixing at the interfaces results from incoherent phonon transport. (b)MT per perpendicular unit cell for SL with atomically smooth (S) and mixed (M) interfaces. The decrease in $M\bar{T}$ as the number of periods increases shows the corresponding decrease in transmission, which is a signal of incoherent phonon transport. For these calculations, the total sample thickness is set to 12 periods of AlAs-GaAs for each sample regardless of the period. (c) Experimental data replotted as conductance vs. number of periods. The data show that conductance is independent of period for short samples with long periods. This figure is from our previous publication Physical Review B 97, no. 8 (2018): 085306. [146]. Jingjie Zhang extracted first principles parameters and simulated the superlattices with random interfacial mixings, and Carlos Polanco simulated the superlattices with clean interfaces.

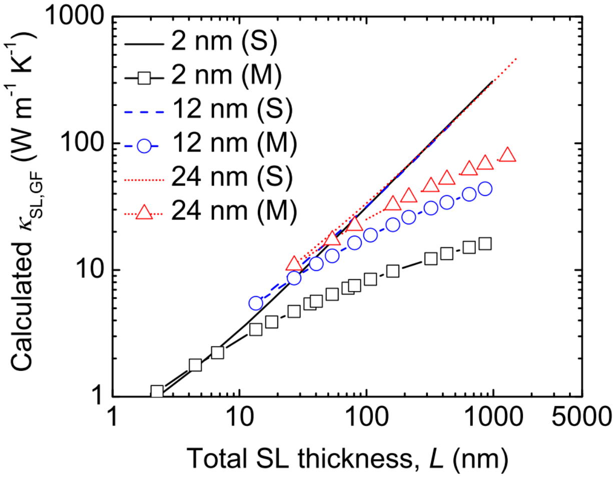

Figure A.3: Thermal conductivity of AlAs-GaAs SLs calculated via our Green's function analysis (κ_{SL},GF) vs. number of periods for SLs with atomically smooth (S) and mixed (M) interfaces. For SLs with perfect interfaces, the slope is nearly independent of the period. For SLs with mixed interfaces, the slope seems linear in spite of incoherent phonon transport. We note that for this calculated value for κ_{SL},GF does not include phonon-phonon interactions. This figure is from our previous publication Physical Review B 97, no. 8 (2018): 085306. Jingjie Zhang extracted first principles parameters and simulated the superlattices with random interfacial mixings, and Carlos Polanco simulated the superlattices with clean interfaces.

centers. The initial decrease in the conductance is a result of the evanescent phonons in infinitely long SLs. The magnitudes of those phonons do not decay to zero in a SL with only a few periods because the interference of vibrational waves backscattered at each interface is not strong enough to cancel the incident wave [146].

However, the experimental data (Fig. A.2(c)) is only consistent with the mixed interface simulations (M) (Fig. A.2(a)), where the conductance G decreases monotonically with the number of periods. This decrease is supported by the decrease in transmission $M\bar{T}$, as shown in Fig. A.2(b), and is a consequence of incoherent phonon transport. The conductance not saturating after a few periods means that most of the phonons scatter at interfaces, and the SL dose not behave as a new homogeneous material.

The simulation results suggest that the discrepancy between these two approaches in demonstrating phonon coherence arises from the quasi-linear slope in κ_{SL} versus L. Although the linear dependence of κ_{SL} on L is a good demonstration of coherent phonon transport, the slope of κ_{SL} versus L for SL samples with a small number of periods is easily misinterpreted as linear (as shown in Fig. A.3). Consequently, the linear dependence of κ_{SL} with L reported for 24 nm period thickness GaAs-AlAs superlattices is not a solid proof for coherent phonons. [125] An improved version of this approach is using the dependence of conductance instead of conductivity on the total sample thickness L, or the comparison of slopes of κ_{SL} with L for a set of samples with several different period thicknesses.

This previous work elucidates the discrepancy of two prevailing approaches demonstrating the phonon coherence. It additionally demonstrates that random interfacial mixing destroys phonon coherence. ***However, how the stochasticity of interatomic mixings at the interfaces destroys the phonon coherence was not answered by this paper nor in the literature.***

A.2 Future Possibilities

In order to understand how the stochasticity of the interatomic mixings at the interfaces destroy the phonon coherence, one can start with the following project (sketched in detail in Fig. A.4), which would deepen our understanding of phonon coherence and the role of stochasticity of the interfacial defects and mixings:

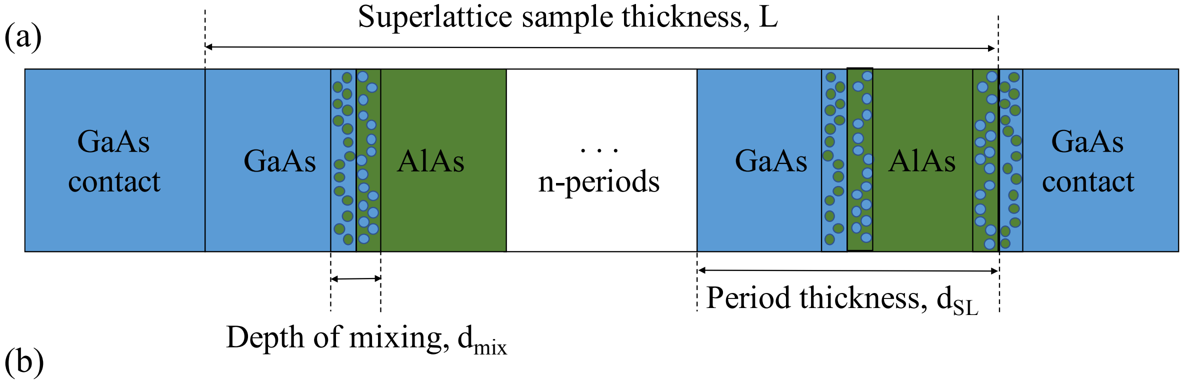

(b)

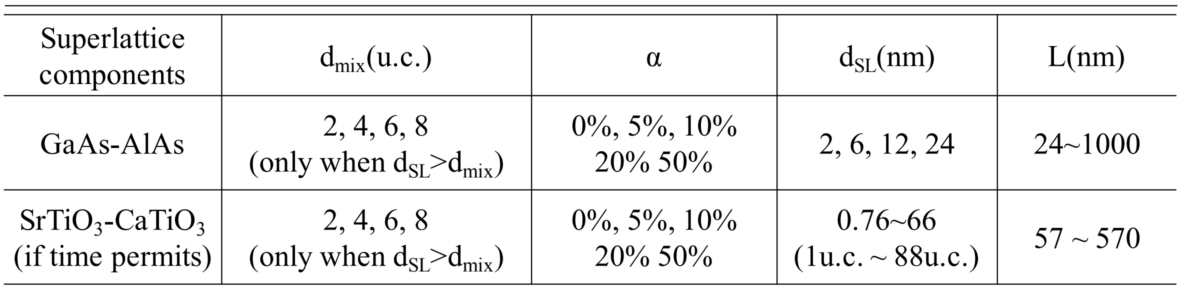

Superlattice components	d_{mix}(u.c.)	α	d_{SL}(nm)	L(nm)
GaAs-AlAs	2, 4, 6, 8 (only when $d_{SL}>d_{mix}$)	0%, 5%, 10% 20% 50%	2, 6, 12, 24	24~1000
$SrTiO_3$-$CaTiO_3$ (if time permits)	2, 4, 6, 8 (only when $d_{SL}>d_{mix}$)	0%, 5%, 10% 20% 50%	0.76~66 (1u.c. ~ 88u.c.)	57 ~ 570

Figure A.4: (a) A sketch of the GaAs-AlAs superlattice system will be studied in this project, and (b) parameters that are considered and varied in the project. α is the probability of Ga atoms of the GaAs layers being randomly replaced by Al atoms (or the probability of Al atoms of the AlAs layers being replaced by Ga atoms).

(1) *Study the random mixing impact on size effects of superlattices.*

At this step, the percentile of mixing α is fixed at 20% and depth of mixing d_{mix} is fixed at 2 u.c. in GaAs-AlAs superlattices. (α is defined as: the chance of Ga atoms of the GaAs layers within the depth of mixing d_{mix} being replaced by Al atoms, or vice versa for Al atoms of the AlAs layers. The definition of depth of mixing is shown in Fig. A.4(a).) A systematic variance of the period thickness (2 nm to 24 nm) and the total sample thickness (24 nm to 1000 nm) should be controlled.

Two results should be delivered in this step:

- During the simulations, the correlation function G^n will be calculated and stored, and the coherence length l_c will be calculated accordingly. A demonstration of how these two quantities are affected by the mixing and how the sample dimensions affect these quantities will be delivered in this step.

- The random mixings at the interface can lower the transmission or lifetime of medium to high frequency phonons while the transmission of low frequency phonons can be enhanced. [97] This phenomenon was never been explained in detail. One possible explanation is that the mixing breaks the translatonal symmetry (as a result, breaks the transverse momentum q conservation), and adds more phonon propogating modes into the system. This can be shown by plotting $M\bar{T}$ (calculated by NEGF) in the Brillouin Zone for systems with or without interfacial mixings.

(2)*Study the impact of percentile and depth of mixings.*

In this step, the depth of mixing will be changed from 2 u.c. to 8 u.c., and the percentile of mixing α is varied from 0%(no mixings) to 50%. The purpose of this kind of study is that the quality of the superlattice interfaces could be one of the contributing factors that destroy the minimum κ_{SL} with d_{SL}. We want to demonstrate how much mixing is needed to destroy the minimum, and relate that to physical arguments, such as intersubband scattering by Fermi's Golden Rule when l_c approaches the dominant mid-frequency phonon wave length.

(3) *The role of material components on the size effects in superlattices.*

A similar calculation on $SrTiO_3$-$CaTiO_3$ superlattices can then be carried out. Existing published measurements on $SrTiO_3$-$CaTiO_3$ superlattices demonstrate a minimum, but not so in GaAs-AlAs superlattices. The underlying reason is that the coherence length in $SrTiO_3$-$CaTiO_3$ superlattices is 3∼4 nm and in GaAs-AlAs superlattices is around 1∼2 nm. Our proposed calculation can help us understand the possible contributions (mass differences, and dispersion differences) to the differences in coherence length of these two types of superlattices.

The purpose of the proposed project of random mixing at the superlattice interfaces is to study how the stochasticity of the interatomic mixing destroy the phonon coherence, executed utilizing our new idea of monitoring off-diagonal elements of lesser Green's function G^n. The significant difference between this proposed work with our previous study is that the lesser Green's function (or correlation function) G^n is introduced into the calculations, and the proposed project will study how the phonon coherence length l_c (extracted from G^n) changes with the period thickness and total sample thickness (Eq. 4.10, 4.11 and 4.12, which are elaborated here). The normalized correlation function is defined as (x is the transport direction):

$$\mu(r, r', \omega) = \frac{G^n(x, x', \omega)}{[G^n(x, x, \omega)]^{1/2}[G^n(x', x', \omega)]^{1/2}} \tag{A.1}$$

and the spatial cross correlation $C(\Delta x, \omega)$ is written as:

$$C(k\Delta x, \omega) = \frac{1}{N-k} \sum_{i=1}^{N-k} \mu(x_i, x_{i+k-1}, \omega), k \in (0...N-1) \tag{A.2}$$

where N is the number of atoms in the device (Fig. 4.1), x_i is the location of the i^{th} atom.

The spatial cross correlation function $C(\Delta x, \omega)$ is further normalized in the following way to quantify the decay and thus the correlation length l_c [129]:

$$l_c^2(\omega) = \frac{\sum_{k=0}^{N-1} |C(\Delta x, \omega)|^2 (k\Delta x)^2}{\sum_{k=0}^{N-1} |C(\Delta x, \omega)|^2} - \left(\frac{\sum_{k=0}^{N-1} |C(\Delta x, \omega)|^2 k\Delta x}{\sum_{k=0}^{N-1} |C(\Delta x, \omega)|^2} \right)^2 \tag{A.3}$$

A.3 Challenges

The challenges to execute this project that I faced arise from the large dimensions of the system in study. Accordingly, the matrix size for the Hamiltonian and Green's function of the superlattice are too large and needs better algorithm to execute on available clusters, CPU time and memory.

Challenge 1: Simulation of superlattices up to 1000 nanometers long.

Atomic Green's function simulations are usually limited to a range of several tens of nanometers, but the systems studied in this project will need to be extended to 1000 nanometers, depending on the phonon mean free paths. For instance, to achieve the diffusive regime transport, the total sample thickness of the GaAs-AlAs superlattice should be at least 200 nanometers (as shown by thermal conductivity saturation length in Fig. A.1(a)). Even if we consider only 1 conventional unit cell in the cross-section area and only calculate transport for phonons with a certain wavevector q_0, and set the frequency grids as 50, the matrix dimension for Green's function of the device (or the superlattices we want to study) is $[4.8\times10^5, 4.8\times10^5]$ (The dimension of the matrix 4.8×10^5 is obtained by $(L/a) \times \mathrm{dof} \times N_a \times N_k \times N_{uc,\perp} \times N_\omega = (\frac{200}{0.5}) \times 3 \times 8 \times 1 \times 1 \times 50$. Here $(L/a) = (\frac{200}{0.5})$ since the conventional unit cell lattice constant is around 0.5 nm, $\mathrm{dof} = 3$ for 3 degrees of freedom, $N_a = 8$ for 8 atoms in a conventional unit cell, $N_k = 1$ if we only calculate the transport for phonons with a certain wavevector, $N_{uc,\perp} = 1$ if only one unit cell in the transverse direction is considered, $N_\omega = 50$ for the frequency grid) With such a large matrix dimension, it is difficult to do the inversions for the matrix, which are required to calculate the Green's function: $G = [M\omega^2 - K - \Sigma_l - \Sigma_r]^{-1}$, since brute force inversion scales with the matrix size. Not to mention that a periodic boundary condition will need to be enforced in the transverse direction, and a grid of wavevectors in the Bouillon Zone will be used. In our previous simulations for the GaAs-AlAs superlattices, we used a 20×20 wavevector grid in the Fourier space and 3×3 conventional unit cells in real space. If we use the regular expression of Green's function to treat the GaAs-AlAs superlattice, then the matrix dimension for the Green's function will be $[8.64 \times 10^9, 8.64 \times 10^9]$ for 1000 nm SLs ($(L/a) \times \mathrm{dof} \times N_a \times N_k \times N_{uc,\perp} \times N_\omega = (\frac{1000}{0.5}) \times 3 \times 8 \times 400 \times 9 \times 50$). Considering each double float number requires 8 bytes in memory, this matrix dimension will be [69.12GB, 69.12GB] memory which is far beyond the maximum matrix size in most of languages in spite of the platforms. For instance, the maximum matrix size can be held in Matlab is shown in

Fig. A.5 This incredible large number makes this project challenging.

Possible solution: Dyson's equation

The approach that I used for the previous paper is Dyson's Equation which provides a new route to solve the Green's function by splitting the device into several layers. An illustration is shown in Fig. A.6. The most common procedure to solve the Green's function and obtain the transmission is by $M\bar{T} = \text{Trace}[\Gamma_l G \Gamma_r G^{\dagger}]$, where $\Gamma_{l,r}$ are the broadening matrices for the left and right contact, and $G_d = (M_d\omega^2 - K_d - \Sigma_l - \Sigma_r)^{-1}$ is the retarded Green's function for the device, M_d, K_d are the mass and force constant matrices of the device, $\Sigma_{l,r}$ are the self-energies that account for the phonons exiting to the contacts. Dyson's equation enables us instead of considering G_d for the whole device, to solve the problem layer by layer from right (N) to left (1) or (left (1) to right (N)) sequentially.

In the following, we will walk through the process layer by layer start from right to left. The self energy of the right contact (same for the left contact) can be expressed as $\Sigma_r = K_{N,r} g_r K_{r,N}$, where $K_{N,r}$ is the interaction between the layer N and the right contact. g_r is the surface Green's function for the right semi-infinite contact. Note that the term g_r represents the Green's function for the first layer in the contact region considering everything on the right, and assumes the right contact is not connected to any material. With the open system boundary self-energy, the surface Green's function for the N$^{\text{th}}$ and N-1$^{\text{th}}$ layer can be written as:

$$\begin{aligned} g_{N,N} &= (M_N\omega^2 - K_N - \Sigma_r)^{-1} \\ g_{N-1,N-1} &= (M_{N-1}\omega^2 - K_{N-1} - \Sigma_N)^{-1} \end{aligned} \tag{A.4}$$

where M_N, K_N (or M_{N-1}, K_{N-1}) are the mass and force constants matrix of the N$^{\text{th}}$ (N-1$^{\text{th}}$) layer. Σ_r is expressed previously; I want to elaborate Σ_N here: $\Sigma_N = K_{N-1,N} g_{N,N} K_{N,N-1}$. Then layer by layer, walking from the right to the left, the problem to solve a very large matrix for the device with G_d can be reduced to repetitions on a relatively small matrix problem with $G_{1,1} = (M_1\omega^2 - K_1 - \Sigma_l - \Sigma_2)^{-1}$. The generalized equation for this process

Largest (Real Double) Matrix and Total Workspace Size by Platform (MATLAB 7.4, part of R2007a)

Operating system and configuration	Total Workspace Size in MB	Largest Matrix Size in MB	Number of Elements in Largest Real Double Array	Number of Elements in Largest int8 Array
32-bit Windows XP	~1700MB	~1189MB	~155e6	~1246e6
32-bit Windows Vista	~1643MB	~1428MB	~187e6	~1497e6
32-bit Windows XP, best case, with 3GB switch	~2700MB	~1536MB	~200e6	~1610e6
32-bit Linux	~2683MB	~2385MB	~312e6	2^{31}-2 (~2147e6)
MAC OS X running 32-bit MATLAB	~2919MB	~1532MB	~200e6	~1606e6
64-bit Windows XP running 32-bit MATLAB	~3155MB	~2047MB	~268e6	2^{31}-2 (~2147e6)
64-bit Linux running 32-bit MATLAB	~3558MB	~2292MB	~300e6	2^{31}-2 (~2147e6)
Solaris running 32-bit MATLAB	~3535MB	~3072MB	~402e6	2^{31}-2 (~2147e6)
64-bit Windows XP, Linux or Solaris running 64-bit MATLAB 7.4 and earlier	~<8TB	16GB (double array) / 2GB (int8 array)	2^{31}-2 (~2147e6)	2^{31}-2 (~2147e6)
64-bit Windows XP, Linux or Solaris running 64-bit MATLAB 7.5 and later	~<8TB	<8TB	2^{48}-1 (~2.8e14)	2^{48}-1 (~2.8e14)

Figure A.5: The largest (real double) matrix size by Matlab. This figure is reproducted from https://www.mathworks.com/matlabcentral/answers/91711-what-is-the-maximum-matrix-size-for-each-platform

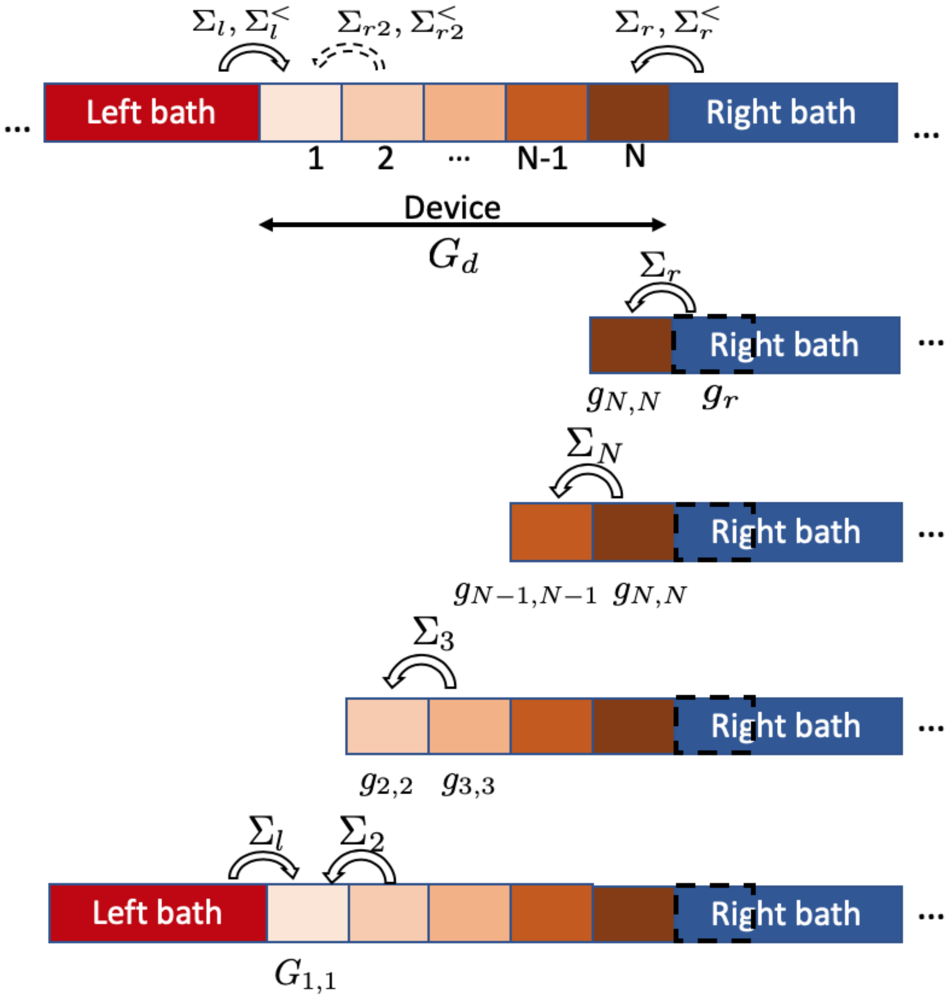

Figure A.6: Scheme of a Dyson set up in NEGF. The system is partitioned into left, right contacts and a device. Self-energies $\Sigma_{l,r}$ represent the phonons loss from the device, and the $\Sigma_{l,r}^<$ represent the phonons injection from left or right contacts to the device.

can be expressed using Dyson's equation as:

$$G_{p,p} = g_{p,p} + g_{p,p}(K_{p,p+1}G_{p+1,p+1}K_{p+1,p})g_{p,p} \tag{A.5}$$

To calculate the coherence length and to visualize the decay of correlation function, the correlation function G^n (or $G^<$, $G^n = -i\hbar G^<$) have to written in terms of Dyson equation as well. This has not been used for phonon transport in the past to our knowledge. Borrowing clues from electron transport, this can be implemented as:

$$\begin{aligned} G^<_{p,p} &= g^<_{p,p} + g^<_{p,p}K_{p,p+1}G^\dagger_{p+1,p} + g_{p,p}K_{p,p+1}G^<_{p+1,p} \\ G^<_{p+1,p} &= G^<_{p+1,p+1}K_{p+1,p}g^\dagger_{p,p} + G_{p+1,p+1}K_{p+1,p}g^<_{p,p} \end{aligned} \tag{A.6}$$

By implementing the Dyson equation to solve the NEGF, the matrix dimension can be greatly reduced. Take our previous system as an example, the matrix dimension of [69.12GB, 69.12GB] can be reduced 1000 fold to [69.12MB, 69.12MB]. However, this is still a large number if the inversions calculated for the matrix. Additional treatments can be done by paralleling the wavevector grid in the Fourier space.

Challenge 2: Simulation of the superlattice with random interfacial mixings - large supercell dimension in the transverse direction

To simulate superlattices with random interfacial mixings, the cross-section area is required to be large enough to consider the mixing atoms. The previous experimental data confirmed that only ~ 1 nm intermixing layer is observed. If only one unit cell is used in the transverse direction, there will be 65.61% chance for GaAs or AlAs layers being free of mixings if the mixing percentage α is 10%. In the previous paper, our simulation supercell uses 9 conventional unit cells with 3 repetitions along each transverse direction. Under this setup, there is only 2.3% chance for GaAs (or AlAs) layers being free of mixings when the mixing percentage α is 10%.

Meanwhile, the phonon wavevector q sampling should be large enough as well. Although we agree that the larger the real space dimension, the smaller the Brillouin Zone size, the shape of the modes times transmission $M\bar{T}$ in the Brillouin Zone is very complex and requires a large sampling. As shown in Fig. A.7, a [20,20] q sampling is not dense enough to capture all the details in $M\bar{T}$.

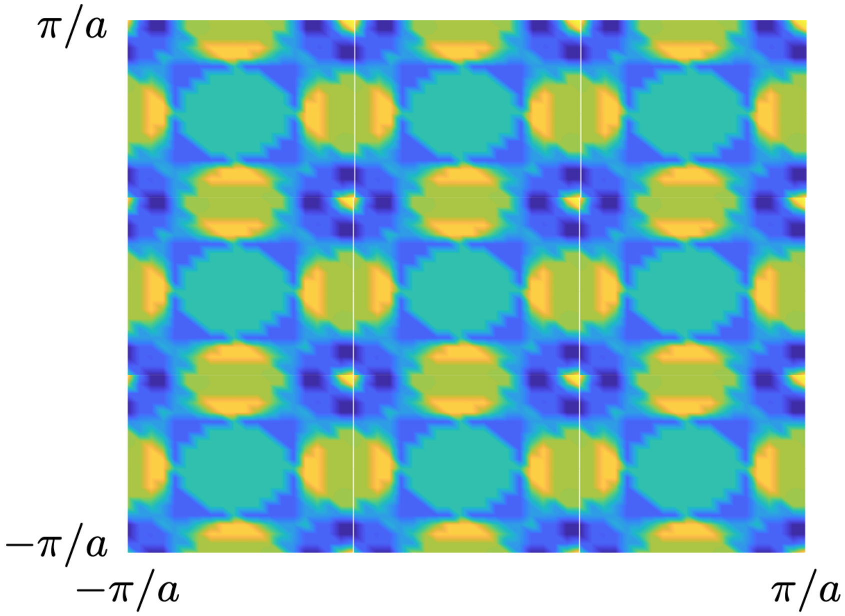

Figure A.7: MT at ω=39.7 Trad/s in the Brillouin zone for a GaAs supercell with [$3a_0$, $3a_0$] cross-section area. $a = 3a_0$ is the supercell size in y/z direction when x is the transport direction, a_0 is the GaAs conventional unit cell lattice constant ($\sim$ 0.56 nm).

One suggestion is to utilize a part of the Brillouin Zone (BZ), e.g. $q_{y,z} \in [-\pi/3a, \pi/3a)$. However, this suggestion is only applicable when the system is periodic in real space, such as GaAs in Fig. A.7. When the system contains randomly distributed interfacial mixings, the supercell is no longer of repetitions of conventional unit cells. As a result, the BZ zone is no longer of repetitions as well, and utilizing only part of the Brillouin Zone leads to loss of essential information in the calculation.

Possible solution: calculate q ***points separately in different batches of simulations.***

Since we simulate systems without anharmonicity, during the phonon transport process, the wavevectors and frequencies are conserved. $M\bar{T}(\omega)$ can be expressed just as the summation over transmission of phonons with different wavevectors: $MT = \sum_{q_\perp} T_{q_\perp(\omega)}$, and separating the calculation into several batches with different $q_\perp$ preserves the result. For instance, assume [20,20] grid is used in the calculation, for every batch we can calculate only [i to i+1, 1 to 20] q grid. And the matrix size can be further reduced to [6.9MB, 6.9MB].

There are other mathematical algorithms or treatments can be done to further scaling the matrices and the problem. 'Partial inversion', 'mode space decoupling' and 'finite element continuum' are the possible solutions, to my knowledge. However, implementing any of these requires some level of understanding of the algorithm and effort in programming.

Challenge 3: Data collection

The solutions to the previous challenges all involve splitting the matrix into smaller ones. However, these solutions also introduce new challenges to the final data analysis.

The separation of wavevector q grid or the frequency ω grid in itself does not cause too much trouble. The reason is that phonons are assumed not to interact with each other, as a result, we can simulate the transport process for each phonon mode separately and sum over the contributions from all the phonon modes in the end.

The separation of the Green's function matrix into layers by Dyson equation will generate a collection of matrices that are the partial elements of the matrix of the device. In order to calculate the coherence length and to visualize the decay process of phonon phases, the correlation function of the whole device is needed. As a result, we need to collect each element (or the small matrices) and rebuild the correlation function matrix $G_d^<$ in the form of the following format:

$$G_d^< = \begin{bmatrix} G_{1,1}^< & G_{1,2}^< & G_{1,3}^< & \dots & G_{1,N}^< \\ G_{2,1}^< & G_{2,2}^< & G_{2,3}^< & \dots & G_{2,N}^< \\ \dots & \dots & \dots & \dots & \dots \\ G_{N,1}^< & G_{N,2}^< & G_{N,3}^< & \dots & G_{N,N}^< \end{bmatrix}$$

. Each element can be solved by Eq. A.6, but each element should be stored during calculations in order to formulate the Green's function for the device. This brings its own memory-related challenges that will need to be overcome.

A.4 Conclusion

All in all, the role of random interfacial mixings on the thermal transport in superlattices is a valuable but also a challenging project to pursuit. A large amount of computing resources from supercomputer centers with large memory cpus, along with a combination of well bench-marked transport algorithms are essential for implementing this project.

Appendix B

DMM from ab-initio NEGF

This work is reproduced with permission from [90] coauthored with Carlos A. Polanco and Avik W. Ghosh. Copyright [2018] ASME. Cite This: J. Heat Transfer. Sep 2018, 140(9): 092405.

The Diffusive mismatch model (DMM) is commonly used to predict the interfacial thermal conductance. In this section, we demonstrate the intrinsic relationship between the Diffusive Mismatch Model (DMM) and the properties from NEGF, and provide an approach to get DMM from first principles NEGF. Instead of using the frequency dependent density of states and velocity from the full non-equilibrium lattice dynamics, we rederive the Diffusive Mismatch Model to go beyond the isotropic approximation. This model stems from the propagating modes, which can be readily calculated using Non-Equilibrium Green's Function and can easily handle inputs from first-principles calculations. This section is partially reproduced with permission from ref. [90].

We start with the description of heat current across the interface in Landauer formula as in Eq. 3.1:

$$q^{1\to 2} = \int_0^\infty (\frac{\hbar\omega}{2\pi} M_1 \bar{T}^{1\to 2})\Delta N dw \tag{B.1}$$

$$q^{2\to 1} = \int_0^\infty (\frac{\hbar\omega}{2\pi} M_2 \bar{T}^{2\to 1})\Delta N dw \tag{B.2}$$

The DMM equations arise under the assumption of detailed balance [147, 148] of the heat so that the current from material 1 to material 2 is equal to the current from material 2 to material 1:

$$q^{1\rightarrow 2} = q^{2\rightarrow 1} \Rightarrow M_1\bar{T}^{1\rightarrow 2} = M_2\bar{T}^{2\rightarrow 1} \tag{B.3}$$

Diffusive process of phonons across the interface assumes that the phonons randomize their phases at one-shot at the interface, consequently the transmission probability of phonons from material 1 to material 2 equals to the reflection probability of phonons from material 2 to material 1 (ie. the history is completely removed):

$$\bar{T}^{1\rightarrow 2} = 1 - \bar{T}^{2\rightarrow 1} \tag{B.4}$$

Combining the Eq. B.3 and Eq. B.4, we get:

$$M\bar{T}_{DMM} = M_1\bar{T}^{1\rightarrow 2} = M_2\bar{T}^{2\rightarrow 1} = \frac{M_1 M_2}{M_1 + M_2} \tag{B.5}$$

M_1 and M_2 are the number of modes of the bulk materials at each side of the interfaces. We can get M_1 and M_2 similarly in Green's functions by defining the contacts and junction as the same materials, using $M\bar{T} = Trace[\Gamma_l G \Gamma_r G^\dagger]$. In the bulk materials, for each mode, transmission probability is 1, so $M\bar{T}$ is just the number of modes. Hence The $M\bar{T}_{DMM}$ equals the number of modes of materials at two sides in parallel.

In a Green's function description, the number of modes is proportional to $AD(\omega)v(\omega)$, where A is the transverse area of the simulated junction unit cell, $D(\omega)$ and $v(\omega)$ are the frequency dependent density of states and velocity respectively. If we write the parallel combination of modes in terms of density of states and velocity, we can recover the general expression often used to describe the DMM from lattice dynamics. For example, in a Au – Self-assembled monolayer (SAM) system, we need to consider the modes of Au and modes of SAMs in the same area. The DMM conductance can be obtained from the combined mode density in parallel:

$$G_{DMM} = \int_0^\infty \frac{\hbar\omega}{2\pi} \frac{(M_1/A_1)(M_2/A_2)}{(M_1/A_1) + (M_2/A_2)} \frac{\partial N}{\partial T} d\omega \tag{B.6}$$

In the following Au-SAM system simulation, we use a compact Au-SAM density with the surface geometry as $\sqrt{3} \times \sqrt{3}$ R30^o. Each alkane chain connects with 3 Au atoms in an area of $2.16 \times 10^{-19} m^2$. The simulated number of modes for Au and alkane chain in that area are shown in Fig. B.1(c), with the inset graph showing the $M\bar{T}_{DMM}$. The number of modes for the Au with that specific density is 3 times as the number of modes of Au in primitive unit cell in (111) direction. Fig. B.1(d) shows the calculated interfacial thermal conductance for the Au-SAMs interface with NEGF-based DMM. The values are almost the same as ref. [148].

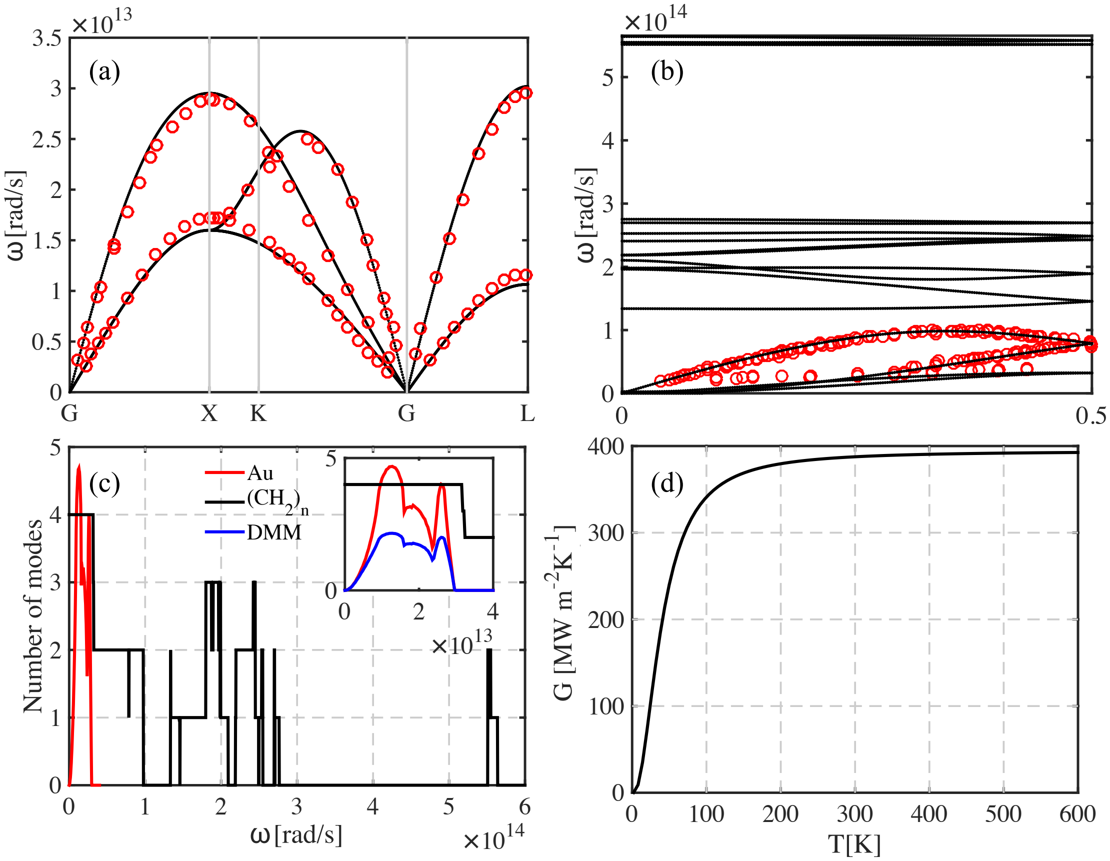

Figure B.1: (A) Phonon dispersion of Au compared with experimental data(red dots); (b) Phonon dispersion of Polyethylene compared with experimental data(red dots); (c) The number of modes of Au and polyethylene. The inset figure shows the $M\bar{T}$ of DMM taking the harmonic mean of modes from each side; (d) The conductance of Au-SAMs junction with NEGF-based DMM.This figure is reproduced from ref. [90]

Appendix C

Publications

C.1 Journal Articles

1. **J. Zhang**, X. Li, K. Xiao, B. G. Sumpter, A. W. Ghosh, L. Liang, "The role of mid-gap phonon modes in thermal transport of transition metal dichalcogenides," Journal of Physics: Condensed Matter, vol. 32, no. 2, pp. 025306, 2019.

2. X. Li, **J. Zhang**, A. A. Puretzky, A. Yoshimura, X. Sang, Q. Cui, Y. Li, L. Liang, A. W. Ghosh, H. Zhao, R. R. Unocic, V. Meunier, C. M. Rouleau, B. G. Sumpter, D. B. Geohegan, and K. Xiao, "Isotope-Engineering the Thermal Conductivity of TwoDimensional MoS2," ACS nano, vol. 13, no. 2, pp. 2481–2489, 2019. **Equal first contribution**

3. R. Rastgarkafshgarkolaei, **J. Zhang**, C. A. Polanco, N. Q. Le, A. W. Ghosh, and P. M. Norris, "Maximization of thermal conductance at interfaces via exponentially mass-graded interlayers," Nanoscale, vol. 11, pp. 6254–6262, 2019. **Equal first contribution**

4. **J. Zhang**, C. A. Polanco, and A. W. Ghosh, "Optimizing the Interfacial Thermal Conductance at Gold-Alkane Junctions From 'First Principles'," J. Heat Tran., vol.

140, no. 9, p. 092405, 2018.

5. R. Cheaito, C. A. Polanco, S. Addamane, **J. Zhang**, A. W. Ghosh, G. Balakrishnan, and P. E. Hopkins, “Interplay between total thickness and period thickness in the phonon thermal conductivity of superlattices from the nanoscale to the microscale: Coherent versus incoherent phonon transport,” Phys. Rev. B, vol. 97, p. 085306, Feb 2018.

6. A. D. Oyedele, S. Yang, L. Liang, A. A. Puretzky, K. Wang, **J. Zhang**, P. Yu, P. R. Pudasaini, A. W. Ghosh, Z. Liu, C. M. Rouleau, B. G. Sumpter, M. F. Chisholm, W. Zhou, P. D. Rack, D. B. Geohegan, and K. Xiao, “PdSe2: Pentagonal Two-Dimensional Layers with High Air Stability for Electronics,” Journal of the American Chemical Society, vol. 139, p. 14090, Sep 2017.

7. N. Q. Le, C. A. Polanco, R. Rastgarkafshgarkolaei, **J. Zhang**, A. W. Ghosh, and P. M. Norris, “Effects of bulk and interfacial anharmonicity on thermal conductance at solid/solid interfaces,” Phys. Rev. B, vol. 95, p. 245417, Jun 2017.

8. C. A. Polanco, R. Rastgarkafshgarkolaei, **J. Zhang**, N. Q. Le, P. M. Norris, and A. W. Ghosh, “Design rules for interfacial thermal conductance: Building better bridges,” Phys. Rev. B, vol. 95, p. 195303, May 2017.

9. C. A. Polanco, R. Rastgarkafshgarkolaei, **J. Zhang**, N. Q. Le, P. M. Norris, P. E. Hopkins, and A. W. Ghosh, “Role of crystal structure and junction morphology on interface thermal conductance,” Phys. Rev. B, vol. 92, p. 144302, Oct 2015.

Bibliography

[1] D. G. Cahill, W. K. Ford, K. E. Goodson, G. D. Mahan, A. Majumdar, H. J. Maris, R. Merlin, and S. R. Phillpot, “Nanoscale thermal transport,” *Journal of Applied Physics*, vol. 93, no. 793, 2003.

[2] D. G. Cahill, P. V. Braun, G. Chen, D. R. Clarke, S. Fan, K. E. Goodson, P. Keblinski, W. P. King, G. D. Mahan, A. Majumdar, H. J. Maris, S. R. Phillpot, E. Pop, and L. Shi, “Nanoscale thermal transport. II. 2003-2012,” *Applied Physics Reviews*, vol. 1, no. 1, p. 011305, 2014.

[3] E. Pop, “Energy Dissipation and Transport in Nanoscale Devices,” *Nano Res.*, vol. 3, p. 147, 2010.

[4] A. J. Minnich, M. S. Dresselhaus, Z. F. Ren, and G. Chen, “Bulk nanostructured thermoelectric materials: current research and future prospects,” *Energy Environ. Sci.*, vol. 2, pp. 466–479, 2009.

[5] A. M. Dehkordi, M. Zebarjadi, J. He, and T. M. Tritt, “Thermoelectric power factor: Enhancement mechanisms and strategies for higher performance thermoelectric materials,” *Materials Science and Engineering: R: Reports*, vol. 97, pp. 1 – 22, 2015.

[6] K. Biswas, J. He, I. D. Blum, C.-I. Wu, T. P. Hogan, D. N. Seidman, V. P. Dravid, and M. G. Kanatzidis, “High-performance bulk thermoelectrics with all-scale hierarchical architectures,” *Nature*, vol. 489, p. 414, 9 2012.

[7] A. I. Hochbaum, R. Chen, R. D. Delgado, W. Liang, E. C. Garnett, M. Najarian, A. Majumdar, and P. Yang, “Enhanced thermoelectric performance of rough silicon nanowires,” *Nature*, vol. 451, no. 7175, p. 163, 2008.

[8] R. E. Rottmayer, S. Batra, D. Buechel, W. A. Challener, J. Hohlfeld, Y. Kubota, L. Li, B. Lu, C. Mihalcea, K. Mountfield, K. Pelhos, C. Peng, T. Rausch, M. A. Seigler, D. Weller, and X. . Yang, “Heat-assisted magnetic recording,” *IEEE Transactions on Magnetics*, vol. 42, pp. 2417–2421, Oct 2006.

[9] L. Pan and D. B. Bogy, “Data storage: Heat-assisted magnetic recording,” *Nature Photonics*, vol. 3, no. 4, p. 189, 2009.

[10] Y. Shen, J. Gaskins, X. Xie, B. M. Foley, R. Cheaito, P. E. Hopkins, and J. C. Campbell, “Thermal analysis of high-power flip-chip-bonded photodiodes,” *Journal of Lightwave Technology*, vol. 35, pp. 4242–4246, Oct 2017.

[11] Q. Zhou, A. S. Cross, Y. Fu, A. Beling, B. M. Foley, P. E. Hopkins, and J. C. Campbell, "Balanced inp/ingaas photodiodes with 1.5-w output power," *IEEE Photonics Journal*, vol. 5, pp. 6800307–6800307, June 2013.

[12] B. S. Williams, "Terahertz quantum-cascade lasers," *Nature photonics*, vol. 1, no. 9, p. 517, 2007.

[13] H. Iwai, "Roadmap for 22nm and beyond (invited paper)," *Microelectronic Engineering*, vol. 86, no. 7, pp. 1520 – 1528, 2009. INFOS 2009.

[14] F. VanGessel, J. Peng, and P. W. Chung, "A review of computational phononics: the bulk, interfaces, and surfaces," *Journal of Materials Science*, vol. 53, pp. 5641–5683, Apr 2018.

[15] S. Chhabra and Y. Solihin, *Green Secure Processors: Towards Power-Efficient Secure Processor Design*. Berlin, Heidelberg: Springer Berlin Heidelberg, 2010.

[16] I. Dincer and C. Zamfirescu, *Sustainable energy systems and applications*. Springer Science & Business Media, 2011.

[17] M. Lundstrom, "Moore's law forever?," *Science*, vol. 299, no. 5604, pp. 210–211, 2003.

[18] R. R. Schaller, "Moore's law: past, present and future," *IEEE Spectrum*, vol. 34, pp. 52–59, June 1997.

[19] A. L. Moore and L. Shi, "Emerging challenges and materials for thermal management of electronics," *Materials Today*, vol. 17, no. 4, pp. 163 – 174, 2014.

[20] H. Casimir, "Note on the conduction of heat in crystals," *Physica*, vol. 5, no. 6, pp. 495–500, 1938.

[21] R. Cheaito, J. C. Duda, T. E. Beechem, K. Hattar, J. F. Ihlefeld, D. L. Medlin, M. A. Rodriguez, M. J. Campion, E. S. Piekos, and P. E. Hopkins, "Experimental investigation of size effects on the thermal conductivity of silicon-germanium alloy thin films," *Phys. Rev. Lett.*, vol. 109, p. 195901, Nov 2012.

[22] A. Ghosh, *Nanoelectronics: a molecular view*, vol. 13. World Scientific Publishing Company, 2016.

[23] N. Zen, T. A. Puurtinen, T. J. Isotalo, S. Chaudhuri, and I. J. Maasilta, "Engineering thermal conductance using a two-dimensional phononic crystal," *Nature communications*, vol. 5, p. 3435, 2014.

[24] M. V. Simkin and G. D. Mahan, "Minimum thermal conductivity of superlattices," *Phys. Rev. Lett.*, vol. 84, pp. 927–930, Jan 2000.

[25] A. A. Balandin, "Nanophononics: Phonon engineering in nanostructures and nanodevices," *Journal of Nanoscience and Nanotechnology*, vol. 5, no. 7, pp. 1015–1022, 2005.

[26] M. Maldovan, “Phonon wave interference and thermal bandgap materials,” *Nature materials*, vol. 14, p. 667, June 2015.

[27] S. Sinha and K. E. Goodson, “Multiscale thermal modeling in nanoelectronics,” *International Journal for Multiscale Computational Engineering*, vol. 3, no. 1, 2005.

[28] T. Luo and G. Chen, “Nanoscale heat transfer ÃćÂĂÂŞ from computation to experiment,” *Phys. Chem. Chem. Phys.*, vol. 15, pp. 3389–3412, 2013.

[29] G. Chen, “Multiscale simulation of phonon and electron thermal transport,” *Annual Review of Heat Transfer*, vol. 17, 2014.

[30] B. Radisavljevic, A. Radenovic, J. Brivio, V. Giacometti, and A. Kis, “Single-layer MoS_2 transistors,” *Nature Nanotechnology*, vol. 6, pp. 147–150, mar 2011.

[31] O. Lopez-Sanchez, D. Lembke, M. Kayci, A. Radenovic, and A. Kis, “Ultrasensitive photodetectors based on monolayer MoS_2,” *Nature Nanotechnology*, vol. 8, pp. 497–501, jul 2013.

[32] Z. Yin, H. Li, H. Li, L. Jiang, Y. Shi, Y. Sun, G. Lu, Q. Zhang, X. Chen, and H. Zhang, “Single-Layer MoS_2 Phototransistors,” *ACS Nano*, vol. 6, pp. 74–80, jan 2012.

[33] Z. Jin, Q. Liao, H. Fang, Z. Liu, W. Liu, Z. Ding, T. Luo, and N. Yang, “A Revisit to High Thermoelectric Performance of Single-layer MoS 2,” *Scientific Reports*, vol. 5, p. 18342, nov 2016.

[34] H. Babaei, J. M. Khodadadi, and S. Sinha, “Large theoretical thermoelectric power factor of suspended single-layer MoS_2,” *Applied Physics Letters*, vol. 105, p. 193901, nov 2014.

[35] J. Wu, H. Schmidt, K. K. Amara, X. Xu, G. Eda, and B. Özyilmaz, “Large Thermoelectricity via Variable Range Hopping in Chemical Vapor Deposition Grown Single-Layer MoS_2,” *Nano Letters*, vol. 14, pp. 2730–2734, may 2014.

[36] K. F. Mak, C. Lee, J. Hone, J. Shan, and T. F. Heinz, “Atomically Thin MoS_2 : A New Direct-Gap Semiconductor,” *Physical Review Letters*, vol. 105, p. 136805, sep 2010.

[37] H. J. Conley, B. Wang, J. I. Ziegler, R. F. Haglund, S. T. Pantelides, and K. I. Bolotin, “Bandgap Engineering of Strained Monolayer and Bilayer MoS_2,” *Nano Letters*, vol. 13, pp. 3626–3630, aug 2013.

[38] E. Scalise, M. Houssa, G. Pourtois, V. Afanas’ev, and A. Stesmans, “Strain-induced semiconductor to metal transition in the two-dimensional honeycomb structure of MoS_2,” *Nano Research*, vol. 5, pp. 43–48, jan 2012.

[39] J. Liu, G.-M. Choi, and D. G. Cahill, “Measurement of the anisotropic thermal conductivity of molybdenum disulfide by the time-resolved magneto-optic Kerr effect,” *Journal of Applied Physics*, vol. 116, p. 233107, dec 2014.

[40] R. Yan, J. R. Simpson, S. Bertolazzi, J. Brivio, M. Watson, X. Wu, A. Kis, T. Luo, A. R. Hight Walker, and H. G. Xing, "Thermal Conductivity of Monolayer Molybdenum Disulfide Obtained from Temperature-Dependent Raman Spectroscopy," *ACS Nano*, vol. 8, pp. 986–993, jan 2014.

[41] S. Sahoo, A. P. S. Gaur, M. Ahmadi, M. J.-F. Guinel, and R. S. Katiyar, "Temperature-Dependent Raman Studies and Thermal Conductivity of Few-Layer MoS_2," *The Journal of Physical Chemistry C*, vol. 117, pp. 9042–9047, may 2013.

[42] I. Jo, M. T. Pettes, E. Ou, W. Wu, and L. Shi, "Basal-plane thermal conductivity of few-layer molybdenum disulfide," *Applied Physics Letters*, vol. 104, p. 201902, may 2014.

[43] X. Zhang, D. Sun, Y. Li, G.-H. Lee, X. Cui, D. Chenet, Y. You, T. F. Heinz, and J. C. Hone, "Measurement of Lateral and Interfacial Thermal Conductivity of Single- and Bilayer MoS_2 and $MoSe_2$ Using Refined Optothermal Raman Technique," *ACS Applied Materials & Interfaces*, vol. 7, pp. 25923–25929, nov 2015.

[44] X. Li, J. Zhang, A. A. Puretzky, A. Yoshimura, X. Sang, Q. Cui, Y. Li, L. Liang, A. W. Ghosh, H. Zhao, R. R. Unocic, V. Meunier, C. M. Rouleau, B. G. Sumpter, D. B. Geohegan, and K. Xiao, "Isotope-Engineering the Thermal Conductivity of Two-Dimensional MoS_2," *ACS nano*, vol. 13, no. 2, pp. 2481–2489, 2019.

[45] W. Li, J. Carrete, and N. Mingo, "Thermal conductivity and phonon linewidths of monolayer MoS_2 from first principles," *Applied Physics Letters*, vol. 103, p. 253103, dec 2013.

[46] X. Gu and R. Yang, "Phonon transport in single-layer transition metal dichalcogenides: A first-principles study," *Applied Physics Letters*, vol. 105, no. 13, p. 131903, 2014.

[47] Y. Cai, J. Lan, G. Zhang, and Y.-W. Zhang, "Lattice vibrational modes and phonon thermal conductivity of monolayer MoS_2," *Phys. Rev. B*, vol. 89, p. 035438, Jan 2014.

[48] Y. Hong, J. Zhang, and X. C. Zeng, "Thermal Conductivity of Monolayer $MoSe_2$ and MoS_2," *The Journal of Physical Chemistry C*, vol. 120, no. 45, pp. 26067–26075, 2016.

[49] A. N. Gandi and U. Schwingenschlögl, "Thermal conductivity of bulk and monolayer MoS_2," *EPL (Europhysics Letters)*, vol. 113, p. 36002, feb 2016.

[50] B. Peng, H. Zhang, H. Shao, Y. Xu, X. Zhang, and H. Zhu, "Thermal conductivity of monolayer MoS_2, $MoSe_2$, and WS_2: interplay of mass effect, interatomic bonding and anharmonicity," *RSC Advances*, vol. 6, no. 7, pp. 5767–5773, 2016.

[51] Z. Yan, M. Yoon, and S. Kumar, "A first-principles study of phonon transport properties of monolayer $MoSe_2$," in *2017 16th IEEE Intersociety Conference on Thermal and Thermomechanical Phenomena in Electronic Systems (ITherm)*, pp. 143–148, IEEE, May 2017.

[52] J. Zhang, X. Li, K. Xiao, B. G. Sumpter, A. W. Ghosh, and L. Liang, “The role of mid-gap phonon modes in thermal transport of transition metal dichalcogenides,” *Journal of Physics: Condensed Matter*, 2019.

[53] P. Giannozzi, S. Baroni, N. Bonini, M. Calandra, R. Car, C. Cavazzoni, D. Ceresoli, G. L. Chiarotti, M. Cococcioni, I. Dabo, A. Dal Corso, S. de Gironcoli, S. Fabris, G. Fratesi, R. Gebauer, U. Gerstmann, C. Gougoussis, A. Kokalj, M. Lazzeri, L. Martin-Samos, N. Marzari, F. Mauri, R. Mazzarello, S. Paolini, A. Pasquarello, L. Paulatto, C. Sbraccia, S. Scandolo, G. Sclauzero, A. P. Seitsonen, A. Smogunov, P. Umari, and R. M. Wentzcovitch, “QUANTUM ESPRESSO: a modular and open-source software project for quantum simulations of materials,” *Journal of Physics: Condensed Matter*, vol. 21, p. 395502, sep 2009.

[54] J. P. Perdew and A. Zunger, “Self-interaction correction to density-functional approximations for many-electron systems,” *Physical Review B*, vol. 23, pp. 5048–5079, may 1981.

[55] S. Baroni, S. de Gironcoli, A. Dal Corso, and P. Giannozzi, “Phonons and related crystal properties from density-functional perturbation theory,” *Reviews of Modern Physics*, vol. 73, pp. 515–562, jul 2001.

[56] S. Datta, *Quantum Transport: Atom to Transistor.* Cambridge, England: Cambridge University Press, 2005.

[57] C. Jeong, S. Datta, and M. Lundstrom, “Thermal conductivity of bulk and thin-film silicon: A Landauer approach,” *Journal of Applied Physics*, vol. 111, p. 093708, may 2012.

[58] C. A. Polanco, R. Rastgarkafshgarkolaei, J. Zhang, N. Q. Le, P. M. Norris, P. E. Hopkins, and A. W. Ghosh, “Role of crystal structure and junction morphology on interface thermal conductance,” *Phys. Rev. B*, vol. 92, p. 144302, Oct 2015.

[59] R. Rastgarkafshgarkolaei, J. Zhang, C. A. Polanco, N. Q. Le, A. W. Ghosh, and P. M. Norris, “Maximization of thermal conductance at interfaces via exponentially mass-graded interlayers,” *Nanoscale*, vol. 11, pp. 6254–6262, 2019.

[60] J.-S. Wang, J. Wang, and J. T. Lü, “Quantum thermal transport in nanostructures,” *The European Physical Journal B*, vol. 62, pp. 381–404, apr 2008.

[61] N. Mingo and L. Yang, “Phonon transport in nanowires coated with an amorphous material: An atomistic Green’s function approach,” *Physical Review B*, vol. 68, p. 245406, dec 2003.

[62] W. Li, J. Carrete, N. A. Katcho, and N. Mingo, “ShengBTE: A solver of the Boltzmann transport equation for phonons,” *Computer Physics Communications*, vol. 185, pp. 1747–1758, jun 2014.

[63] J. M. Ziman, *Electrons and phonons: the theory of transport phenomena in solids.* Oxford university press, 2001.

[64] N. H. Protik, J. Carrete, N. A. Katcho, N. Mingo, and D. Broido, “Ab initio study of the effect of vacancies on the thermal conductivity of boron arsenide,” *Phys. Rev. B*, vol. 94, p. 045207, Jul 2016.

[65] D. A. Broido, L. Lindsay, and T. L. Reinecke, “Ab initio study of the unusual thermal transport properties of boron arsenide and related materials,” *Phys. Rev. B*, vol. 88, p. 214303, Dec 2013.

[66] L. Lindsay, D. A. Broido, and T. L. Reinecke, “First-principles determination of ultrahigh thermal conductivity of boron arsenide: A competitor for diamond?,” *Phys. Rev. Lett.*, vol. 111, p. 025901, Jul 2013.

[67] A. A. Balandin, “Phonon engineering in graphene and van der waals materials,” *MRS Bulletin*, vol. 39, no. 9, pp. 817–823, 2014.

[68] D. L. Nika and A. A. Balandin, “Two-dimensional phonon transport in graphene,” *Journal of Physics: Condensed Matter*, vol. 24, no. 23, p. 233203, 2012.

[69] W. Cai, A. L. Moore, Y. Zhu, X. Li, S. Chen, L. Shi, and R. S. Ruoff, “Thermal transport in suspended and supported monolayer graphene grown by chemical vapor deposition,” *Nano letters*, vol. 10, no. 5, pp. 1645–1651, 2010.

[70] B. Chakraborty, H. S. S. R. Matte, A. K. Sood, and C. N. R. Rao, “Layer-dependent resonant Raman scattering of a few layer MoS_2,” *Journal of Raman Spectroscopy*, vol. 44, no. 1, pp. 92–96, 2013.

[71] S. Tamura, “Isotope scattering of dispersive phonons in ge,” *Phys. Rev. B*, vol. 27, pp. 858–866, 1983.

[72] C. A. Ratsifaritana and P. G. Klemens, “Scattering of phonons by vacancies,” *International journal of thermophysics*, vol. 8, pp. 737–750, 1987.

[73] G. Xie, Y. Shen, X. Wei, L. Yang, H. Xiao, J. Zhong, and G. Zhang, “A bond-order theory on the phonon scattering by vacancies in two-dimensional materials,” *Scientific reports*, vol. 4, p. 5085, 2014.

[74] P. G. Klemens, “Thermal conductivity and lattice vibrational modes,” in *Solid state physics* (F. Seitz and D. Turnbull, eds.), vol. 7, pp. 1–98, Academic Press, 1958.

[75] P. G. Klemens, “The scattering of low-frequency lattice waves by static imperfections,” *Proceedings of the Physical Society. Section A*, vol. 68, no. 12, pp. 1113–1128, 1955.

[76] A. A. Balandin, S. Ghosh, W. Bao, I. Calizo, D. Teweldebrhan, F. Miao, and C. N. Lau, “Superior thermal conductivity of single-layer graphene,” *Nano Lett.*, vol. 8, no. 3, pp. 902–907, 2008.

[77] J. Garg, N. Bonini, B. Kozinsky, and N. Marzari, “Role of disorder and anharmonicity in the thermal conductivity of silicon-germanium alloys: A first-principles study,” *Phys. Rev. Lett.*, vol. 106, p. 045901, Jan 2011.

[78] C. A. Polanco and L. Lindsay, “Ab initio phonon point defect scattering and thermal transport in graphene,” *Phys. Rev. B*, vol. 97, p. 014303, Jan 2018.

[79] G. Riedel, J. Pomeroy, K. Hilton, J. Maclean, D. Wallis, M. Uren, T. Martin, U. Forsberg, A. Lundskog, A. Kakanakova-Georgieva, G. Pozina, E. Janzen, R. Lossy, R. Pazirandeh, F. Brunner, J. Wurfl, and M. Kuball, “Reducing Thermal Resistance of AlGaN/GaN Electronic Devices Using Novel Nucleation Layers,” *IEEE Electron Dev. Lett.*, vol. 30, no. 2, p. 103, 2009.

[80] K. Park and C. Bayram, “Thermal resistance optimization of GaN/substrate stacks considering thermal boundary resistance and temperature-dependent thermal conductivity,” *Applied Physics Letters*, vol. 109, p. 151904, oct 2016.

[81] A. Sarua, H. Ji, K. P. Hilton, D. J. Wallis, M. J. Uren, T. Martin, and M. Kuball, “Thermal Boundary Resistance Between GaN and Substrate in AlGaN/GaN Electronic Devices,” *IEEE Transactions on Electron Devices*, vol. 54, no. 12, pp. 3152–3158, 2007.

[82] P. E. Hopkins, “Thermal Transport across Solid Interfaces with Nanoscale Imperfections: Effects of Roughness, Disorder, Dislocations, and Bonding on Thermal Boundary Conductance,” *ISRN Mechanical Engineering*, vol. 2013, pp. 1–19, jan 2013.

[83] C. S. Gorham, K. Hattar, R. Cheaito, J. C. Duda, J. T. Gaskins, T. E. Beechem, J. F. Ihlefeld, L. B. Biedermann, E. S. Piekos, D. L. Medlin, and P. E. Hopkins, “Ion irradiation of the native oxide/silicon surface increases the thermal boundary conductance across aluminum/silicon interfaces,” *Phys. Rev. B*, vol. 90, p. 024301, Jul 2014.

[84] Z. Liang and H.-L. Tsai, “Effect of thin film confined between two dissimilar solids on interfacial thermal resistance,” *Journal of Physics: Condensed Matter*, vol. 23, no. 49, p. 495303, 2011.

[85] Z. Liang and H.-L. Tsai, “Reduction of solid–solid thermal boundary resistance by inserting an interlayer,” *International Journal of Heat and Mass Transfer*, vol. 55, no. 11-12, pp. 2999–3007, 2012.

[86] T. S. English, J. C. Duda, J. L. Smoyer, D. A. Jordan, P. M. Norris, and L. V. Zhigilei, “Enhancing and tuning phonon transport at vibrationally mismatched solid-solid interfaces,” *Phys. Rev. B*, vol. 85, p. 035438, Jan 2012.

[87] Z. Tian, K. Esfarjani, and G. Chen, “Enhancing phonon transmission across a Si/Ge interface by atomic roughness: First-principles study with the Green’s function method,” *Phys. Rev. B*, vol. 86, p. 235304, Dec 2012.

[88] C. A. Polanco, R. Rastgarkafshgarkolaei, J. Zhang, N. Q. Le, P. M. Norris, and A. W. Ghosh, “Design rules for interfacial thermal conductance: Building better bridges,” *Phys. Rev. B*, vol. 95, p. 195303, May 2017.

[89] E. Lee, T. Yoo, and T. Luo, “The role of intermediate layers in thermal transport across GaN/SiC interfaces,” in *ITherm 2017 Proceedings*, pp. 368–372, IEEE, May 2017.

[90] J. Zhang, C. A. Polanco, and A. W. Ghosh, "Optimizing the Interfacial Thermal Conductance at Gold-Alkane Junctions From 'First Principles'," *J. Heat Tran.*, vol. 140, no. 9, p. 092405, 2018.

[91] P. Jiang, B. Huang, and Y. K. Koh, "Accurate measurements of cross-plane thermal conductivity of thin films by dual-frequency time-domain thermoreflectance (tdtr)," *Review of Scientific Instruments*, vol. 87, no. 7, p. 075101, 2016.

[92] D. G. Cahill, "Analysis of heat flow in layered structures for time-domain thermoreflectance," *Review of Scientific Instruments*, vol. 75, no. 12, pp. 5119–5122, 2004.

[93] I. Calizo, A. A. Balandin, W. Bao, F. Miao, and C. N. Lau, "Temperature dependence of the raman spectra of graphene and graphene multilayers," *Nano Letters*, vol. 7, no. 9, pp. 2645–2649, 2007.

[94] M. Luisier, "Atomistic modeling of anharmonic phonon-phonon scattering in nanowires," *Physical Review B*, vol. 86, no. 24, p. 245407, 2012.

[95] N. Mingo, "Anharmonic phonon flow through molecular-sized junctions," *Phys. Rev. B*, vol. 74, p. 125402, Sep 2006.

[96] S. Plimpton, "Fast parallel algorithms for short-range molecular dynamics," *Journal of Computational Physics*, vol. 117, no. 1, pp. 1 – 19, 1995.

[97] Z. Tian, K. Esfarjani, and G. Chen, "Green's function studies of phonon transport across Si/Ge superlattices," *Phys. Rev. B*, vol. 89, p. 235307, Jun 2014.

[98] I. Altfeder, A. A. Voevodin, and A. K. Roy, "Vacuum phonon tunneling," *Phys. Rev. Lett.*, vol. 105, p. 166101, Oct 2010.

[99] Z. T. Tian, B. E. White, and Y. Sun, "Phonon wave-packet interference and phonon tunneling based energy transport across nanostructured thin films," *Applied Physics Letters*, vol. 96, no. 26, p. 263113, 2010.

[100] K. Gordiz and A. Henry, "Phonon transport at crystalline Si/Ge interfaces: the role of interfacial modes of vibration," *Scientific reports*, vol. 6, p. 23139, 2016.

[101] K. Gordiz and A. Henry, "Interface conductance modal analysis of lattice matched InGaAs/InP," *Applied Physics Letters*, vol. 108, no. 18, p. 181606, 2016.

[102] K. Gordiz and A. Henry, "Phonon transport at interfaces: Determining the correct modes of vibration," *Journal of Applied Physics*, vol. 119, no. 1, p. 015101, 2016.

[103] N. Q. Le, C. A. Polanco, R. Rastgarkafshgarkolaei, J. Zhang, A. W. Ghosh, and P. M. Norris, "Effects of bulk and interfacial anharmonicity on thermal conductance at solid/solid interfaces," *Phys. Rev. B*, vol. 95, p. 245417, Jun 2017.

[104] X. Wu and T. Luo, "The importance of anharmonicity in thermal transport across solid-solid interfaces," *Journal of Applied Physics*, vol. 115, no. 1, p. 014901, 2014.

[105] Z. Tian, J. Garg, K. Esfarjani, T. Shiga, J. Shiomi, and G. Chen, "Phonon conduction in PbSe, PbTe, and PbTe1 $-$ xSe$_x$ from first-principles calculations," *Phys. Rev. B*, vol. 85, p. 184303, May 2012.

[106] A. McGaughey, "Predicting phonon properties from equilibrium molecular dynamics simulations," *Annual Review of Heat Transfer*, vol. 17, 2014.

[107] P. B. Clapham and M. C. Hutley, "Reduction of Lens Reflexion by the "Moth Eye" Principle," *Nature*, vol. 244, p. 281, 1973.

[108] C. Bernhard, "Structural and functional adaptation in a visual system," *Endeavour*, vol. 26, no. 98, p. 79, 1967.

[109] C. A. Polanco, C. B. Saltonstall, P. M. Norris, P. E. Hopkins, and A. W. Ghosh, "Impedance Matching of Atomic Thermal Interfaces Using Primitive Block Decomposition," *Nanoscale Microscale Thermophys. Eng.*, vol. 17, no. 3, p. 263, 2013.

[110] S. Lepri, R. Livi, and A. Politi, "Thermal conduction in classical low-dimensional lattices," *Physics Reports*, vol. 377, no. 1, pp. 1 – 80, 2003.

[111] A. Dhar, "Heat transport in low-dimensional systems," *Advances in Physics*, vol. 57, no. 5, pp. 457–537, 2008.

[112] R. Clausius, *The Nature of the Motion which we call Heat*, pp. 111–134. Philosophical Magazine, 1857.

[113] S. Datta, *Electronic transport in mesoscopic systems.* Cambridge, England: Cambridge university press, 1997.

[114] R. Peierls, "Zur kinetischen theorie der wärmeleitung in kristallen," *Annalen der Physik*, vol. 395, no. 8, pp. 1055–1101, 1929.

[115] K. Sääskilahti, J. Oksanen, S. Volz, and J. Tulkki, "Nonequilibrium phonon mean free paths in anharmonic chains," *Phys. Rev. B*, vol. 92, p. 245411, Dec 2015.

[116] K. Sääskilahti, J. Oksanen, S. Volz, and J. Tulkki, "Frequency-dependent phonon mean free path in carbon nanotubes from nonequilibrium molecular dynamics," *Phys. Rev. B*, vol. 91, p. 115426, Mar 2015.

[117] Y. S. Ju and K. E. Goodson, "Phonon scattering in silicon films with thickness of order 100 nm," *Applied Physics Letters*, vol. 74, no. 20, pp. 3005–3007, 1999.

[118] R. S. Prasher, X. J. Hu, Y. Chalopin, N. Mingo, K. Lofgreen, S. Volz, F. Cleri, and P. Keblinski, "Turning carbon nanotubes from exceptional heat conductors into insulators," *Phys. Rev. Lett.*, vol. 102, p. 105901, Mar 2009.

[119] Z. Yan, G. Liu, J. M. Khan, and A. A. Balandin, "Graphene quilts for thermal management of high-power gan transistors," *Nature communications*, vol. 3, p. 827, 5 2012.

[120] M. S. Kushwaha, P. Halevi, L. Dobrzynski, and B. Djafari-Rouhani, “Acoustic band structure of periodic elastic composites,” *Phys. Rev. Lett.*, vol. 71, pp. 2022–2025, Sep 1993.

[121] R. Venkatasubramanian, “Lattice thermal conductivity reduction and phonon localizationlike behavior in superlattice structures,” *Phys. Rev. B*, vol. 61, pp. 3091–3097, Jan 2000.

[122] S. Chakraborty, C. A. Kleint, A. Heinrich, C. M. Schneider, J. Schumann, M. Falke, and S. Teichert, “Thermal conductivity in strain symmetrized Si/Ge superlattices on Si(111),” *Applied Physics Letters*, vol. 83, no. 20, pp. 4184–4186, 2003.

[123] V. Rawat, Y. K. Koh, D. G. Cahill, and T. D. Sands, “Thermal conductivity of (Zr,W)N/ScN metal/semiconductor multilayers and superlattices,” *Journal of Applied Physics*, vol. 105, no. 2, p. 024909, 2009.

[124] J. Ravichandran, A. K. Yadav, R. Cheaito, P. B. Rossen, A. Soukiassian, S. Suresha, J. C. Duda, B. M. Foley, C.-H. Lee, Y. Zhu, *et al.*, “Crossover from incoherent to coherent phonon scattering in epitaxial oxide superlattices,” *Nature materials*, vol. 13, p. 168, December 2014.

[125] M. N. Luckyanova, J. Garg, K. Esfarjani, A. Jandl, M. T. Bulsara, A. J. Schmidt, A. J. Minnich, S. Chen, M. S. Dresselhaus, Z. Ren, E. A. Fitzgerald, and G. Chen, “Coherent phonon heat conduction in superlattices,” *Science*, vol. 338, no. 6109, pp. 936–939, 2012.

[126] C. Akcay, P. Parrein, and J. P. Rolland, “Estimation of longitudinal resolution in optical coherence imaging,” *Appl. Opt.*, vol. 41, pp. 5256–5262, Sep 2002.

[127] L. Mandel and E. Wolf, *Optical coherence and quantum optics.* Cambridge, England: Cambridge university press, 1995.

[128] R. G. Winter, A. M. Steinberg, and D. Attwood, “Coherence,” 2008.

[129] B. Latour, S. Volz, and Y. Chalopin, “Microscopic description of thermal-phonon coherence: From coherent transport to diffuse interface scattering in superlattices,” *Phys. Rev. B*, vol. 90, p. 014307, Jul 2014.

[130] B. Latour and Y. Chalopin, “Distinguishing between spatial coherence and temporal coherence of phonons,” *Phys. Rev. B*, vol. 95, p. 214310, Jun 2017.

[131] C. H. Lewenkopf and E. R. Mucciolo, “The recursive green’s function method for graphene,” *ournal of Computational Electronics*, vol. 12, pp. 203–231, Jun 2013.

[132] R. Golizadeh-Mojarad and S. Datta, “Nonequilibrium green’s function based models for dephasing in quantum transport,” *Phys. Rev. B*, vol. 75, p. 081301, Feb 2007.

[133] R. Lake, G. Klimeck, R. C. Bowen, and D. Jovanovic, “Single and multiband modeling of quantum electron transport through layered semiconductor devices,” *Journal of Applied Physics*, vol. 81, no. 12, pp. 7845–7869, 1997.

[134] A. M. Kriman, N. C. Kluksdahl, and D. K. Ferry, “Scattering states and distribution functions for microstructures,” *Phys. Rev. B*, vol. 36, pp. 5953–5959, Oct 1987.

[135] E. Lisi, A. Marrone, and D. Montanino, “Probing possible decoherence effects in atmospheric neutrino oscillations,” *Phys. Rev. Lett.*, vol. 85, pp. 1166–1169, Aug 2000.

[136] P. Zanardi, “Dissipation and decoherence in a quantum register,” *Phys. Rev. A*, vol. 57, pp. 3276–3284, May 1998.

[137] R. Alicki, “Pure decoherence in quantum systems,” *Open Systems & Information Dynamics*, vol. 11, no. 01, pp. 53–61, 2004.

[138] S. Takahashi, I. Tupitsyn, J. Van Tol, C. Beedle, D. Hendrickson, and P. Stamp, “Decoherence in crystals of quantum molecular magnets,” *Nature*, vol. 476, no. 7358, p. 76, 2011.

[139] B. C. Daly, H. J. Maris, K. Imamura, and S. Tamura, “Molecular dynamics calculation of the thermal conductivity of superlattices,” *Phys. Rev. B*, vol. 66, p. 024301, Jun 2002.

[140] Y. Chen, D. Li, J. R. Lukes, Z. Ni, and M. Chen, “Minimum superlattice thermal conductivity from molecular dynamics,” *Phys. Rev. B*, vol. 72, p. 174302, Nov 2005.

[141] E. S. Landry and A. J. H. McGaughey, “Effect of interfacial species mixing on phonon transport in semiconductor superlattices,” *Phys. Rev. B*, vol. 79, p. 075316, Feb 2009.

[142] Y. Wang, C. Gu, and X. Ruan, “Optimization of the random multilayer structure to break the random-alloy limit of thermal conductivity,” *Applied Physics Letters*, vol. 106, no. 7, p. 073104, 2015.

[143] B. Qiu, G. Chen, and Z. Tian, “Effects of aperiodicity and roughness on coherent heat conduction in superlattices,” *Nanoscale and Microscale Thermophysical Engineering*, vol. 19, no. 4, pp. 272–278, 2015.

[144] T. Zhu and E. Ertekin, “Phonon transport on two-dimensional graphene/boron nitride superlattices,” *Phys. Rev. B*, vol. 90, p. 195209, Nov 2014.

[145] S. C. Huberman, J. M. Larkin, A. J. H. McGaughey, and C. H. Amon, “Disruption of superlattice phonons by interfacial mixing,” *Phys. Rev. B*, vol. 88, p. 155311, Oct 2013.

[146] R. Cheaito, C. A. Polanco, S. Addamane, J. Zhang, A. W. Ghosh, G. Balakrishnan, and P. E. Hopkins, “Interplay between total thickness and period thickness in the phonon thermal conductivity of superlattices from the nanoscale to the microscale: Coherent versus incoherent phonon transport,” *Phys. Rev. B*, vol. 97, p. 085306, Feb 2018.

[147] E. T. Swartz and R. O. Pohl, “Thermal Boundary Resistance,” *Reviews of Modern Physics*, vol. 61, no. 3, pp. 605–668, 1989.

[148] J. C. Duda, P. E. Hopkins, J. L. Smoyer, M. L. Bauer, T. S. English, C. B. Saltonstall, and P. M. Norris, "On the Assumption of Detailed Balance in Prediction of Diffusive Transmission Probability During Interfacial Transport," *Nanoscale and Microscale Thermophysical Engineering*, vol. 14, no. 1, pp. 21–33, 2010.